DIJET ANGULAR DISTRIBUTIONS AT $\sqrt{s} = 1800$ GeV USING THE DØ DETECTOR

by

Andrew James Milder

A Dissertation Submitted to the Faculty of the

DEPARTMENT OF PHYSICS

In Partial Fulfillment of the Requirements
For the Degree of

DOCTOR OF PHILOSOPHY

In the Graduate College

THE UNIVERSITY OF ARIZONA

1 9 9 3

Final Examining Committee Approval Form

STATEMENT BY AUTHOR

This dissertation has been submitted in partial fulfillment of requirements for an advanced degree at The University of Arizona and is deposited in the University Library to be made available to borrowers under rules of the Library.

Brief quotations from this dissertation are allowable without special permission, provided that accurate acknowledgement of source is made. Requests for permission for extended quotation from or reproduction of this manuscript in whole or in part may be granted by the head of the major department or the Dean of the Graduate College when in his or her judgement the proposed use of the material is in the interests of scholarship. In all other instances, however, permission must be obtained from the author.

SIGNED: _____

ACKNOWLEDGEMENTS

I appreciate the support and assistance of many people whose help made this endeavor, if not possible, then at least more enjoyable. I would like to thank everyone in the EEPP group at the University of Arizona: faculty, staff, and students (including the muon guys.) I would also like to thank the multitude of people who designed, built, and ran the DØ detector without whom this work would certainly not be possible. Also, the QCD group at DØ provided much assistance and feedback for this analysis, including Harry Weerts, Jerry Blazey, and especially Rich Astur. I also thank my advisor, John Rutherfoord, who provided support and advice, and allowed me to graduate in a reasonable time.

To my Parents.

TABLE OF CONTENTS

LIST OF FIGURES **9**

LIST OF TABLES **15**

ABSTRACT **16**

1 Introduction **17**

2 Theory **19**

2.1 Parton Model 19

2.2 Renormalization and the Running Coupling 20

2.3 Parton Distribution Functions 23

2.4 Jet Production 24

2.4.1 The hard interaction 25

2.4.2 Parton Showering 26

2.4.3 Hadronization 27

2.5 Jet Definition 29

2.6 Dijet Angular Distributions 30

2.6.1 Definition of Angular Variables 30

2.6.2 Calculation of $dN/d\chi$ in Leading Order 34

2.6.3 Next-to-Leading-Order Calculation of $d\sigma/d\chi$. 37

2.6.4 Effects of Compositeness 40

3 The DØ Detector **45**

3.1 Central Detector 45

3.2 Muon System 47

3.3 Calorimeter 48

3.3.1 Massless Gaps and Inner Cryostat Detectors 51
3.4 Trigger System 53

4 The Jet Reconstruction Algorithm 55
4.1 Cone Algorithm 56
4.1.1 Dijet Mass Measurement 58
4.2 Jet Reconstruction Tests 58
4.2.1 Jet Reconstruction Efficiency 59
4.2.2 Uncertainty in Reconstructed Jet Position 60
4.2.3 Tests of Jet Splitting and Merging 62

5 Data Selection and Corrections 67
5.1 Jet Triggering 67
5.1.1 Description of Triggers 67
5.1.2 Jet Trigger Efficiencies 70
5.2 Event Selection 71
5.2.1 Removal of Fake Jets 74
5.2.2 Trigger Threshold Cuts 76
5.3 Jet Energy Calibration 76
5.3.1 Jet Energy Scale in the Central Calorimeter 77
5.3.2 Jet Energy Scale at Large η 96
5.3.3 Jet Energy Resolution 103

6 Results 109
6.1 Acceptance Corrections 109
6.2 Systematic Uncertainties 116
6.3 Dijet Angular Distributions 117
6.4 Search for Quark Substructure 133
6.5 Conclusion 137

REFERENCES 139

LIST OF FIGURES

2.1 Deep inelastic electron-proton scattering. 21

2.2 Parton distribution functions weighted with x for the u valence quark and the gluon shown for different values of Q. The distribution MRS S0 is used. 22

2.3 Parton distribution functions weighted with x for the gluon and the u valence quark. Two different distributions are shown: set MRS S0 (solid line) and set Morfin-Tung B2 (dotted line) at $Q^2 = (50GeV)^2$. 24

2.4 Feynman diagrams for parton-parton scattering to order α_s^2. 25

2.5 Examples of α_s^3-order processes. 26

2.6 Schematic of the development of a parton shower. The time and distance increase from left to right while the invariant mass decreases. Hadrons form when the masses become of the order of Λ, the QCD scale parameter. 28

2.7 Dijet event in lab frame and center-of-mass frame. 31

2.8 $dN/d\cos\theta$ for pure Rutherford scattering (solid line) and for leading order QCD dijets (dashed line) 32

2.9 $dN/d\eta^*$ for pure Rutherford scattering (solid line) and for leading order QCD dijets (dashed line) 32

2.10 $dN/d\cos\eta$ for pure Rutherford scattering (solid line) and for leading order QCD dijets (dashed line) 33

2.11 Subprocess matrix elements χ-dependence $= \frac{|\mathcal{M}|^2}{g_s^4}\frac{1}{(\chi+1)^2}$. 35

2.12 Calculated $d\sigma/d\chi$ for $200 < M_{JJ} < 400$ and $|\eta_{boost}| < 2.0$ using $Q^2 = P_T^2/4$. The parton distribution functions MRS S0(solid), M-T B2(dashed) and CTEQ 1M(dotted) are used and the curves have been normalized over the range shown in χ. 38

2.13 Calculated $d\sigma/d\chi$ for $200 < M_{JJ} < 400$ and $|\eta_{boost}| < 2.0$ using CTEQ 1M. Different values of $Q^2 = P_T^2/4$(solid), P_T^2(dashed), $4P_T^2$(dotted) have been used and the curves have been normalized. 39

2.14 Calculated $d\sigma/d\chi$ for $200 < M_{JJ} < 400$ and all values of η_{boost} for $O(\alpha_s^2)$ and $O(\alpha_s^3)$ QCD calculations. The $O(\alpha_s^3)$ curve is flatter at high χ. The leading order prediction is shown for two choices of the momentum scale, $Q = P_T/2$ and $Q = .5M_{JJ}/2\cosh(0.7\eta^*)$. 41

2.15 Calculated $d\sigma/d\chi$ using $O(\alpha_s^2)$ QCD for $M_{JJ} > 500$ with and without the contact term. The compositeness scale used is $\Lambda_C = 1$ TeV. Although the contact term increases the cross section at low χ, here the two curves have been normalized over the range in χ shown in order to show differences in shape. 43

3.16 The DØ detector. 46

3.17 The DØ central tracking system. 48

3.18 Cross-section through calorimeter readout sampling cell. 49

3.19 Cutout view of the DØ calorimeter. 50

3.20 Cutout view of the calorimeter crack region. 52

4.21 Jet reconstruction efficiency. The algorithm is seen to be nearly 100% efficient for jets with $E_T > 20$ GeV. 60

4.22 Resolution in ϕ and η versus jet E_T using the Monte Carlo simulation. 61

4.23 Resolution in ϕ using actual dijet events compared to ϕ resolution from Monte Carlo. 62

4.24 Systematic shifts in reconstructed ϕ and η versus jet η using the Monte Carlo simulation. An η dependent bias is seen. 63

4.25 Number of jets found with EKS algorithm minus number of jets found with reconstruction algorithm when the splitting fraction equals 0.5. 65

5.26 Trigger efficiency for JET_MIN trigger. Efficiency versus jet E_T for jets with $|\eta| < 0.7$. 71
5.27 Trigger efficiency for JET_LOW trigger. Efficiency versus jet E_T for jets with $|\eta| < 0.7$. 72
5.28 Trigger efficiency for JET_MEDIUM trigger. Efficiency versus jet E_T for jets with $|\eta| < 0.7$. 72
5.29 Trigger efficiency for JET_HIGH trigger. Efficiency versus jet E_T for jets with $|\eta| < 0.7$. 73
5.30 Trigger efficiency for JET_MAX trigger. Efficiency versus jet E_T for jets with $|\eta| < 0.7$. 73
5.31 Efficiency of the cut .05 < EMfrac < .95 (a) versus $|\eta|$ for jets with $E_T > 25$ GeV, and (b) versus E_T for $0.9 < |\eta| < 1.4$. 75
5.32 Efficiency of the cut CHfrac < .4 (a) versus $|\eta|$ for jets with $E_T > 25$ GeV, and (b) versus E_T for $0.9 < |\eta| < 1.4$. 76
5.33 Test beam responses for electrons. 79
5.34 Test beam responses for pions. 79
5.35 Particle composition of 50 GeV jets. The percent contribution is shown integrated over lower energies. For example, particles with energies below 5 GeV make up about 70% of the total jet energy. . 81
5.36 Nominal jet energy scale and limits of errors. The thick line is the nominal response and the thin lines are the upper and lower limits. 83
5.37 Energy lost due to zero-suppression of data for jets with cone size $R = 0.7$. Plotted is ((unsuppressed energy) - (suppressed energy))/(unsuppressed energy) versus suppressed jet energy. 85
5.38 Direct photon event with single jet balancing P_T. If the calorimeter response to both the photon and jet is 100%, then the reconstructed missing E_T is zero. If the jet response is less than 100%, then there will be a reconstructed missing E_T vector pointing along the direction of the jet that is equal to the jet E_T lost due to low response. 87

5.39 Direct photon event with two balancing jets 88

5.40 Comparison of "actual" jet response (open circles) and MPF-derived response (solid circles) using HERWIG generated direct photon events and simulated calorimeter single particle responses and resolutions. 89

5.41 Comparison of "actual" jet response (open circles) and MPF-derived response (solid circles) using HERWIG generated electromagnetic jet events and simulated calorimeter single particle responses and resolutions. 91

5.42 Jet energy response using the MPF method. The best fit is shown by the solid line and the limits of the uncertainties by the dashed lines 94

5.43 Jet energy response in the central calorimeter using the MPF method and effects of corrections. 97

5.44 Jet energy response versus detector η using dijet P_T balance asymmetry. 99

5.45 Jet energy response versus detector η using dijet P_T balance and the MPF method. 101

5.46 Jet transverse energy resolution versus jet energy using the asymmetry for two regions of the detector. Actual data is compared to Monte Carlo resolution and the agreement is seen to be good. . . . 106

5.47 Jet energy resolution versus energy using the asymmetry for the central and crack region and Monte Carlo results for the end region. Resolution fits are shown for each region. 107

6.48 Acceptance versus χ for different mass ranges. 114

6.49 Acceptance versus χ for different mass ranges. 115

6.50 Nominal and upper and lower limits of slope of the jet response. . . 118

6.51 Comparison of angular distributions $dN/d\chi$ vs. χ using the simple definition $\eta^* = \frac{1}{2}(\eta_1 - \eta_2)$ and the Collins-Soper angle. Two different mass ranges are shown and no acceptance corrections have been made. 120

6.52 $dN/d\chi$ versus χ for $100 < M_{JJ} < 150$ distribution obtained using the Collins-Soper angle and compared to leading order QCD. 122

6.53 $dN/d\chi$ versus χ for $100 < M_{JJ} < 150$ distribution obtained using the simple definition $\eta^* = \frac{1}{2}(\eta_1 - \eta_2)$ compared to both leading order and next-to-leading order. 123

6.54 $dN/d\chi$ versus χ for $150 < M_{JJ} < 250$ distribution obtained using the Collins-Soper angle compared to leading order QCD. 124

6.55 $dN/d\chi$ versus χ for $150 < M_{JJ} < 250$ distribution obtained using the simple definition $\eta^* = \frac{1}{2}(\eta_1 - \eta_2)$ compared to both leading order and next-to-leading order. 125

6.56 $dN/d\chi$ versus χ for $250 < M_{JJ} < 350$. 127

6.57 $dN/d\chi$ versus χ for $350 < M_{JJ} < 450$. 128

6.58 $dN/d\chi$ versus χ for $450 < M_{JJ} < 550$. 129

6.59 $dN/d\chi$ versus χ for $M_{JJ} > 550$ GeV. 130

6.60 $dN/d\chi$ versus χ for $M_{JJ} > 450$ GeV. 132

6.61 $dN/d\chi$ versus χ for $M_{JJ} > 550$ GeV compared to $O(\alpha_s^2)$ QCD without a contact term and with $\Lambda_C = 0.9$ Tev and $\Lambda_C = 1.1$ TeV. . . . 134

6.62 $dN/d\chi$ versus χ for $M_{JJ} > 550$ GeV. (Top): Leading order QCD alone and the best-fit curve LO QCD plus a contact term using the momentum scale $Q = P_T/2$. (Bottom): Same but using NLO-derived scale $Q = M_{JJ}/4\cosh(0.7\eta^*)$ and leading order QCD. . . . 136

LIST OF TABLES

2.1 Squared matrix elements for leading order $2 \rightarrow 2$ subprocesses with appropriate spin and color factors. q and q' are separate flavors of quarks and $g_s^2 = 4\pi\alpha_s$. 36

5.2 Triggers used to acquire dijet data. See text for explanation of terms. 68

5.3 Trigger E_T thresholds and efficiencies. 74

5.4 Results of fitting $E_{measured}$ versus E_{actual} 82

5.5 Jet energy resolution fit parameters. 105

6.6 Mass ranges and triggers used to plot dijet angular distributions. . . 113

6.7 Results of fits of $O(\alpha_s^2)$ and $O(\alpha_s^3)$ QCD predictions to the data. χ^2 significance levels in % are shown. 131

6.8 Results of fits of $O(\alpha_s^2)$ QCD with a quark-quark contact term. Shown is χ^2 significance levels as a function of Λ_C. 133

ABSTRACT

Dijet angular distributions provide a excellent look at the interactions between partons. The measurements performed by the DØ detector are the most precise accomplished to date at $p\overline{p}$ colliders and cover a larger angular range than previously possible. Both leading order and next-to-leading order QCD calculations show agreement with the data over a large range in dijet invariant mass. This comparison is limited mainly by the large size of the theoretical uncertainties which are larger than the experimental uncertainties for some mass ranges. Additionally, a limit on quark compositeness of $\Lambda_C > 1.1$ TeV has been obtained.

CHAPTER 1

Introduction

Jet production was first observed at e^+e^- colliders in 1975. At $p\bar{p}$ colliders such as the Fermilab Tevatron, the production of jets is one of the fundamental processes observed in events with large transverse momentum. Jets are the observable remnants of the quarks and gluons (collectively known as partons) from hard scattering events. Measurements of the properties of jet events is a good test of the theory known as Quantum Chromodynamics, or QCD.

At lowest order, the QCD predictions refer to jet events in which a parton from each of the incoming hadrons participates in a collision that results in two outgoing final state partons. To a good approximation, the cross section for two jet events can be factorized into a term dependent on the parton distribution functions and another dependent on the center-of-mass scattering angle. Hence the angular distribution measurement is largely independent of the parton distribution uncertainty and directly related to the hard scattering matrix elements of QCD. The measurement is also sensitive to the strong coupling constant (a measure of the strength of the interaction between partons), α_s, and its dependence on the momentum transfer.

Currently, due to the difficulties in calculation, only leading order ($O(\alpha_s^2)$) and next-to-leading ($O(\alpha_s^3)$) order QCD calculations exist. The higher order prediction should be superior and in certain kinematical regions the difference between leading and next-to-leading order calculations is substantial enough for us to attempt to discriminate between the two.

The DØ detector is ideally suited to measurements of this type due to its excellent calorimetry which enables us to measure jet properties to high precision

over a large angular region. It is mainly the large region of uniform coverage and jet triggering ability that make our measurement of the dijet angular distribution superior to previous attempts.

The following chapters will expand the theoretical motivation behind this measurement and discuss in detail the experimental apparatus and issues such as jet energy calibration and resolution, jet triggering and acceptance, and data selection criteria. Finally, the results and conclusions will be presented.

CHAPTER 2

Theory

At the Fermilab Tevatron, protons are collided with antiprotons at a center-of-mass energy of 1.8 TeV, and jets are produced copiously. In this chapter we will explain how jets can be studied in order to gather some information about the processes which are governed by the theory known as Quantum Chromodynamics, or QCD.

Protons are made up of smaller particles called quarks which are held together by gluons. Quarks and gluons are collectively referred to as partons. It is these proton constituents which interact to generate an observable event. First we will review our understanding of the proton itself, knowledge that is essential since we must know the internal structure of the proton in order to predict which interactions will take place. Then we will review the QCD predictions for the dijet angular distributions for individual parton-parton subprocesses. Also the theoretical definition of a jet will be presented.

2.1 Parton Model

The proton is a fairly stable object, not prone to breaking apart easily. Yet, when probed by high energy particles, the partons that make it up are not locked rigidly together but rather appear to be connected in a very loose fashion. This apparent contradiction first came to light when the results of deep inelastic electron-proton scattering showed that the cross section for

$$e + P \rightarrow e + X$$

shown diagrammatically in Figure 2.1 could be expressed as a function of a single kinematic variable, x, the fraction of the proton momentum carried by the interacting quark[1]. In the massless approximation for electrons and quarks, the massless condition for the final quark gives

$$0 = k'^2 = (k+q)^2 = q^2 + 2k \cdot q.$$

Using $k = xP, q^2 = -Q^2$ and $P \cdot q = M\nu$ where Q^2 is the invariant momentum transfer squared, M is the proton mass and ν is the momentum carried by the virtual photon in the proton rest frame, we obtain

$$x = \frac{-q^2}{2P \cdot q} = \frac{Q^2}{2M\nu}.$$

Both Q^2 and $2M\nu$ are much greater than M^2 in deep inelastic scattering, making the time scale of the interaction very short compared to the lifetime of a virtual state of the proton, thereby justifying the treatment of the partons as free during the collision.

2.2 Renormalization and the Running Coupling

Renormalization is an elaborate process whereby infinities which occur when calculating Feynman diagrams are eliminated. It also introduces a parameter, μ, which embodies the uncertainties due to uncalculated higher order loops. The major result of renormalization is an expression for the strong coupling constant in terms of a momentum scale, Λ, which is given here in the one-loop (leading order) approximation[2]:

$$\alpha_s(Q^2) = \frac{12\pi}{(33-2f)\ln(Q^2/\Lambda^2)}$$

where f is the number of flavors contributing at a given Q^2 and Λ is the experimentally derived fundamental scale parameter of QCD. This shows that the strength of the coupling between partons, α_s, depends on the momentum scale of the particles involved. We see that for large values of Q^2, the coupling becomes small and

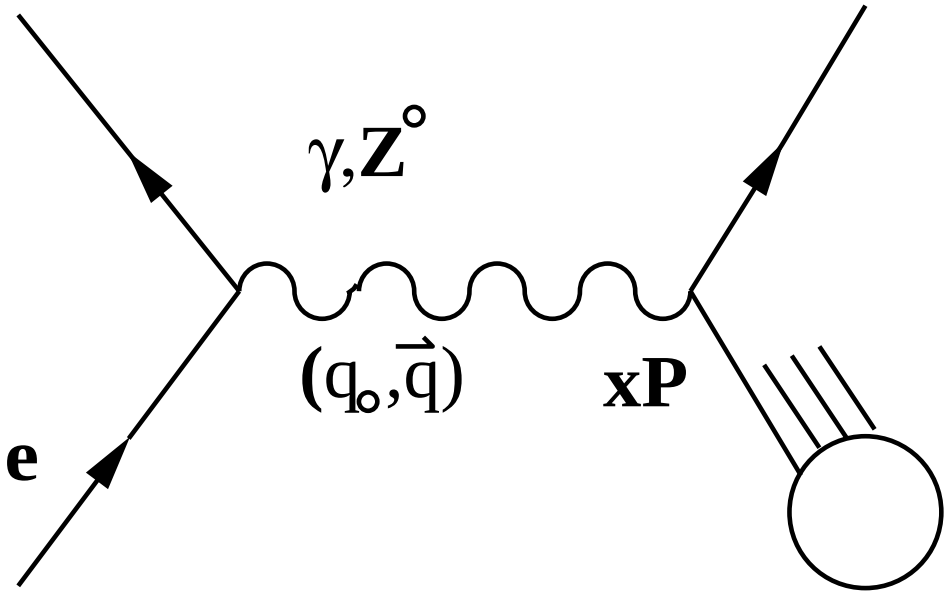

Figure 2.1: Deep inelastic electron-proton scattering.

perturbative calculations can be used. But for values of $Q \simeq \Lambda$, all orders of the theory contribute equally and perturbative calculations are useless. The value of Λ depends on the renormalization scheme used and the number of quark flavors involved. The currently accepted value of Λ is around 200 MeV, the exact value not being too critical. For measurable jet physics at the Fermilab Tevatron, α_s of the parton-parton scattering ranges from about 0.10 to 0.15, so that perturbative calculations may be used with reasonable accuracy.

The falling of $\alpha_s(Q^2)$ with increasing momentum scale is known as "asymptotic freedom" and explains the scaling result of deep inelastic scattering; that the partons scatter incoherently when interactions occur at short distances and short times. The increase of the strong coupling at low momentum scales (longer times and distances) is called "confinement" and is what keeps the proton together under normal circumstances. The phenomenological description of jets as a spray of collimated hadrons is also predicted by the increase of the coupling at large distances.

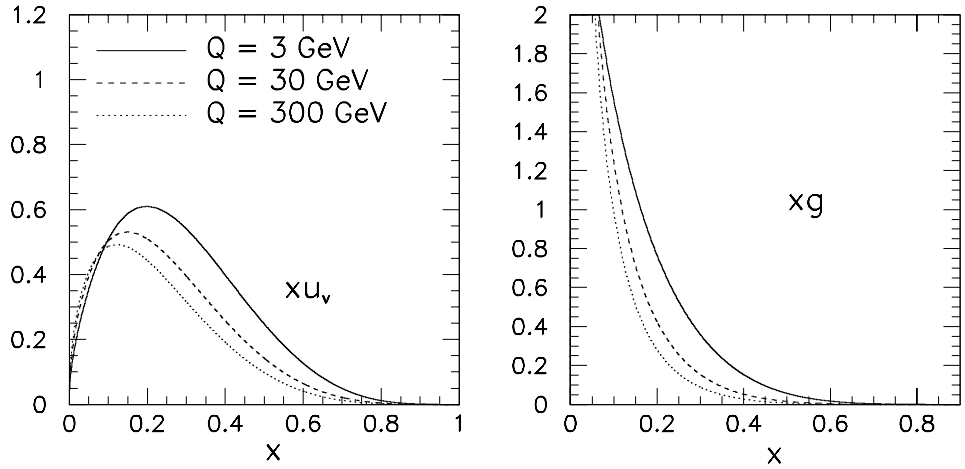

Figure 2.2: Parton distribution functions weighted with x for the u valence quark and the gluon shown for different values of Q. The distribution MRS S0 is used.

The momentum scale also comes into play when we try to describe the structure of the proton. As we probe it deeper, we see not only the valence quarks that nominally make up the proton, but also a sea of gluons, quarks and anti-quarks. The equations governing the evolution of the protons structure with Q^2 are called the Altarelli-Parisi equations [3]. They predict a logarithmic dependence on Q^2 of the momentum fraction distribution of the partons. At higher Q^2, the distribution gets softer, which can be explained by an increased likelihood that a quark has just radiated a gluon. This is shown in Figure 2.2 where the gluon and u valence quark distributions are shown for several values of Q. As Q increases, the distributions tend toward lower x (the fraction of the proton's momentum carried by the parton.) This "evolution" of the momentum distribution functions gives violations of the deep inelastic scaling that become observable only when a large kinematic range is studied, due to the logarithmic dependence on Q^2.

2.3 Parton Distribution Functions

Since we are dealing with proton-antiproton collisions and we have theoretical predictions for parton-parton subprocesses, we must have some knowledge of how much contribution a given parton makes to the total momentum of the proton. The parton distribution functions (PDF), $f_q(x)$ give the probability that a given parton, q, carries momentum fraction x. The PDF's are calculated based on experimental data. Deep inelastic scattering of electrons and muons off protons can give the quark distributions, but gluons, which have no electroweak coupling, are not measured by this method. Gluon distributions can be probed by direct photons or Drell-Yan lepton pairs from a quark-gluon interaction, but current measurements are of limited usefulness and do not extend to low values of x, where the gluon density gets very large. Several constraints are placed on the distributions:

$$\int_0^1 u_v(x)dx = 2$$

$$\int_0^1 d_v(x)dx = 1$$

$$\int_0^1 xdx[g(x) + \sum_{q,\bar{q}}[q(x) + \bar{q}(x)]] = 1$$

simply that there be 2 valence u quarks, 1 valence d quark, and the momentum of all the partons add up to the momentum of the proton. Using these constraints, experimental results, and the previously mentioned Altarelli-Parisi equations the parton distribution functions and their Q^2 dependencies can be generated by fitting the parameters of some assumed form. Most of the experimental measurements were done at low values of Q, from 4-10 GeV, so that evolution up to the current experimental scale is essential.

Many sets of PDF's exist, each using different experimental results, renormalization schemes, and fitting methods. Also, some sets use the leading order α_s calculation while others use the next-to-leading order evolution. Two are shown in Figure 2.3 evolved up to a scale $Q^2 = (50 \text{ GeV })^2$. Using PDF's, we may now

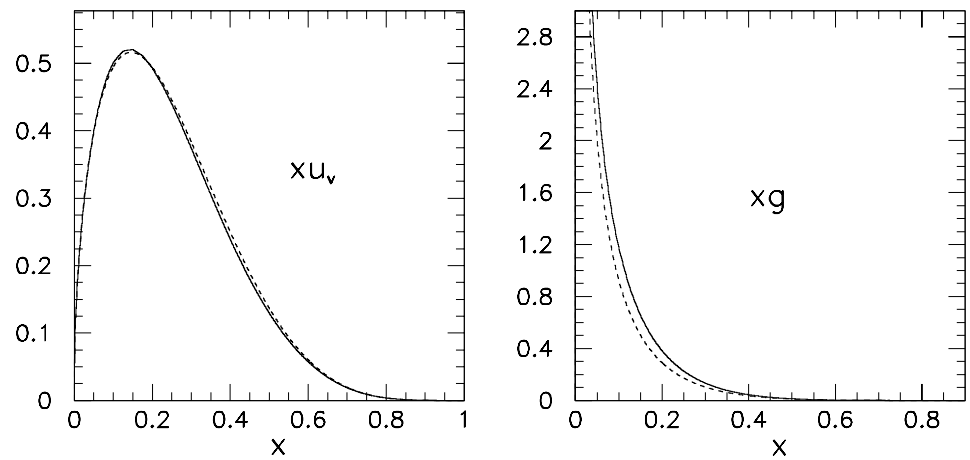

Figure 2.3: Parton distribution functions weighted with x for the gluon and the u valence quark. Two different distributions are shown: set MRS S0 (solid line) and set Morfin-Tung B2 (dotted line) at $Q^2 = (50GeV)^2$.

finally calculate cross-sections for proton-antiproton collisions by summing over all the possible initial partons and integrating over the x for each one:

$$\sigma(p\bar{p} \to jet + jet) = \sum_{a,b} \iint dx_a dx_b f_{a/p}(x_a) f_{b/\bar{p}}(x_b) \hat{\sigma}(ab \to jet + jet).$$

Where a and b are the initial state partons, $\hat{\sigma}$ is the subprocess cross-section.

2.4 Jet Production

The production of jets in hadron-hadron collisions can be reduced to three steps, the perturbative hard interaction, the perturbative but difficult-to-calculate parton showering, and the non-perturbative "hadronization" or "fragmentation". These steps will be discussed separately since they are handled in completely different ways.

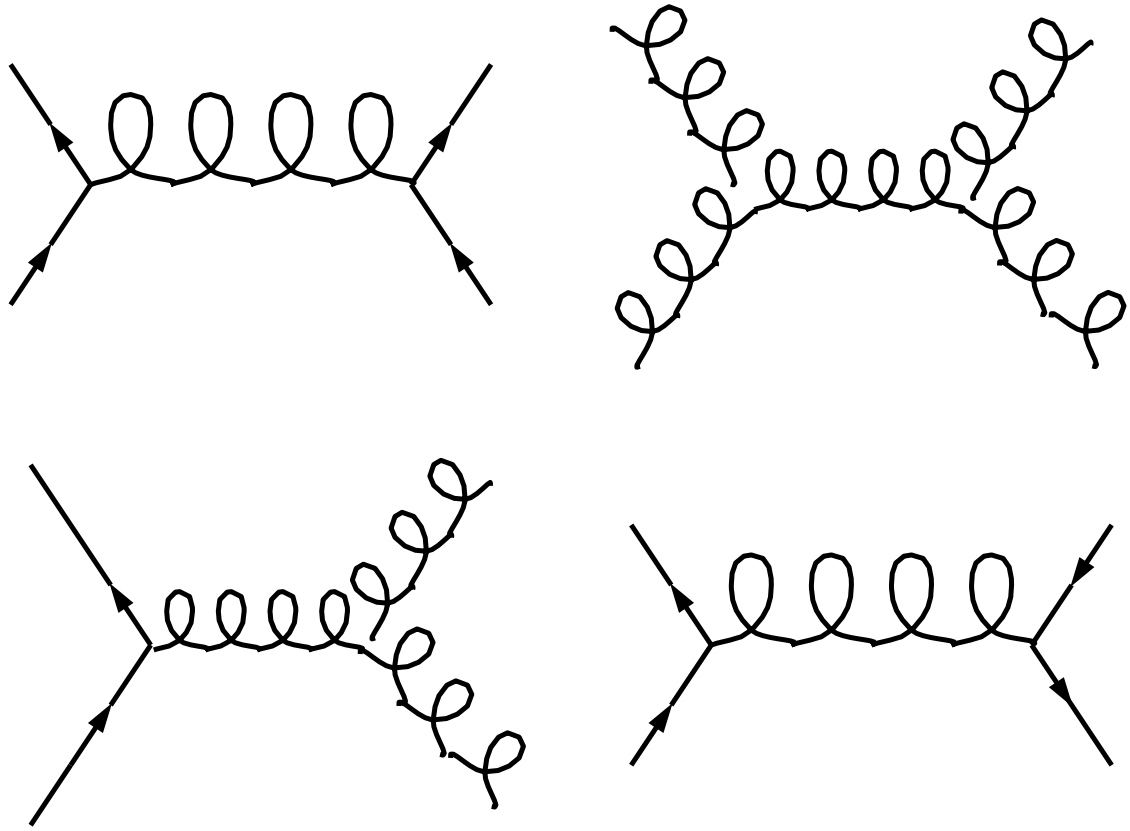

Figure 2.4: Feynman diagrams for parton-parton scattering to order α_s^2.

2.4.1 The hard interaction

The QCD hard-scattering predictions are derived directly from the theory, and these are what we hope to measure experimentally. The accuracy of the test is limited by the difficulty in calculating higher order terms in the perturbation theory. Leading-order ($O(\alpha_s^2)$) calculations are derived from the Feynman diagrams of Figure 2.4. Leading order subprocess predictions are presented in § 2.6.2.

Next-to-leading-order ($O(\alpha_s^3)$) calculations have become available in recent years [4] and have increased our predictive accuracy. Examples of next-to-leading-order diagrams are shown in Figure 2.5. These predictions increase the theoretical accuracy by including possible third jets, but also cause additional difficulties in

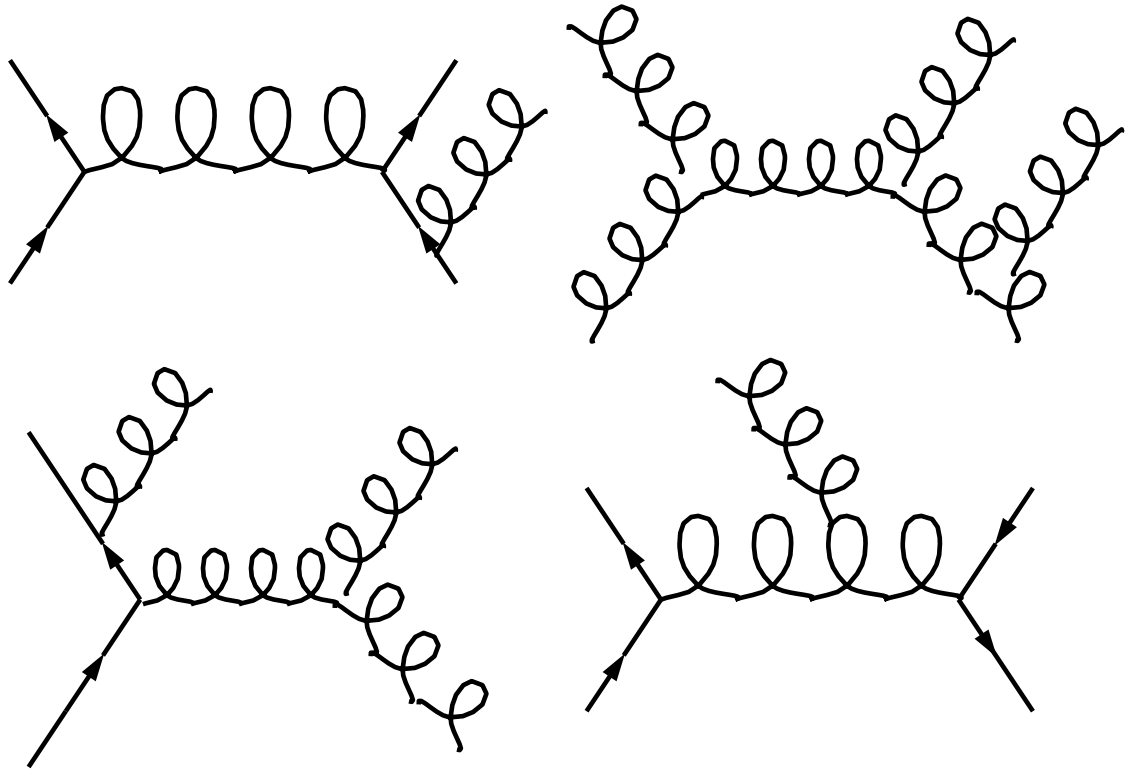

Figure 2.5: Examples of α_s^3-order processes.

jet definition. This problem will be discussed more fully in § 2.5.

The value of Q (the momentum transfer) used in α_s^2 and the parton distribution evolution is normally chosen as some fraction of the outgoing parton P_T. Uncertainties in the scale μ lead to uncertainties in what fraction of P_T to use, for instance, $Q^2 = (P_T/2)^2, (P_T)^2, (2P_T)^2$, etc. Since μ is related to the uncertainty due to missing higher orders, $O(\alpha_s^2)$ calculations depend on this choice more strongly than do $O(\alpha_s^3)$ calculations.

2.4.2 Parton Showering

At this stage we have 2 (or 3) partons moving at high momentum transverse to the initial beam momentum. As the partons move apart the time and distance

scales increase causing the coupling to strengthen (See Figure 2.6.) The quarks and gluons from the original collision begin radiating gluons and the gluons can also split into quark-antiquark pairs. This is called the parton shower. At early times in the shower, the parton invariant masses are large and gluons may be emitted at large angles. Later in the shower the invariant masses decrease and the "gluon bremmstrahlung" is collinear. The parton shower is perturbative, and although the exact higher order matrix elements have not been calculated, the process may be simulated using using a so-called "leading-log" approximation where all the terms $\alpha_s^n \ln^n Q^2$ are summed. Events can be generated which have multi-jet characteristics, but the approximation is poor for early times when Q^2 (equals invariant mass) is large and interference effects (left out with the non-leading-log terms) are important. Leading-log approximations will be used here to generate Monte Carlo simulated events, but data will be compared only to $O(\alpha_s^2)$ and $O(\alpha_s^3)$ theoretical predictions.

It is important to note that the partons can radiate before the hard collision as well. This initial state radiation will take part in the parton showering after the collision as will the remnants of the proton and antiproton, which will shower and hadronize into the so-called "beam jets."

2.4.3 Hadronization

When the invariant masses drop to order Λ, α_s becomes large, and non-perturbative hadronization takes over. This process is characterized by a fragmentation function $\mathcal{D}_h^k(z, Q^2)$, the probability of finding a hadron of type h with momentum fraction $z = 2E_h/Q$ where k is the initiating parton type. Various models using fragmentation functions have been incorporated into event generator Monte Carlos.

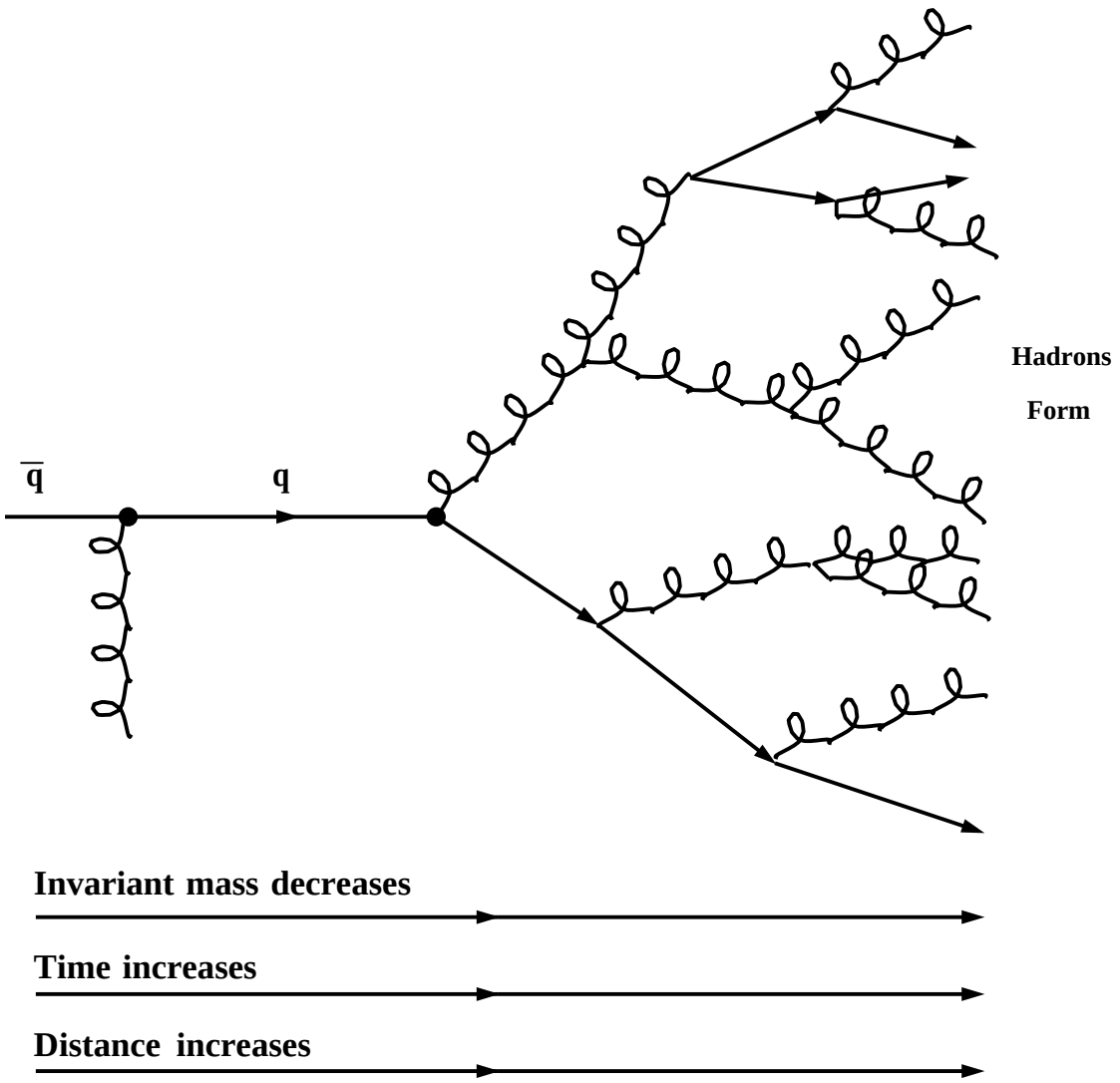

Figure 2.6: Schematic of the development of a parton shower. The time and distance increase from left to right while the invariant mass decreases. Hadrons form when the masses become of the order of Λ, the QCD scale parameter.

2.5 Jet Definition

When dealing with leading order $2 \rightarrow 2$ processes, the outgoing partons are widely separated and the jet's 4-momentum is equated with the 4-momentum of the partons. With next-to-leading-order calculations, where 3 outgoing partons are possible, it is more tricky. As we have seen, the parton showering and hadronization processes tend to widen jets, so that if two of the outgoing partons are close together, they will be experimentally unresolvable and appear as a single jet. If we are to compare experimental results to theory, then these partons must be merged into a single object. Also, theoretical divergences occur as the radiated parton's energy become small ("infrared divergence") or the angle between it and the parent parton become small ("collinear divergence".) They can removed by requiring some separation distance cutoff parameter.

The question then arises as to what constitutes "close." To answer this we must first define the rapidity:

$$y = \frac{1}{2}\ln(\frac{E+p_z}{E-p_z}) = \tanh^{-1}(\frac{p_z}{E})$$

and the pseudorapidity:

$$\eta = -\ln\ \tan(\theta/2)$$

where the z-axis is defined along the beam line (initial parton direction) and θ is the angle between the parton (or jet) and the z-axis. The pseudorapidity is easily measured experimentally and approaches the rapidity in the limit $p \gg m$. It is a very useful variable since under a boost $\beta = v/c$ in the z-direction, the rapidity transforms like $y \rightarrow y + \tanh^{-1}\beta$. Hence distributions in rapidity such as jet shapes are invariant under longitudinal boosts. This variable along with the azimuthal angle ϕ are used to define distances between partons.

The $O(\alpha_s^3)$ predictions of Ellis, Kunszt, and Soper[4] used here to compare with data do indeed merge partons into jets when they are too close in y, ϕ-space. They also make use of the parton's transverse momentum, P_T, the momentum component perpendicular to the beam line. The criteria they use is to merge the

partons if they are both inside a cone (circle in y, ϕ-space) with a P_T-weighted centroid: If

$$\sqrt{(y_1 - y_2)^2 + (\phi_1 - \phi_2)^2} \leq \frac{(P_{T_1} + P_{T_2})\, R}{\max(P_{T_1}, P_{T_2})}$$

then the two partons are merged into a single jet with

$$P_{T_J} = P_{T_1} + P_{T_2}$$

and

$$y_J = \frac{y_1 P_{T_1} + y_2 P_{T_2}}{P_{T_J}} \qquad \phi_J = \frac{\phi_1 P_{T_1} + \phi_2 P_{T_2}}{P_{T_J}}.$$

The nominal size of the cone, R, is the cutoff parameter mentioned above. The theoretical results are dependent on R and its value can be chosen experimentally in consultation with detector resolution and the normal jet width due to parton showering and hadronization. This topic will be discussed further in §4.1.

2.6 Dijet Angular Distributions

2.6.1 Definition of Angular Variables

There are 3 independent variables used here to describe dijet events, M_{JJ}, the dijet invariant mass, η_{boost}, the longitudinal boost in rapidity, and $\cos\theta^*$, the cosine of the angle between a parton and the beam line in the center-of-mass frame. These variables are shown schematically in Figure 2.7. It should be noted that since we are experimentally unable to differentiate between θ^* and $\pi - \theta^*$, what we actually measure is $|\cos\theta^*|$. An implicit absolute value is assumed for all angular variables.

In the simple dijet case, if the pseudorapidities of the two jets are η_1 and η_2, then the center-of-mass pseudorapidity is $\eta^* = \frac{1}{2}(\eta_1 - \eta_2)$. This is related to θ^* by this equation:

$$\cos\theta^* = \tanh\eta^*.$$

The longitudinal boost of the dijet system can be expressed in terms of the two jet η's as well:

$$\eta_{boost} = \frac{1}{2}(\eta_1 + \eta_2).$$

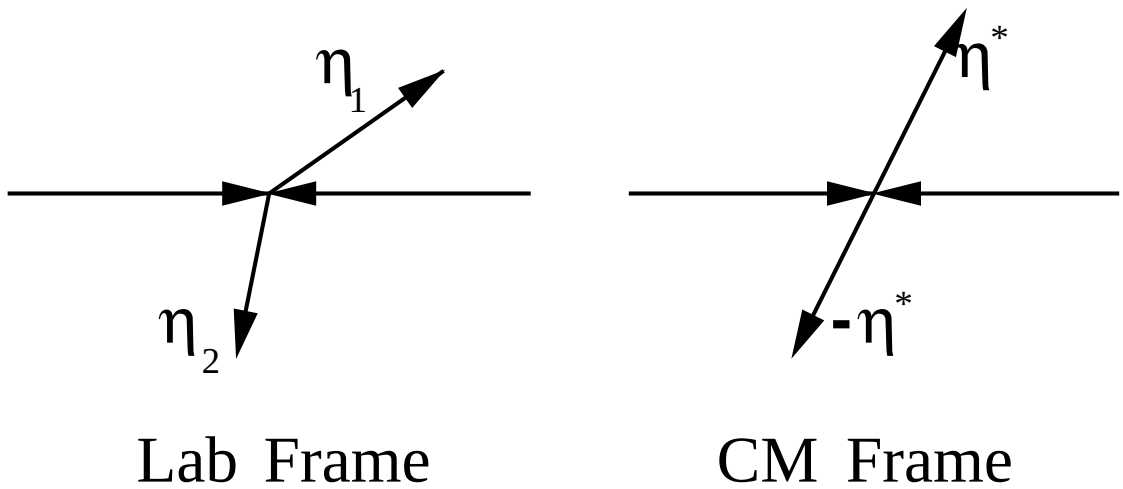

Figure 2.7: Dijet event in lab frame and center-of-mass frame.

The dijet mass, M_{JJ}, is calculated using $M_{JJ}^2 = (P_1 + P_2)^2$, where the P's are the jet's 4-momenta. In this simple dijet case where there is no transverse boost (i.e., the two jet P_T's are equal) then $M_{JJ} = 2P_T \cosh \eta^*$.

Jet production is dominated by t-channel exchange of a vector gluon between partons, which gives the characteristic angular distribution known as Rutherford scattering at larger angles. This distribution $d\sigma/d\cos\theta^* \sim (1 - \cos\theta^*)^{-2}$ is strongly peaked in the forward direction. Figure 2.8 shows both a pure Rutherford scattering distribution and a leading order QCD calculation normalized over the range in $\cos\theta^*$ shown. Figure 2.9 shows the same two curves versus η^*.

The variable χ will also be used here. Although it is not easily visualized in terms of physical coordinates, it tends to flatten the distributions and makes the various contributions and differences more easily observable. It is defined by:

$$\chi = e^{2|\eta^*|}$$

or

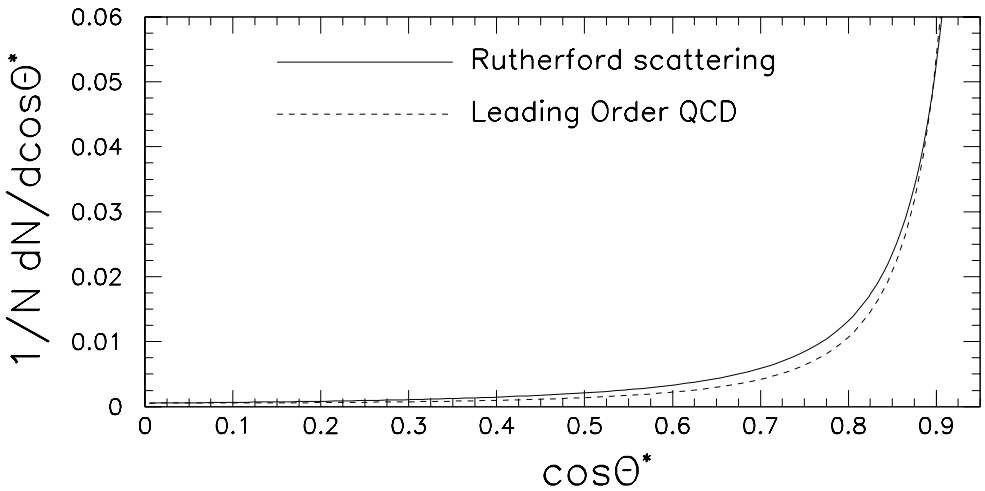

Figure 2.8: $dN/d\cos\theta$ for pure Rutherford scattering (solid line) and for leading order QCD dijets (dashed line) .

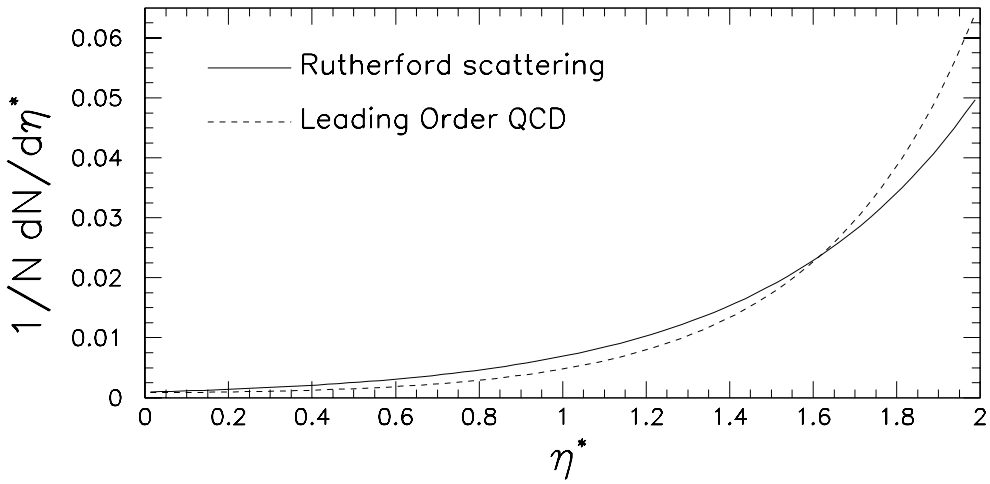

Figure 2.9: $dN/d\eta^*$ for pure Rutherford scattering (solid line) and for leading order QCD dijets (dashed line) .

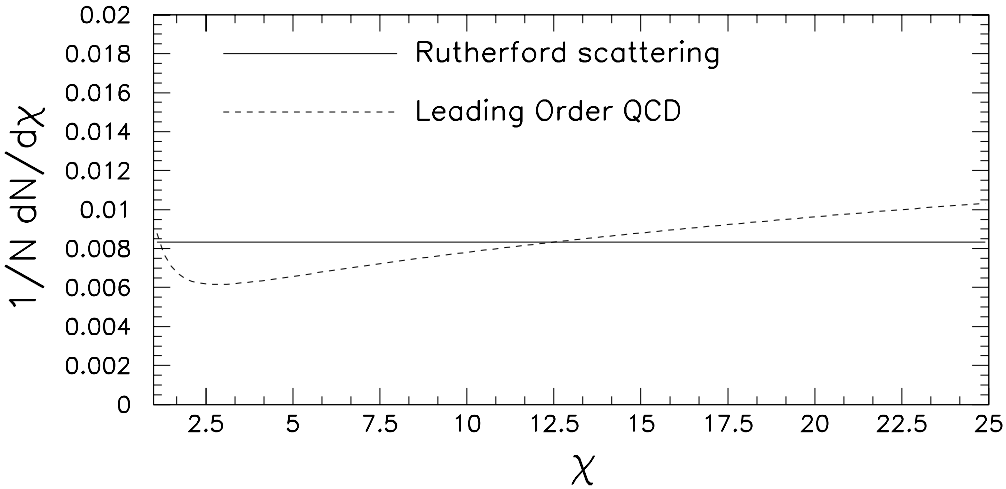

Figure 2.10: $dN/d\cos\eta$ for pure Rutherford scattering (solid line) and for leading order QCD dijets (dashed line) .

$$\chi = \frac{1+\cos\theta^*}{1-\cos\theta^*}.$$

Using χ, The Rutherford scattering distribution can be written as

$$\frac{d\sigma}{d\chi} = \frac{d\sigma}{d\cos\theta^*}\frac{d\cos\theta^*}{d\chi} \sim \left(1-\frac{\chi-1}{\chi+1}\right)^{-2}\left(\frac{1}{\chi+1}-\frac{\chi-1}{(\chi+1)^2}\right)$$

$$= \left(\frac{2}{\chi+1}\right)^{-2}\frac{2}{(\chi+1)^2} = \frac{1}{2}$$

using $\cos\theta^* = (\chi-1)/(\chi+1)$. Thus the distribution in χ is completely flat for pure Rutherford scattering. In Figure 2.10 the QCD leading order curve (same as used in Figure 2.8 and Figure 2.9) is shown plotted versus χ and it is clearly not completely flat at large χ. This discrepancy between leading order QCD and pure Rutherford scattering will be explained in the next section.

Experimentally, there are often non-negligible transverse boosts due to the transverse momentum components of the partons inside the proton and additional

low P_T jets. The definition shown above,

$$\cos\theta^* = \tanh(\frac{1}{2}(\eta_1 - \eta_2)),$$

assumes the dijet system is boosted along the beam axis only. Using this definition for dijet masses below around 200 GeV, the dijet transverse boosts (typically around 10 GeV) could smear the observed angular distribution, thereby flattening it slightly. The "Collins-Soper" angle[5], which determines the center-of-mass scattering angle along a general boost vector, may provide better agreement with leading order predictions. The definition is:

$$\cos\theta^* = \frac{(E_1 + P_{z1})(E_2 - P_{z2}) - (E_1 - P_{z1})(E_2 + P_{z2})}{M_{JJ}\sqrt{M_{JJ}^2 + \vec{Q_T^2}}}$$

where

$$\vec{Q_T^2} = (\vec{P_{T1}} + \vec{P_{T2}})^2 = (P_{x1} + P_{x2})^2 + (P_{y1} + P_{y2})^2.$$

Additionally, due to transverse boosts, the experimental dijet mass will be calculated using the general definition,

$$M_{JJ} = (P_1 + P_2)^2 = (E_1 + E_2)^2 - (P_{x1} + P_{x2})^2 - (P_{y1} + P_{y2})^2 - (P_{z1} + P_{z2})^2.$$

The derivation of the 4-vectors involved in the calculation will be explained in §4.1.1.

2.6.2 Calculation of $dN/d\chi$ in Leading Order

The leading order matrix elements are calculated using Feynman diagrams such as those in Figure 2.4. The individual subprocesses have been symmetrized and combined for inclusive final states and represented in terms of χ in Table 2.1[6]. In Figure 2.11, the subprocess matrix elements are plotted in the form $\frac{|\mathcal{M}|^2}{g_s^4}\frac{1}{(\chi+1)^2}$, thereby showing only the explicit χ dependence and color factor differences. Note that they are all quite similar in shape, making the contribution of quarks relative to gluons of little importance. Therefore we expect the full distributions to be mostly independent of the choice of parton distribution.

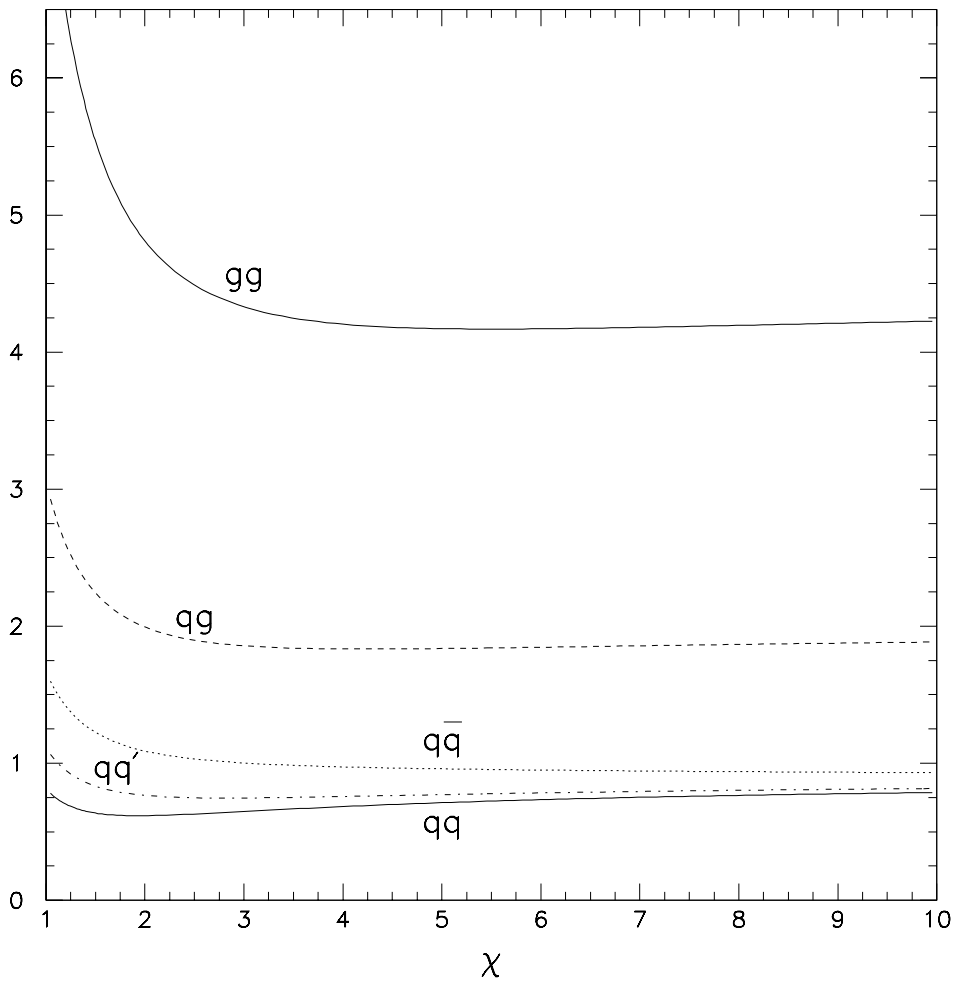

Figure 2.11: Subprocess matrix elements χ-dependence $= \frac{|\mathcal{M}|^2}{g_s^4}\frac{1}{(\chi+1)^2}$.

Table 2.1: Squared matrix elements for leading order $2 \to 2$ subprocesses with appropriate spin and color factors. q and q' are separate flavors of quarks and $g_s^2 = 4\pi\alpha_s$.

Subprocess	$\lvert\mathcal{M}\rvert^2/g_s^4$
$qq', q\bar{q}' \to jj$	$\frac{8}{9}(\chi^2 + \chi + 1 + \chi^{-1} + \chi^{-2})$
$qq \to jj$	$\frac{8}{9}(\chi^2 + \frac{2}{3}\chi + \frac{1}{3} + \frac{2}{3}\chi^{-1} + \chi^{-2})$
$q\bar{q} \to jj$	$\frac{8}{9}(\chi^2 + \frac{8}{3}\chi + \frac{2}{3} + \frac{8}{3}\chi^{-1} + \chi^{-2} - \frac{(\chi^2+1)}{(\chi+1)^2})$
$qg \to jj$	$2(\chi^2 + \frac{11}{9}\chi + \frac{5}{3} + \frac{11}{9}\chi^{-1} + \chi^{-2})$
$gg \to jj$	$\frac{9}{2}(\chi^2 + \frac{29}{27}\chi + 3 + \frac{29}{27}\chi^{-1} + \chi^{-2} - \frac{\chi}{(\chi+1)^2}) - \frac{3}{4}\frac{(\chi^2+1)}{(\chi+1)^2}$

The curves flatten as expected at large χ where the t-channel contribution dominates. The sharp rise at low χ (which is also low $\cos\theta^*$) is due partly to s-channel contributions which are only visible above the large t-channel cross section where the jets are nearly perpendicular to the beam line (in the CM frame). This corresponds to $\chi < 3$ or $|\theta^*| < 60$ degrees or $|\eta^*| < .5$.

To generate an observable distribution we must now sum over these subprocess matrix elements weighted with parton distribution functions and multiply by appropriate phase space factors. This can be written as follows:

$$\frac{d\sigma^3}{d\eta_{boost} dM_{JJ} d\chi} = \frac{1}{128\pi E_{beam}} \frac{E_T^2}{\chi M_{JJ}} \sum_{a,b} f_a(x_a, Q^2) f_b(x_b, Q^2) |\mathcal{M}_{ab}|^2$$

where a, b are the initial state partons, E_T is the parton transverse energy and E_{beam} is the initial proton(antiproton) energy in the lab frame. In order to generate $d\sigma/d\chi$, integrate η_{boost} and M_{JJ} over the ranges of interest. All the plots have been normalized to unity over the region of interest. This normalization reduces the largest source of experimental uncertainty, the jet energy scale uncertainty, and makes the measurement sensitive to differences in shape. Results are shown in

Figure 2.12 for the parton distribution functions MRS S0[7], Morfin-Tung B2[8], and CTEQ 1M [9] using $Q^2 = P_T^2/4$. As expected, little variation is seen due to differing PDF's. For all ranges of M_{JJ} and χ within experimental reach the differences between curves generated using different parton distributions is of order 2% or less.

The subprocess χ distributions tended to flatten at larger χ (Figure 2.11) in agreement with pure Rutherford scattering. However, the full distributions shown in Figure 2.12 keep rising. This is due to two factors, both related to the running of α_s with Q^2, which is proportional to P_T^2. For constant M_{JJ}, or range of M_{JJ} such as used here, the jet P_T decreases as χ increases. This may be seen from the equation shown above, $M_{JJ} = 2P_T \cosh \eta^*$, which may be rewritten as:

$$P_T = \frac{M_{JJ}}{2\cosh \eta^*} = \frac{M_{JJ}}{\sqrt{\chi} + 1/\sqrt{\chi}}.$$

The two effects which cause the rise in the distribution at large χ are:

- The parton distributions get harder (tends to higher x) as Q^2 decreases. This increases the number of partons available to scatter at higher χ.
- The matrix elements contain a factor $\alpha_s^2(Q^2)$ which increases as Q^2 decreases.

Since the rise of the distribution at large χ is due to the running of α_s, we may be sensitive to the choice of momentum scale used. Shown in Figure 2.13 is the distribution using CTEQ 1M and varying the choice of Q^2 over the range: $Q^2 = P_T^2/4,\ P_T^2,\ 4P_T^2$. The distribution is seen to be sensitive at about the 3% level to choices in this range. Since the choice of momentum scale effects the slope of the curve, as the χ range increases the sensitivity to the choice of scale increases.

2.6.3 Next-to-Leading-Order Calculation of $d\sigma/d\chi$.

Calculation of the dijet angular distribution to order α_s^3 is far more difficult than for leading order. There are very many more Feynman diagrams to add up and the subprocess expressions are much more complex– they will not be reproduced here.

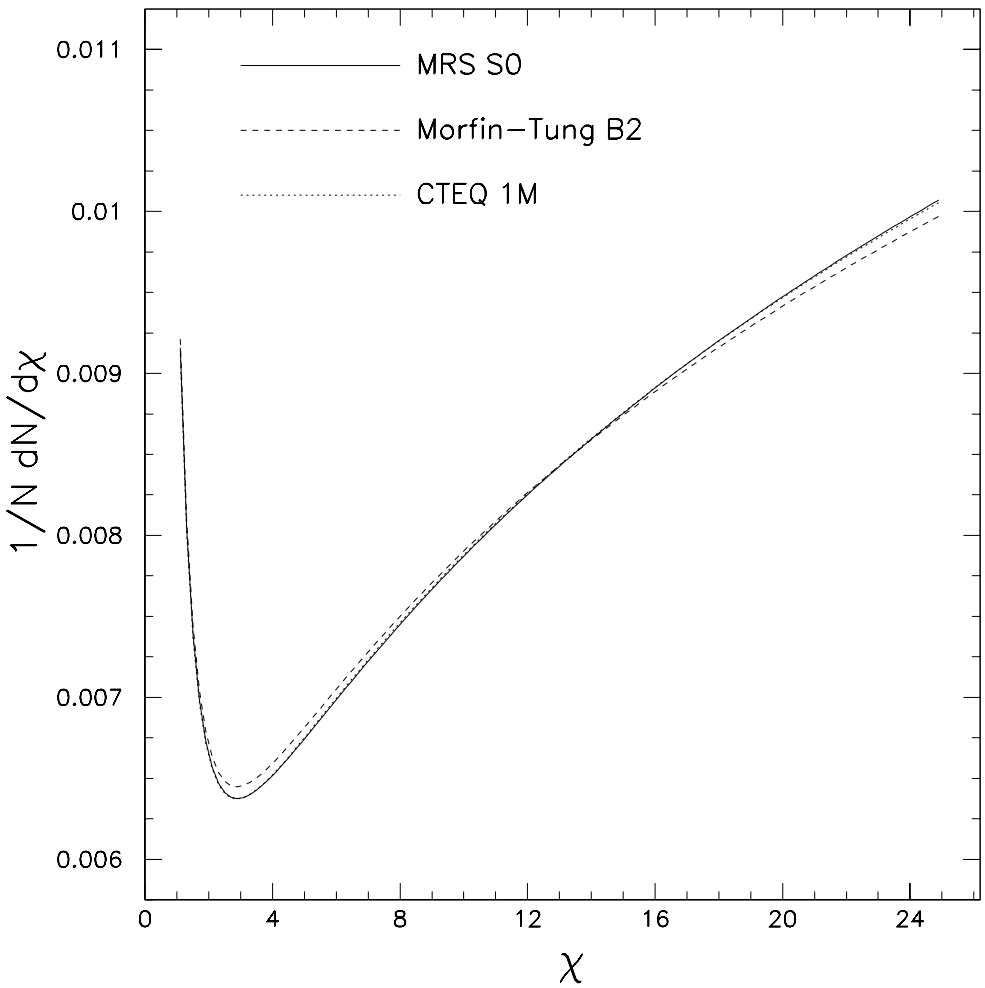

Figure 2.12: Calculated $d\sigma/d\chi$ for $200 < M_{JJ} < 400$ and $|\eta_{boost}| < 2.0$ using $Q^2 = P_T^2/4$. The parton distribution functions MRS S0(solid), M-T B2(dashed) and CTEQ 1M(dotted) are used and the curves have been normalized over the range shown in χ.

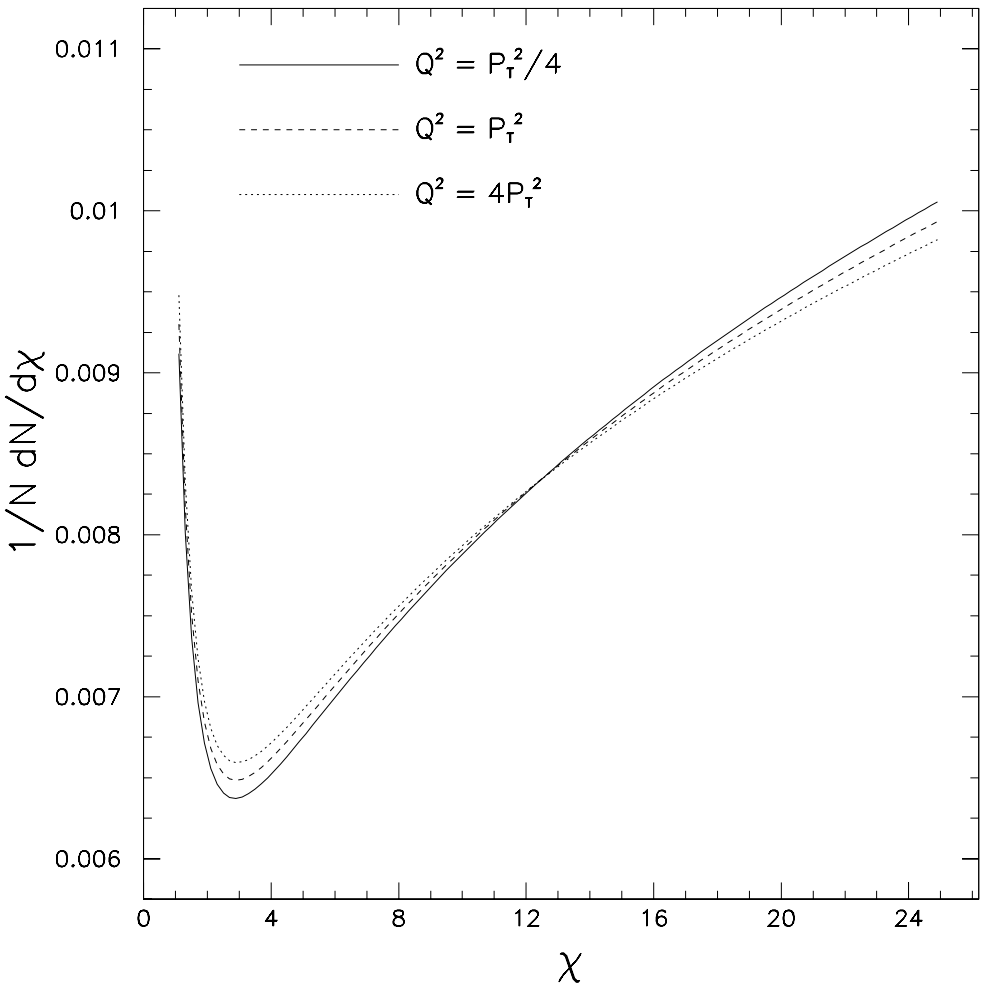

Figure 2.13: Calculated $d\sigma/d\chi$ for $200 < M_{JJ} < 400$ and $|\eta_{boost}| < 2.0$ using CTEQ 1M. Different values of $Q^2 = P_T^2/4$(solid), P_T^2(dashed), $4P_T^2$(dotted) have been used and the curves have been normalized.

Calculations have been performed by Ellis, Kunszt, and Soper [4] using the matrix elements provided by Ellis and Sexton[10] and they have been made available for this analysis via a computer program from Dave Soper. In the $O(\alpha_s^3)$ case, the two highest P_T final partons (if there are three) are used to calculate the kinematic parameters, M_{JJ}, η_{boost}, and χ. The choice of momentum scale is different also. Using a modified Principle of Minimal Sensitivity, Ellis, Kunszt, and Soper[11] use the following parameterization:

$$Q = \frac{AM_{JJ}}{2\cosh(B\eta^*)}$$

where A and B are chosen in order to minimize the derivative of the result with respect to Q. In other words, for some choice of A and B, variations of Q about this choice will minimally effect the resultant cross section. This choice is $A = 0.5$ and $B = 0.7$. Note that if $B = 1$ in the above formula, it is equivalent to $Q = AP_T$ and that the parameter B effectively controls the rate at which Q varies as a function of the angular variable. If we use this choice of Q in the leading order calculation, we get very nearly the same curve as the next-to-leading order prediction as expected. In Figure 2.14 the $O(\alpha_s^2)$ and $O(\alpha_s^3)$ distributions are compared and the slope is seen to be less steep for the $O(\alpha_s^3)$ QCD distribution. Ellis, Kunszt, and Soper claim an uncertainty of 10% [11] for the $O(\alpha_s^3)$ curve and 40% for the $O(\alpha_s^2)$ curve due to the uncertainty in the choice of momentum scale.

2.6.4 Effects of Compositeness

The dijet angular distribution can be used to test for new physics. It is sensitive to the presence of composite quarks, i.e., quarks that are made up of smaller, as yet unknown, particles. In high-P_T quark-quark scattering, these quark constituents could be exchanged and give rise to point-like interactions. Calculations are usually made assuming color-singlet isoscalar exchanges between left-handed u and d quarks, which can be expressed by the addition of the effective Lagrangian[12]

$$\mathcal{L} = \frac{\eta g^2}{2\Lambda_C^2}(\bar{u}_L\gamma^\mu u_L + \bar{d}_L\gamma^\mu d_L)(\bar{u}_L\gamma_\mu u_L + \bar{d}_L\gamma_\mu d_L)$$

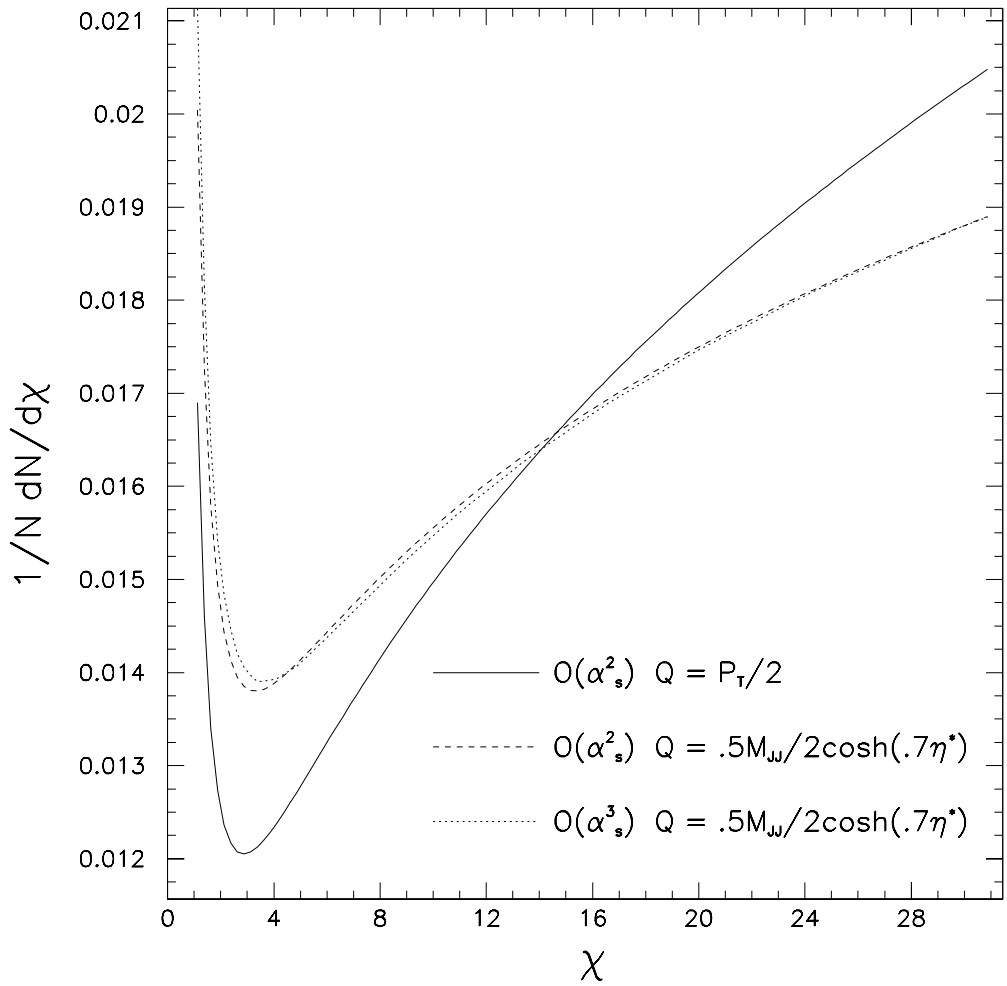

Figure 2.14: Calculated $d\sigma/d\chi$ for $200 < M_{JJ} < 400$ and all values of η_{boost} for $O(\alpha_s^2)$ and $O(\alpha_s^3)$ QCD calculations. The $O(\alpha_s^3)$ curve is flatter at high χ. The leading order prediction is shown for two choices of the momentum scale, $Q = P_T/2$ and $Q = .5M_{JJ}/2\cosh(0.7\eta^*)$.

to the QCD Lagrangian. This is often referred to as a contact term or 4-point interaction. Here Λ_C is the scale of compositeness and $\eta = \pm 1$ is the sign (phase.) The matrix elements are then modified by the addition of the following $|\mathcal{M}|^{*2}$ terms:

$$|\mathcal{M}(q\bar{q} \to q\bar{q})|^{*2} = -\frac{8}{9}\frac{4\pi\eta g_s^2 M_{JJ}^2}{\Lambda_C^2}\frac{\chi^3}{(\chi+1)^2} + \frac{8}{3}\left(\frac{4\pi\eta M_{JJ}^2}{\Lambda_C^2}\right)^2 \frac{\chi^2}{(\chi+1)^2}$$

$$|\mathcal{M}(qq \to qq)|^{*2} = -\frac{8}{9}\frac{4\pi\eta g_s^2 M_{JJ}^2}{\Lambda_C^2} + \left(\frac{4\pi\eta M_{JJ}^2}{\Lambda_C^2}\right)^2 \left(\frac{\chi^2+1}{(\chi+1)^2} + \frac{2}{3}\right)$$

$$|\mathcal{M}(qq' \to qq')|^{*2} = |\mathcal{M}(q\bar{q} \to q'\bar{q}')|^{*2} = |\mathcal{M}(q\bar{q}' \to q\bar{q}')|^{*2} = \left(\frac{4\pi\eta M_{JJ}^2}{\Lambda_C^2}\right)^2 \frac{\chi^2}{(\chi+1)^2}$$

These additional terms can be included in the $O(\alpha_s^2)$ calculation above to see the results of the contact term in the χ distribution. The results are shown in Figure 2.15 for $500 < M_{JJ} < 600$ with and without a compositeness scale of $\Lambda_C = 1000$ GeV, $\eta = +1$, and normalized to unity. The contact term is seen to increase the peak at low χ. Also note that since the added terms have factors of M_{JJ}/Λ_C, the higher the M_{JJ} range selected, the more sensitive we are to higher Λ_C. But due to the rapidly falling cross section, the statistical uncertainties increase as the mass threshold increases.

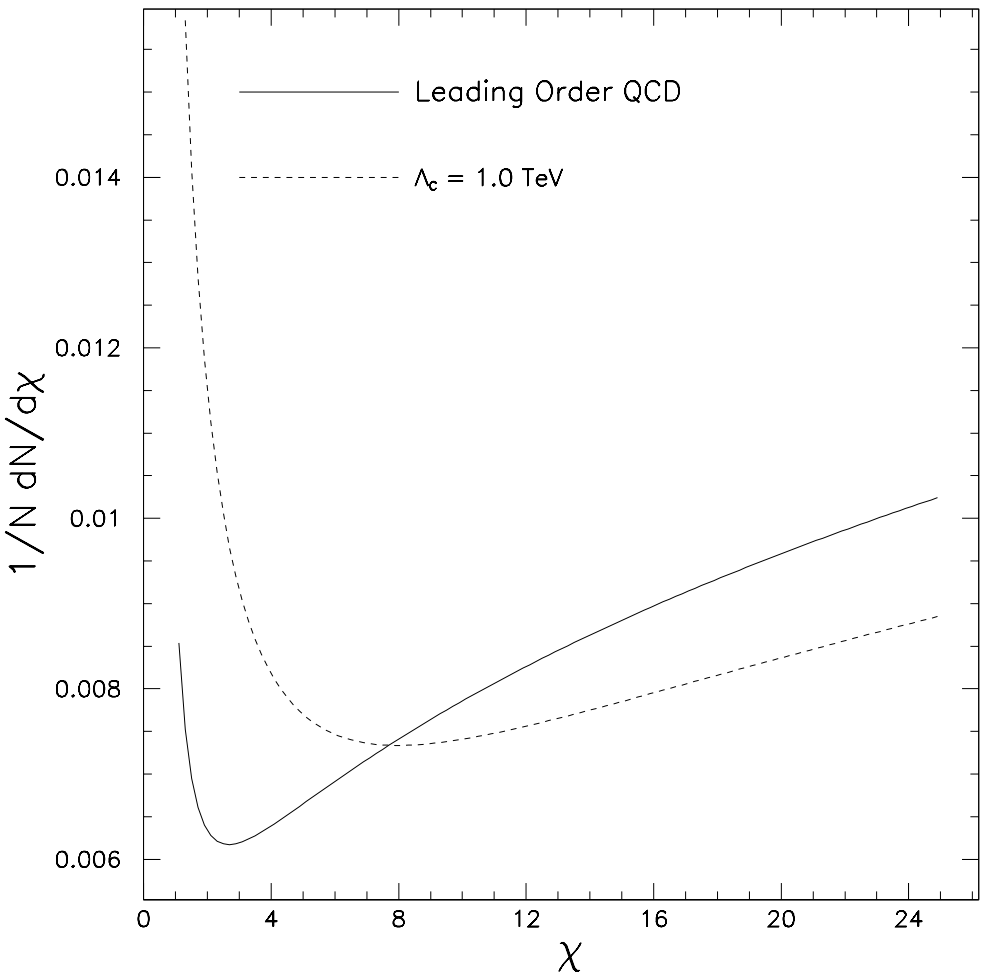

Figure 2.15: Calculated $d\sigma/d\chi$ using $O(\alpha_s^2)$ QCD for $M_{JJ} > 500$ with and without the contact term. The compositeness scale used is $\Lambda_C = 1$ TeV. Although the contact term increases the cross section at low χ, here the two curves have been normalized over the range in χ shown in order to show differences in shape.

CHAPTER 3

The DØ Detector

The DØ detector [13, 14] was designed as a multipurpose collider physics detector. It consists of three main components: the central detector, the muon system and the calorimeter as shown in Figure 3.16. Since jets are detected and measured in the calorimeter, it will receive special emphasis in the following descriptions. A discussion of jet triggering at DØ is also included.

At the Fermilab Tevatron, the distribution of the interaction points can be described by a Gaussian in the coordinate z, defined as the distance along the beam line where $z = 0$ is the center of the detector. During the run during which the data presented here was collected the center of the Gaussian was shifted 11 cm from the detector center and the width was 31 cm. When a pseudorapidity, η, is mentioned in the following descriptions, it is assumed the interaction occurs at $z = 0$. This will also be referred to as the "detector η" or "η index" and should be considered as a label for a given readout channel rather than a true pseudorapidity. The other coordinates used are the polar angle θ and the azimuthal angle ϕ.

3.1 Central Detector

The central detector resides in a barrel-shaped region surrounding the interaction point[15] (Figure 3.17.) It consists of three types of drift chambers and the transition radiation detector. Drift chambers consist of wires at high potential in a gaseous medium. They operate by timing the arrival of charge on the wires due to a high energy charged particle ionizing the gas. This time can then be used to form a "hit" coordinate in the chamber and a series of such hits can be linked together to form a "track", the reconstructed trajectory of the particle. Unlike

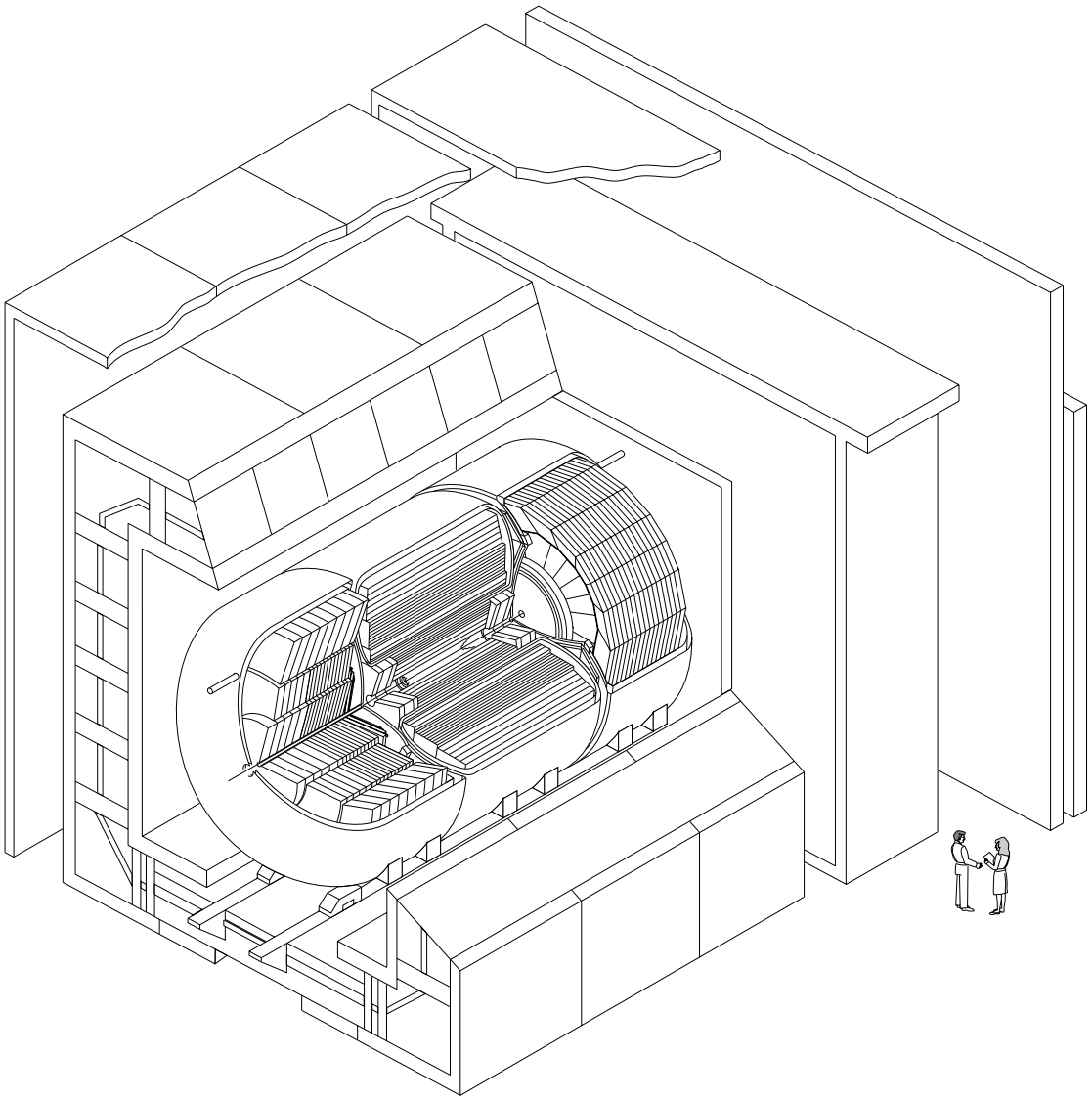

DØ Detector

Figure 3.16: The DØ detector.

some other collider detectors, DØ has no central magnetic field, so that particle tracks are straight and the momentum and sign of the charged particles cannot be determined. The four subdetectors are:

- Vertex Chamber (VTX): This subdetector consists of three concentric layers of drift chambers close to the beam pipe. It is used to measure the longitudinal position of the interaction point which in turn is used to correct the jet η and E_T.

- Transition Radiation Detector (TRD): The TRD is used to discriminate electrons from charged pions by measuring the radiation produced when crossing the boundary between materials with different dielectric constants. It consists of many layers of alternating dielectric and a proportional wire chamber to detect the induced radiation.

- Central Drift Chamber (CDC): The CDC consists of four layers of drift chambers just inside the central calorimeter cryostat. This subdetector, along with the two previously mentioned, measure tracks in the range of pseudorapidity $|\eta| < 1$.

- Forward Drift Chamber (FDC): The FDC's each include two types of chambers. The ϕ-chambers have radial sense wires and the θ- chambers have 4 quadrants with the sense wires perpendicular to and surrounding the beam.

3.2 Muon System

The wide angle muon system (WAMUS) consists of three layers of proportional drift tubes and a steel toroid. The first layer is inside the magnet and together with the central detector give the muon trajectory before the track is bent by the magnetic field. The two layers outside the steel measure the altered direction. In addition, the small angle muon system (SAMUS) end toroids and chambers give

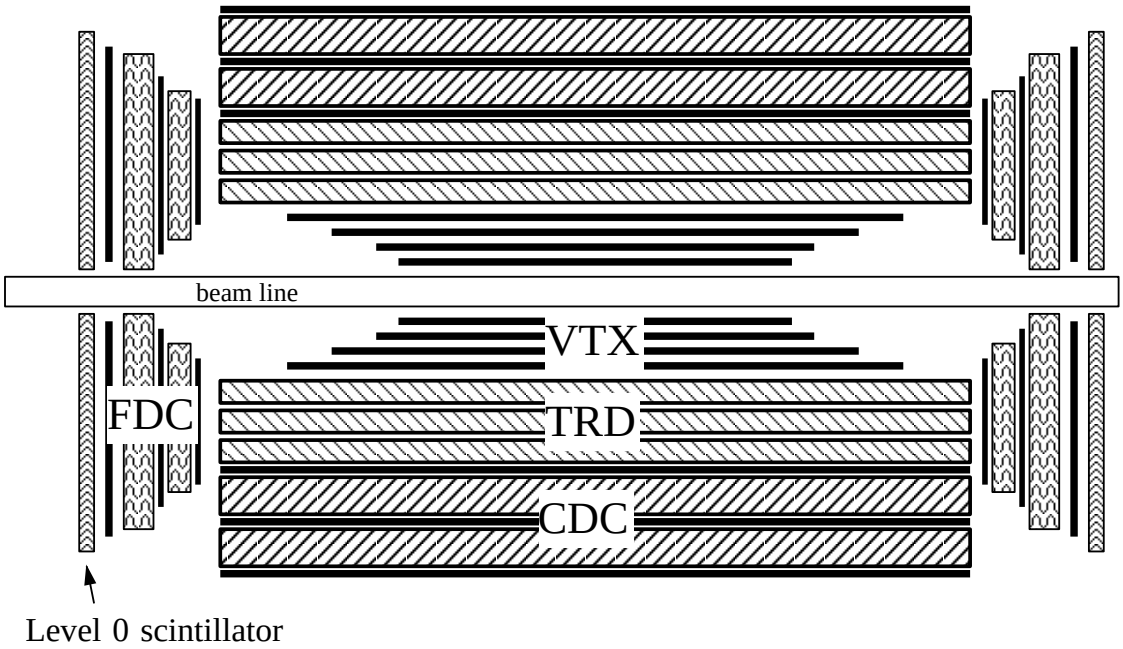

Figure 3.17: The DØ central tracking system.

coverage for $|\eta| < 3$. There are from 13-19 absorbtion lengths before the outer two muon chambers so the probability of pion punch-through is very small.

3.3 Calorimeter

Jets at DØ are measured exclusively in the calorimeter. This detector is a sampling calorimeter with depleted uranium as an absorber and liquified argon as the active ionizing material. As particles enter the calorimeter, they interact with the dense uranium and more particles are created. These particles also interact to generate more particles and this "shower" of particles passes from absorber plate to sampling layer to absorber plate again as they travel away from the interaction vertex. When charged particles traverse the sampling layer of liquid argon, they ionize the argon atoms. As shown in Figure 3.18, there exists a read-out board in the center of each argon gap where the copper pads and the absorber plates are held at ground

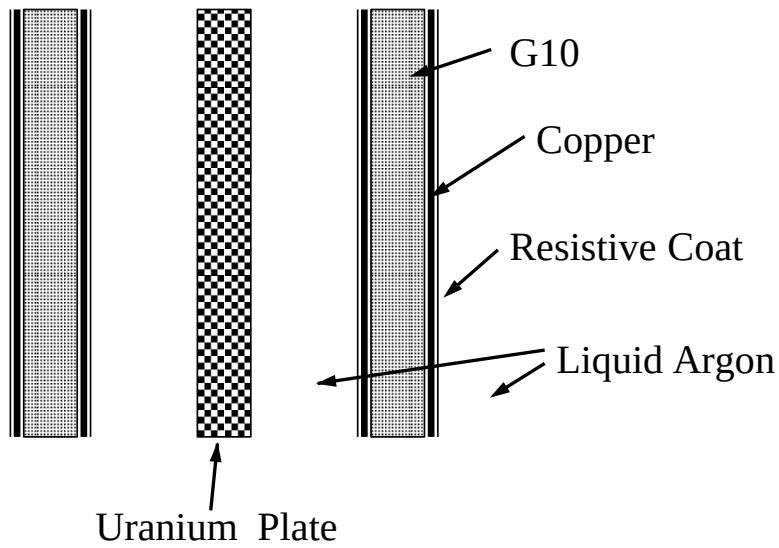

Figure 3.18: Cross-section through calorimeter readout sampling cell.

while the resistive coat is at high voltage (typically 2.0 kV.) The thin G-10 board between the resistive coat and the copper pads serves as a blocking capacitor for the preamp. As the charge moves across the argon gap, each copper readout pad produces a signal which is then sent through a charge-sensitive preamp, a shaping and sampling circuit known as the base line subtracter (BLS), and next to an analog-to-digital converter (ADC). The ADC's also subtract the pedestal value and zero-suppress each channel [16].

Typical transverse segmentation is 0.1×0.1 in η, ϕ where all longitudinal layers with the same η, ϕ index are projective from the center of the detector which is the nominal interaction point [1].

Physically, the DØ calorimeter is divided into 3 sections, the central (CC) and two end caps (EC) calorimeters (see Figure 3.19) each in its own cryostat in order to keep the liquid argon cold. In terms of function, it can be divided

[1] Actually, the calorimeter geometry is usually described as "pseudo-projective" since in the interest of cost, not every read-out board pad layout is customized for its particular depth in the calorimeter. The boards were produced typically in groups of 5, giving a somewhat "blocky" tower border.

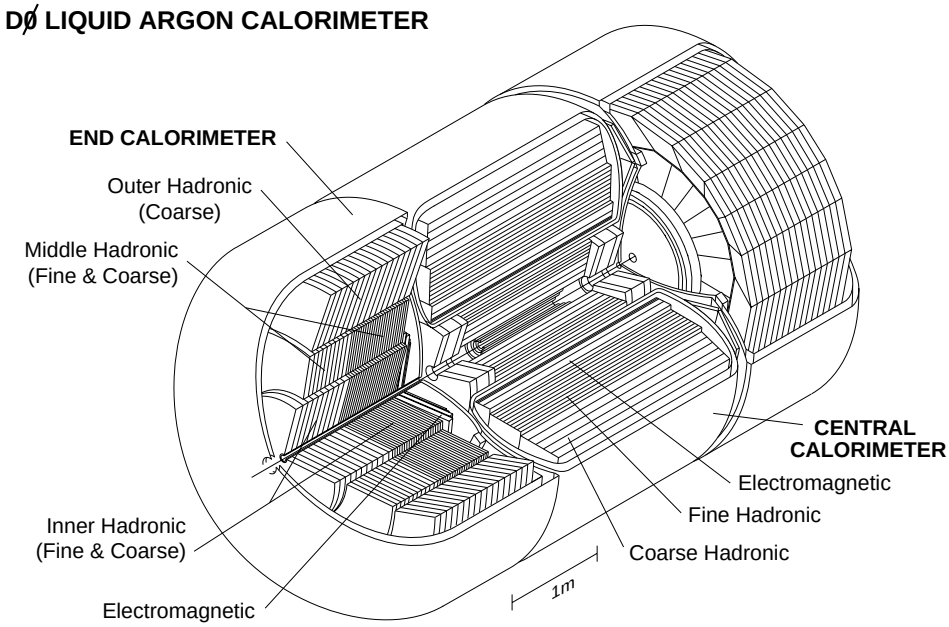

Figure 3.19: Cutout view of the DØ calorimeter.

into 3 different types in order from the interaction point outwards: First is the finely segmented electromagnetic section which absorbs almost all of the energy from electromagnetic showers. Next is the fine hadronic with thicker absorber and coarser sampling. Last is the coarse hadronic section with very thick absorber plates and very coarse sampling. Each of these calorimeter types will be discussed here in order.

- Electromagnetic Section (EM): The electromagnetic calorimeter uses uranium plates with thickness 4 mm in the EC and 3 mm in the CC for fine sampling and good energy resolution. It is read out in four longitudinal layers of thickness 2, 2, 7, and 10 radiation lengths (X_0), where the first layer thickness includes the cryostat wall. The transverse segmentation is $\Delta\eta \times \Delta\phi = 0.1 \times 0.1$, except for the third longitudinal layer where it is $\Delta\eta \times \Delta\phi = 0.05 \times 0.05$. This provides better positional resolution for electrons and photons since the average electromagnetic shower deposits about

65% of its energy in the third layer.

- Fine Hadronic Section (FH): The fine hadronic section uses 6 mm uranium plates and consists of four read-out layers in the EC and three in the CC. It is a total of about 5 interaction lengths in depth and has a transverse segmentation of $\Delta\eta \times \Delta\phi = 0.1 \times 0.1$.

- Coarse Hadronic Section (CH): The coarse hadronic section consists of very thick (46.5 mm) plates of stainless steel in the EC and copper in the CC that amounts to about 4 interaction lengths. This maximizes the containment of the shower in the calorimeter and prevents (except for the most energetic jets) the spraying of particles into the muon chambers.

The calorimeter modules were studied during test beam runs taken between 1985 and 1992 where various sections of the calorimeter were exposed to monochromatic beams of electrons or charged pions. The test beam results show that the calorimeter response is linear to within 0.5% for electrons above 10 GeV and pions above 20 GeV. The effects of nonlinear response for low energy particles is very important for jets, which are typically composed of many low energy particles. The low energy test beam data and its implications to jet energy response will be studied in great detail in chapter 5.

3.3.1 Massless Gaps and Inner Cryostat Detectors

Between calorimeter cryostats there exists a region of non-uniform response. A jet entering this region may encounter very little EM and FH calorimetry and deposit large portions of its energy in uninstrumented materials such as cryostat walls (2.5 cm thick steel) and support structures. For this reason, two separate and complimentary methods are used in this region in order to recover some of this lost information. The massless gap detectors consist of alternating sets of high voltage and grounded signal boards placed on the steel endplates of modules both in the CC and EC. They are sensitive to showering in the argon between the cryostat walls

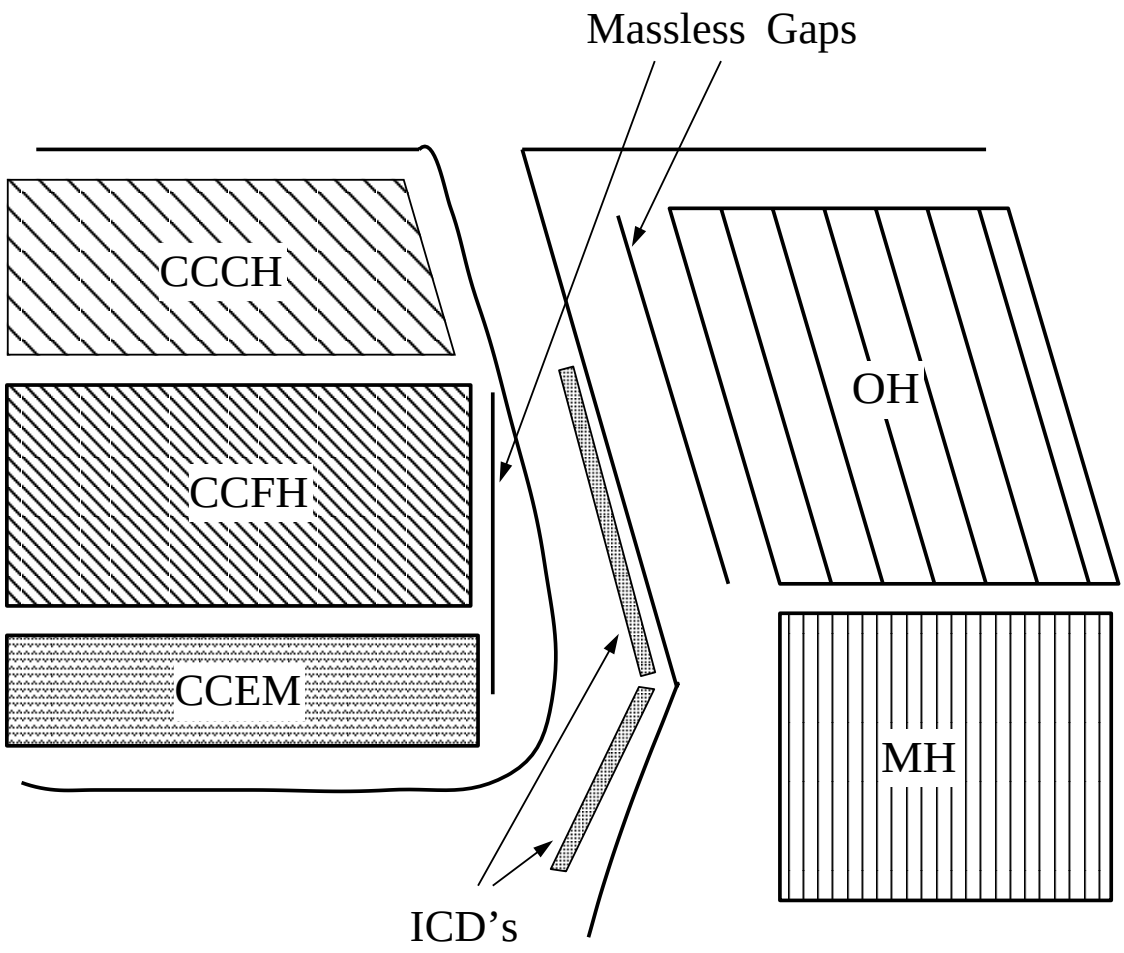

Figure 3.20: Cutout view of the calorimeter crack region.

and the steel endplates. The inner cryostat detector (ICD) consists of scintillator placed between the CC cryostat and the EC cryostats. The arrangement of these detector elements can be seen in Figure 3.20. They have been calibrated in a test beam setup and can contribute large fractions to the reconstructed energy of jets that enter the crack between cryostats.

3.4 Trigger System

At a typical running luminosity of $5 \times 10^{30}\text{cm}^{-2}\text{sec}^{-1}$, inelastic scattering events occur 200,000 times per second. Since events are written to tape at a rate of only 2 per second, the trigger system must quickly decide which events are worth keeping and which are not. This is accomplished using three trigger layers, each more restrictive than the previous:

- Level 0: The level 0 trigger system consists of a set of scintillators on each side of the interaction region[17]. By comparing the time at which particles passed through each side, these detectors are used to signal whether an interaction occurred, find its approximate position along the beam line, and also flag events with more than one interaction.

- Level 1: This trigger level accepts or rejects events on the basis of localized energy (actually E_T) deposits in the calorimeter[18]. It makes a decision by counting how many "trigger towers" were found above a certain E_T threshold. A trigger tower is formed by the summation of calorimeter cells (excluding the coarse hadronic, ICD and massless gaps) in a square of $.2 \times .2$ in $\eta - \phi$ space using special fast readouts on the BLS cards. These triggers can be prescaled by a number N, where only one event in N is passed on to the next layer. The level 1 trigger covers the range of pseudorapidity $|\eta| < 3.2$.

- Level 2: The level 2 trigger layer performs an event reconstruction similar to that used offline. This is performed on one of 50 Vaxstation 4000 model 60 computers, making this a software trigger as opposed to the first two trigger layers, where all decisions were made in hardware. Jet events are filtered at this stage by requiring at least one jet above a certain E_T threshold. Jets are constructed using the list of fired (above threshold) level 1 trigger towers as centers of the jet cone and without iterations. See §4.1 for a complete discussion of the offline jet reconstruction.

CHAPTER 4

The Jet Reconstruction Algorithm

For this analysis, jets are reconstructed using a cone algorithm[19]. Calorimeter energy clusters are found using an η, ϕ cone with radius 0.7. In this chapter, the algorithm will be discussed in detail and its ability to reproduce theoretical results will be studied.

Before the algorithm is presented, it is necessary to describe the processing of the data before it is used by the algorithm. The data for each event is zero-suppressed in hardware, that is, each cell with energy below some threshold is set to zero and not read out. The threshold used is 2σ, where σ is the width of the pedestal distribution, typically 10 MeV for a electromagnetic calorimeter cell and 50 MeV for an hadronic cell. Since the noise has negative as well as positive energy tails, the decision was made to use a two-sided zero-suppression, i.e., to zero channels when $|\text{Cell Energy}| < 2\sigma$. The zero-suppression has a negligible effect on the reconstruction but is important in energy scale considerations.

In the first step of the reconstruction, calorimeter cells with the same η and ϕ detector index are summed into towers. The energy centroid of each cell is corrected using the actual z-vertex, as obtained by central tracking, to obtain the cell's energy vector. The mass of each cell is taken as zero, so $\vec{P_{cell}} = \vec{E_{cell}}$. The cells in a given calorimeter tower are then summed vectorially to obtain E_x, E_y, E_z, and E_{total}. After the summation a true physics η, ϕ, and E_T for each tower is calculated using $\vec{E}$ and used for all subsequent steps of the jet finding.

4.1 Cone Algorithm

As a first step of implementing the cone algorithm, localized energy deposits are found and labeled "preclusters." The η, ϕ coordinates of these preclusters are used as initial centers for the iterative cone algorithm, which will try to find a stable centroid for the jet. If the final, stable jet cone then overlaps with any previously found jet cones, a decision must be made whether to split the overlap energy between the two jets or merge the two into one jet. The three steps are described in detail as follows:

- **Preclustering:** The preclustering algorithm loops over all towers. A precluster is formed for each tower with $E_T > 1$ GeV and the nearest neighbors are then added to the precluster if they also have $E_T > 1$ GeV. The E_T-weighted η, ϕ center of each precluster is calculated and kept in a list.

- **Jet Cone Implementation:** The input to the algorithm consists of the list of preclusters and the towers obtained as described above. The algorithm loops through the list of preclusters using the coordinate of each precluster as a "seed", or initial starting center, of the jet cone. Given the center of the cone, (call it η_0, ϕ_0), all the towers having an η, ϕ within the radius $R = 0.7$ are summed. That is, all towers with

  $$\sqrt{(\eta_0 - \eta)^2 + (\phi_0 - \phi)^2} < 0.7$$

  are summed. The four quantities E_{total}, E_x, E_y, and E_z are summed individually. A η, ϕ centroid is obtained from this sum in the following manner:

  $$\phi = \tan^{-1} \frac{E_x}{E_y} \qquad \theta = \tan^{-1} \frac{E_T}{E_z} \qquad \eta = \ln \cot \frac{\theta}{2}$$

  where $E_T = \sqrt{E_x^2 + E_y^2}$. The jet mass obtained from this procedure $M_J^2 = E_{total}^2 - \vec{E}^2$ is what you would get if each calorimeter cell were a massless particle. This is poorly measured and in the next section we will discuss how it is avoided altogether.

If the new centroid is the same as the initial centroid then it is considered stable and we are done with this stage. Otherwise, if the new centroid is different from the old, we must re-sum the towers using the new centroid as the center of the cone. In this way iterations are carried out to ensure that our jet centroid is the actual center of the calorimeter energy cluster. The stable jet centroid is then cut on E_T by requiring a minimum of 8 GeV in the jet. It is important to note that this iteration procedure can be thought of as a first pass of jet merging. If two energy clusters are close enough together, the iterations will bring the jet center to some point between the two clusters, and they will both be inside the jet cone.

- **Splitting and Merging:** If the newly found jet cone does not overlap any previously found jet cone, then we move on to the next precluster seed. Otherwise, if there is overlap, then we must decide whether to split the two jets or merge them into one. This decision is based on the fraction of E_T contained in the region of overlapping cones between the two jets. If the jet E_T's are labeled E_{T_1} and E_{T_2}, then they are merged if

$$\frac{\text{shared } E_T}{\min(E_{T_1}, E_{T_2})} > 0.5.$$

That is, if the jets share more than 50% of their E_T, then they are merged. Otherwise they are split and the shared energy is divided between the two by awarding individual towers to the jet with the nearest centroid. In either case, the jet parameters are recalculated based on the new set of towers in each jet.

Often two or more different initial seeds will lead, after iteration, to the same or very nearly the same jet centroid. If the new jet is within 0.01 in η, ϕ-space of a previously found jet and their E_T difference is less than 10 MeV then they are considered to be the same object and the new jet is not merged but simply erased.

4.1.1 Dijet Mass Measurement

As discussed above, by constructing sums of E_{total}, E_x, E_y, and E_z individually, we obtain an individual jet mass $M_J^2 = E_{total}^2 - \vec{E}^2$ that is determined as if each calorimeter cell were a massless particle. Jets actually do have a mass, obtained through the process of parton showering and fragmentation. The measured quantity is a poor measurement of the actual jet mass, since it is sensitive to η-dependent calorimeter segmentation and particle showering spread in the calorimeter as well as the actual jet width.

We need not measure the individual jet mass in order to calculate the dijet (equals di-parton) mass. The jet energy we measure is an accurate reflection, on average, of the parton energy[20], so we may set the individual jet mass to zero and redefine E_x, E_y, and E_z using E_{total}, θ, and ϕ. Now our definition of dijet mass requires only that we measure the jet energy and position well, and not the spread of individual particles. This is only approximate for the higher order QCD processes where two final state partons are close enough to be a single jet with mass, but studies indicate this effect is much smaller than the known calorimeter energy resolution contribution to the dijet mass uncertainty.

4.2 Jet Reconstruction Tests

We will be concerned here with how well the jet reconstruction algorithm performs in yielding the correct jet η and ϕ. Also of interest is how well the splitting and merging criteria used in the reconstruction match the theoretical criteria described in Chapter 2. The question of jet reconstruction efficiency will be covered briefly.

A detector Monte Carlo was used for the following tests. At DØ this includes a detailed simulation of the calorimeter geometry in the GEANT[21] physics program. GEANT simulates the interactions and showering of particles inside the calorimeter in order to provide some approximation of what actually happens in the DØ calorimeter. Although the GEANT simulation of DØ does not reproduce

the single particle energy responses seen at the test beam, it does give reasonably accurate transverse shower profiles which is all that is required here[22].

Simulated events used here are produced using the ISAJET [23] event generator. It is used to generate two jet events and includes leading-log parton showering and a fragmentation model. The output of ISAJET is a list of particle types and momenta which can be fed directly into GEANT. The particles from ISAJET are also formed into jets directly using a package called PJETS [24]. PJETS mimics the real jet reconstruction except that it uses particle energies rather than calorimeter tower energies. The jet from PJETS will also be referred to as the generated jet and the GEANT calorimeter jet as the reconstructed jet. Comparisons between the PJETS particle jets and the reconstructed jets will then show the degradation of the jet signal (including η and ϕ position) that arises in the calorimeter.

4.2.1 Jet Reconstruction Efficiency

Although the jet may form an energy cluster in the calorimeter, the reconstruction algorithm may not find it, for whatever reason: fluctuations near the E_T threshold, too broad, no precluster found, etc. This reconstruction efficiency can be found using the Monte Carlo GEANT and the particle jet finder, PJETS. A comparison is made between PJETS with the E_T threshold set at 3 GeV and reconstructed GEANT-simulated jets with the normal threshold of 8 GeV. Preclustering efficiency is not a concern with PJETS since it uses every particle as a jet seed in order from highest to lowest in E_T. The PJET is considered reconstructed if a reconstructed jet is found within a radius 0.7 in η, ϕ space where both use a cone size of 0.7. The results are shown in Figure 4.21 for jets above 3 GeV E_T. The PJETS reconstruction defined above is estimated to be fully efficient at 6 GeV E_T. The calorimeter jet reconstruction is seen to reach 99% efficiency at 16 GeV. In the analysis to come, no jets are used with reconstructed E_T below 20 GeV, so the reconstruction efficiency is taken always to be 100%.

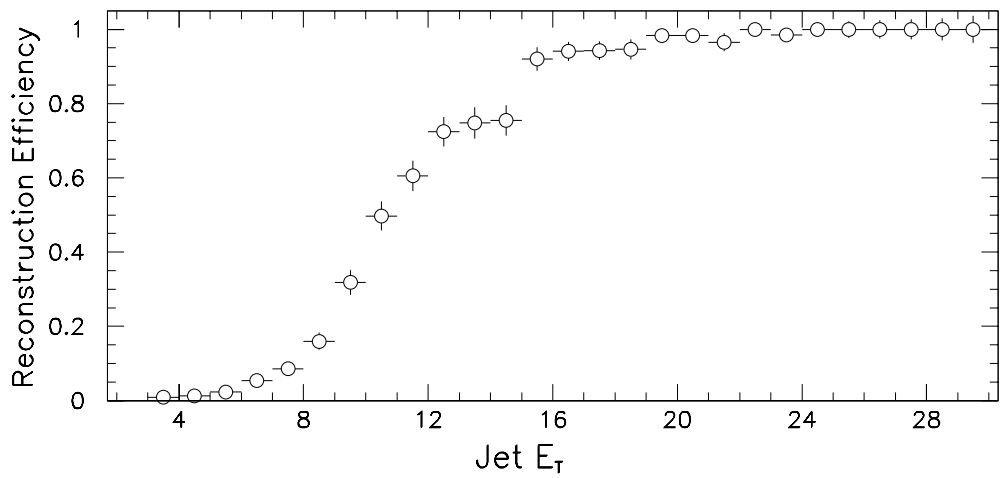

Figure 4.21: Jet reconstruction efficiency. The algorithm is seen to be nearly 100% efficient for jets with $E_T > 20$ GeV.

4.2.2 Uncertainty in Reconstructed Jet Position

The detector position resolution can also be studied using the Monte Carlo. ISAJET is used to generate two parton final states which are then parton showered and hadronized. The η and ϕ of the two outgoing partons from the hard scatter are considered to be the actual jet position and compared to the results of the jet reconstruction on the GEANT output. The reconstructed jet nearest the parton is used in the comparison but must be within $R = 0.5$ of the parton. The ϕ and η resolution results are shown versus jet E_T in Figure 4.22 for jets with $|\eta| < 1.0$. The resolution is seen to go to about 0.015 at high E_T in both η and ϕ. The difference between the η and ϕ resolution at low E_T may be due in part to the additional η position smearing from the measured z-vertex position smearing which was also simulated in the Monte Carlo.

The resolution in ϕ can also be tested, although somewhat imperfectly, using actual DØ two jet events. By requiring two and only two reconstructed jets

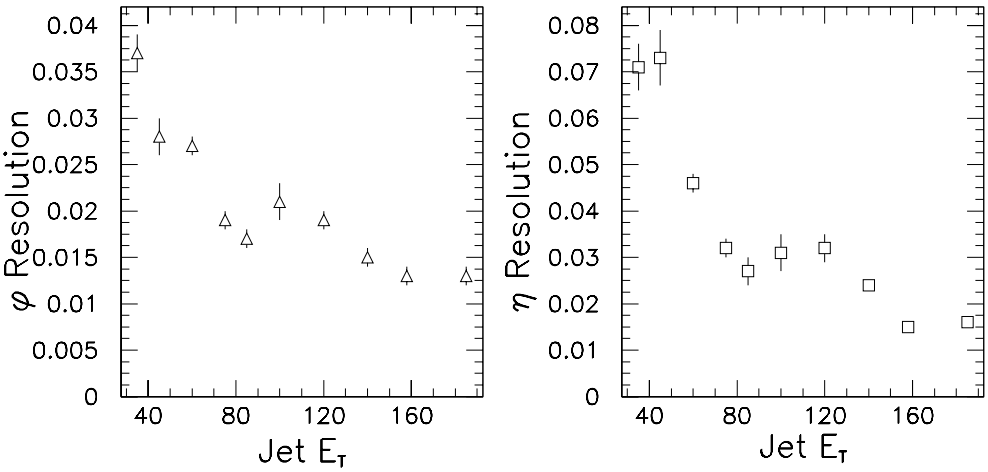

Figure 4.22: Resolution in ϕ and η versus jet E_T using the Monte Carlo simulation.

with $|\eta| < 1.0$ in the event we get a sample of jets that should be back-to-back in ϕ. The deviations from $\Delta\phi = \pi - (\phi_1 - \phi_2) = 0$ come from two sources:

- Smearing due to the finite ϕ resolution of the calorimeter. This is the only contribution to the Monte Carlo ϕ resolution obtained above.
- Fluctuations due to unreconstructed low-E_T jets at large angles from the two highest E_T jets. This contamination should be substantial for the lower E_T dijets and decrease as the dijet E_T increases.

Assuming the ϕ uncertainty is the same for each jet, then

$$\sigma_{\Delta\phi} = \sqrt{\sigma_\phi^2 + \sigma_\phi^2} = \sqrt{2}\sigma_\phi$$

or $\sigma_\phi = \sigma_{\Delta\phi}/\sqrt{2}$. So the ϕ resolution is simply the width of the $\Delta\phi$ distribution divided by $\sqrt{2}$. The resolution is shown in Figure 4.23 versus jet E_T and is seen to be larger than that obtained from the Monte Carlo, as expected.

Systematic shifts of the reconstructed η and ϕ of the jet can be determined using the Monte Carlo. Figure 4.24 shows the average value of $\Delta\phi$ and $\Delta\eta$ versus

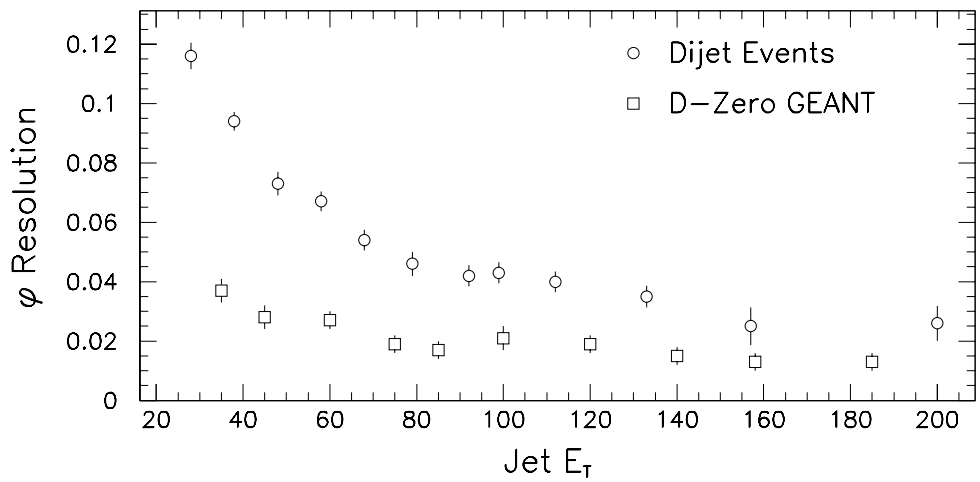

Figure 4.23: Resolution in ϕ using actual dijet events compared to ϕ resolution from Monte Carlo.

η. Small shifts in η away from the beam line are seen in the crack region, but since this region is physically complex and therefore hard to simulate, no corrections in eta position will be performed. An additional η position uncertainty will be introduced to account for these results.

4.2.3 Tests of Jet Splitting and Merging

The splitting and merging algorithm must be tested for compatibility, at the parton level, with the splitting and merging criteria used in the next-to-leading-order calculations of Ellis, Kunszt and Soper (EKS.) This test has been conducted[25] using generated events with only two partons that were within $R = 1.1$ of each other with the requirement that the events satisfy the EKS definition (See Chapter 2) of two jets using a cone size of 0.3. Additionally, the partons were required to have $|\eta| < .5$, total E_T between 75 and 140 GeV, and minimum E_T of 15 GeV. The two parton events were simulated in the detector using GEANT, and the jet reconstruction using a cone size of $R = 0.7$ was performed. Figure 4.25 shows the

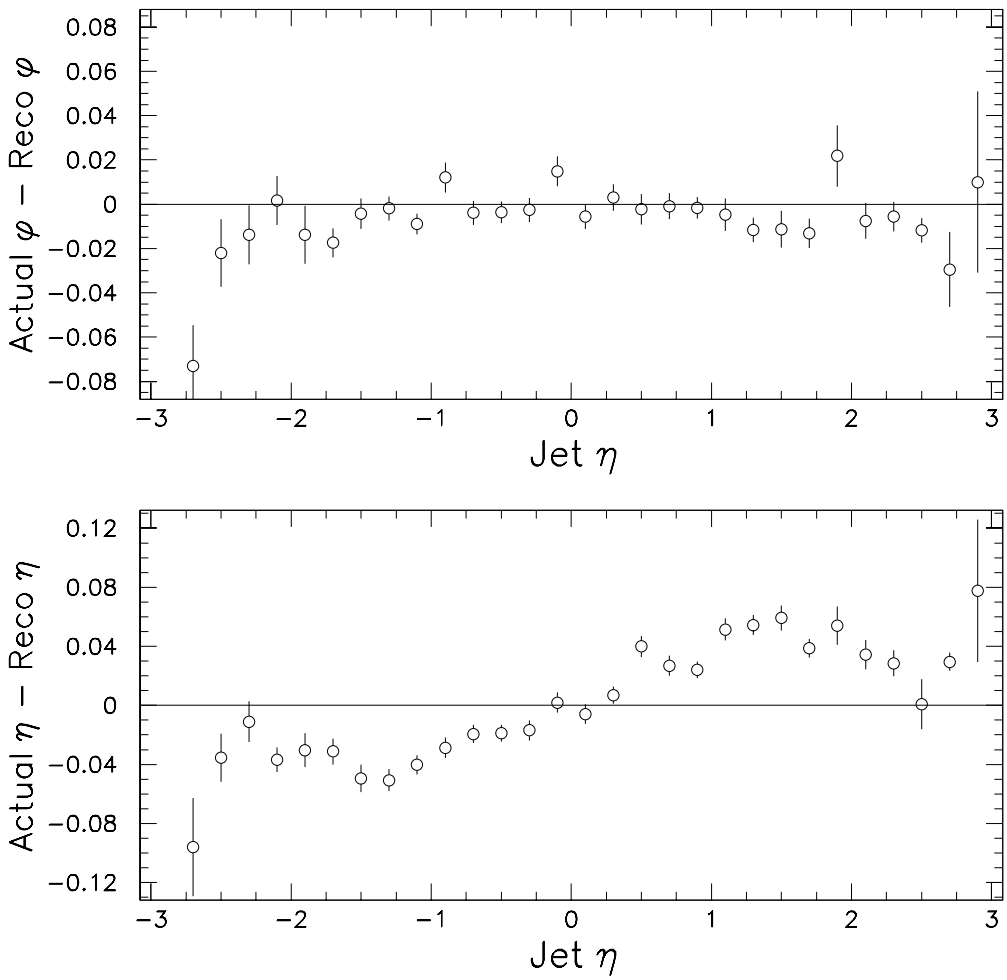

Figure 4.24: Systematic shifts in reconstructed ϕ and η versus jet η using the Monte Carlo simulation. An η dependent bias is seen.

results of the comparison using the variable (Number of EKS jets) - (Number of reconstructed jets) for a splitting fraction of 0.5 and a cone size $R = 0.7$. A value of zero indicates agreement and as can be seen from the Figure, the two methods agree about 85% of the time. This is encouraging, since the sample we have tested should optimize the disagreement between the two methods.

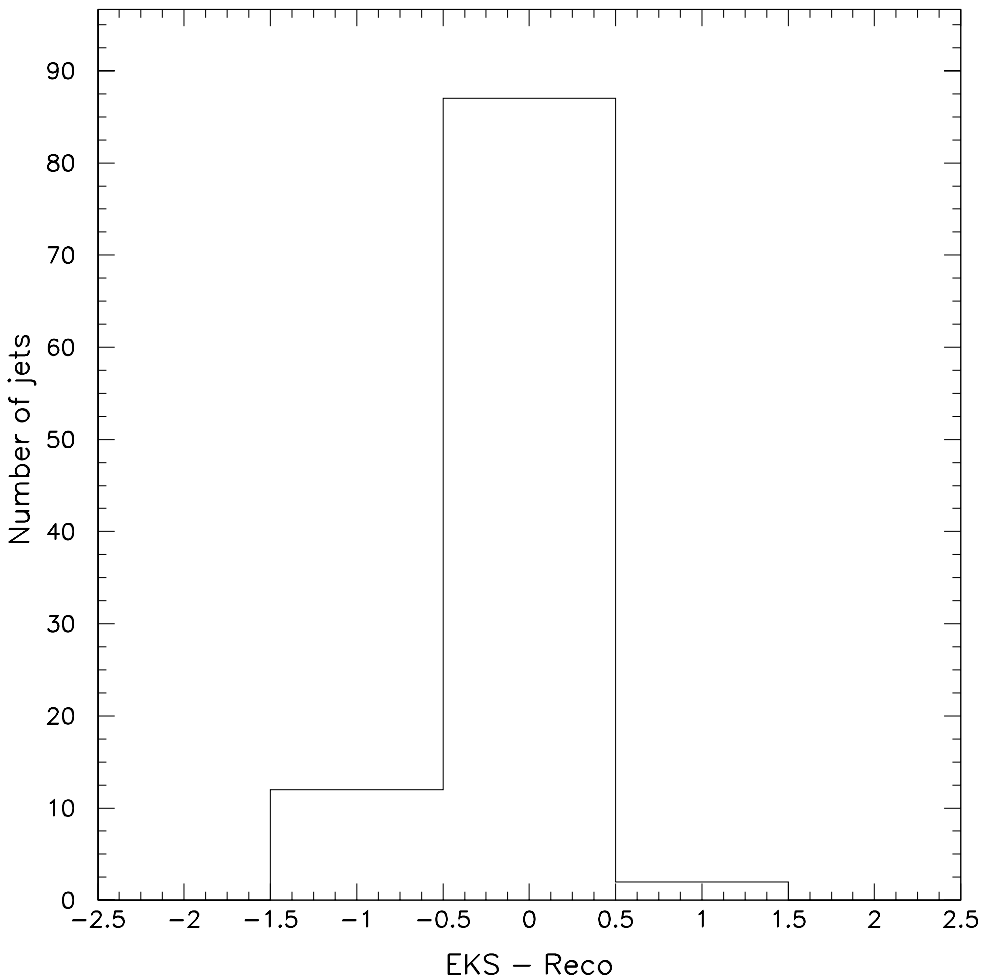

Figure 4.25: Number of jets found with EKS algorithm minus number of jets found with reconstruction algorithm when the splitting fraction equals 0.5.

CHAPTER 5

Data Selection and Corrections

In this chapter we will discuss how the final event samples are obtained, both the online triggering that was used and the offline cuts that have been made. An explanation of the derivation of the jet energy scale correction will follow.

The data used in this analysis was taken during a 10-month period at the Fermilab Tevatron collider. A total of 8.277 pb^{-1} will be used in this analysis which was accumulated during the run with instantaneous luminosities ranging from about $0.5 \times 10^{30} cm^{-2} sec^{-1}$ to $8.7 \times 10^{30} cm^{-2} sec^{-1}$. Except for luminosity, the trigger conditions were quite stable. Some of the triggering parameters did change during the run, as mentioned below, but these changes were minor and did not necessitate separate analyses.

5.1 Jet Triggering

The DØ trigger system, which has been introduced in Chapter 3, is composed of 3 separate trigger levels. It can support up to 32 different combinations of level 0 and level 1 trigger requirements, and up to 64 combinations in level 2.

5.1.1 Description of Triggers

Since the jet E_T and dijet mass spectrum fall very rapidly as the energy increases, a trigger that was fully efficient for 30 GeV E_T jets would see very few 100 GeV E_T jets. For this reason, the jet data used in this analysis was taken using 5 different trigger combinations, each covering a different range in single jet E_T (with some overlap.) Table 5.2 gives each trigger by name, and running parameters of each. Also shown is the number of events accumulated from each trigger, and

Table 5.2: Triggers used to acquire dijet data. See text for explanation of terms.

Jet Triggers					
Name	Level 0	Level 1	Level 2	Events	Luminosity
JET_MIN	SL0, MB	JT(1,3)	L2JT(20)	321,000	8.166 nb^{-1}
JET_LOW	SL0, MB	JT(1,7)	L2JT(30)	395,000	94.08 nb^{-1}
JET_MEDIUM	SL0, MB	JT(2,7)	L2JT(50)	249,000	678.6 nb^{-1}
JET_HIGH	SL0*, MB	JT(3,7)	L2JT(85)	217,000	3.380 pb^{-1}
JET_MAX	–	JT(4,5)	L2JT(115)	186,000	8.277 pb^{-1}

* The slow z-vertex requirement was used for approximately half of the JET_HIGH events.

the corresponding effective luminosity. All of the triggers except JET_MAX were prescaled with a value dependent on the instantaneous luminosity.

- **Level 0:** The level 0 scintillator counters give a signal if evidence of proton-antiproton breakup is seen and it is in coincidence with a bunch crossing. This requirement is always made on jet triggers. The timing between the two counters (one on each side of the interaction region) can also give a measurement of the position of the interaction vertex along the beam line (z-axis.) This has been used for the jet triggers; in Table 5.2, SL0 indicates that the level 0 z-vertex was required to be within 10.5 cm of the nominal interaction point. This requirement was made for all triggers except JET_MAX and JET_HIGH, and was used on the JET_HIGH trigger until approximately halfway through the run. This requirement reduces the rate by about about a factor of 4, and since the triggers were prescaled anyway, limiting the z-vertex position to center gives us a sample of more accurately measured jets.

  All of the triggers except JET_MAX utilized micro-blanking (MB in Table 5.2.) The main ring accelerator component that runs through the outermost (coarse hadronic) section of the calorimeter (see §3.3) has protons

injected at about 4 second intervals when in operation[1]. For a short time after injection (350 μs) these protons can collide with the main ring beam pipe walls, thereby depositing large amounts of energy in the coarse hadronic section. Events with this problem can be almost completely avoided by simply vetoing any events which occur during this time period.

The trigger JET_MAX is used to collect the highest E_T (and highest mass) jet events and so has the fewest restrictions in order to collect as much as possible of these rare and interesting events. This trigger was never limited by prescales, level 0 z-vertex cuts or micro-blanking.

- **Level 1:** The calorimeter level 1 trigger operates by making a fast summation over all layers in a $.2 \times .2$ region in η, ϕ and testing to see if these "trigger towers" are over the requested threshold. In Table 5.2, the notation "JT(n, x)" means that the requirement for an event to pass level 1 is that n towers have E_T greater than x GeV. The number of trigger towers requested should not be confused with the number of jets, since very often a single jet will result in two or more trigger towers above the threshold.

- **Level 2:** The level 2 jet trigger operates by forming jets using the calorimeter cell information and requiring at least one above a threshold. In Table 5.2, L2JT(x) indicates that the level 2 requirement was at least one jet with E_T greater than x GeV. A cone size of $R = 0.7$ was used and the ICD and massless gap data was not available for the level 2 reconstruction. The z-vertex from level 0 was used to calculate the actual jet η and E_T.

  The level 2 jet reconstruction uses the list of above-threshold trigger towers from level 1 as centers of its jet cones. Since the reconstruction is constrained in the computer CPU time it can use, no iterations of the jet center and no splitting or merging of jets is done. Therefore it cannot find jets that did

[1]The main ring accelerates protons during the store for use in making antiprotons, which are accumulated in storage ring.

not trigger in level 1. In order to improve the level 2 efficiency, the 3 GeV level 1 threshold JT(1,3) was in operation for all triggers. Although this has no effect on the level 1 rates or efficiencies, it does make available all those trigger towers with more than 3 GeV E_T for level 2 jet finding.

The jet trigger is designed to pass events with at least one jet above a certain threshold, and each successive level sharpens this cut. In order to use the data from these triggers, however, we must know how well each trigger performed its task by determining the efficiency of each trigger and its dependence on jet E_T and η.

5.1.2 Jet Trigger Efficiencies

The trigger efficiencies are calculated using the data. The level 1 trigger tower and level 2 reconstructed jet information are stored in each event, so one can determine whether a given jet either caused or would have caused a trigger given the level 1 and level 2 thresholds. So, starting with events from a minimum bias trigger (only level 0 required) we test the jets to see if they would have triggered the JET_MIN trigger. Figure 5.26 shows the results of this test where the trigger efficiency is defined as the ratio of jets that would have caused a trigger with all the jets found at the given E_T and η. The JET_MIN trigger is seen to become efficient ($> 95\%$) for jets at 25 GeV E_T. Although not shown here, the trigger shows some η-dependency in the form of a dip in efficiency at about 1.4 is due to the fact that the ICD and massless gaps are not used in the trigger. The efficiency also drops above $|\eta| = 3.0$ is due the limit of the level 1 trigger instrumented area. The most forward rings of trigger towers cover the range from $3.0 < |\eta| < 3.2$.

Knowing the efficiency for the JET_MIN trigger, we can now use these events to calculate the efficiency of the JET_LOW trigger in a manner very similar to above. By testing jets to see whether they would have passed the JET_LOW trigger requirements and dividing the number that would have passed by the total

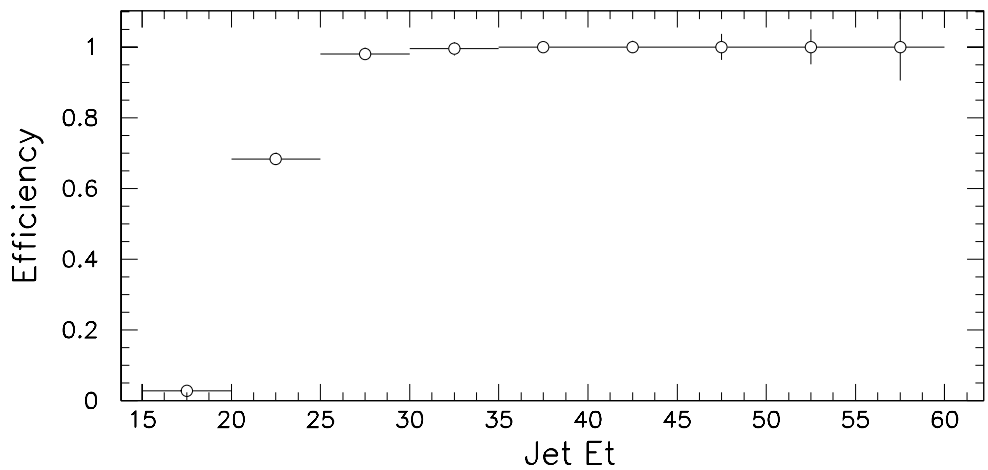

Figure 5.26: Trigger efficiency for JET_MIN trigger. Efficiency versus jet E_T for jets with $|\eta| < 0.7$.

number we obtain the efficiency versus jet E_T. The results for the JET_LOW trigger are shown in Figure 5.27.

In the same fashion, we obtain the efficiencies for the JET_MEDIUM trigger by studying events from JET_LOW, JET_HIGH from JET_MEDIUM and JET_MAX from JET_HIGH. The results are shown in Figures 5.28,5.29, and 5.30 for the JET_MEDIUM, JET_HIGH, and JET_MAX triggers, respectively. This information is summarized in Table 5.3 where the average efficiency at the benchmark E_T for $|\eta| < 3.0$ is shown. The benchmark E_T for each trigger is defined as the value for which the trigger is approximately 95% efficient and also a multiple of 5 GeV.

5.2 Event Selection

Not all events that pass a given trigger should be used in the analysis. Events which contain fake jets from a background source should be removed along with events with kinematical variables outside the region of interest. Also, we will remove

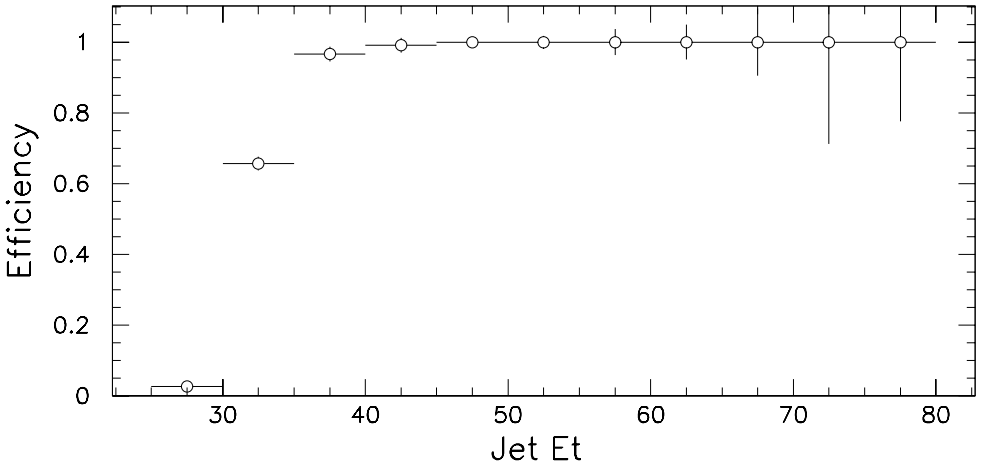

Figure 5.27: Trigger efficiency for JET_LOW trigger. Efficiency versus jet E_T for jets with $|\eta| < 0.7$.

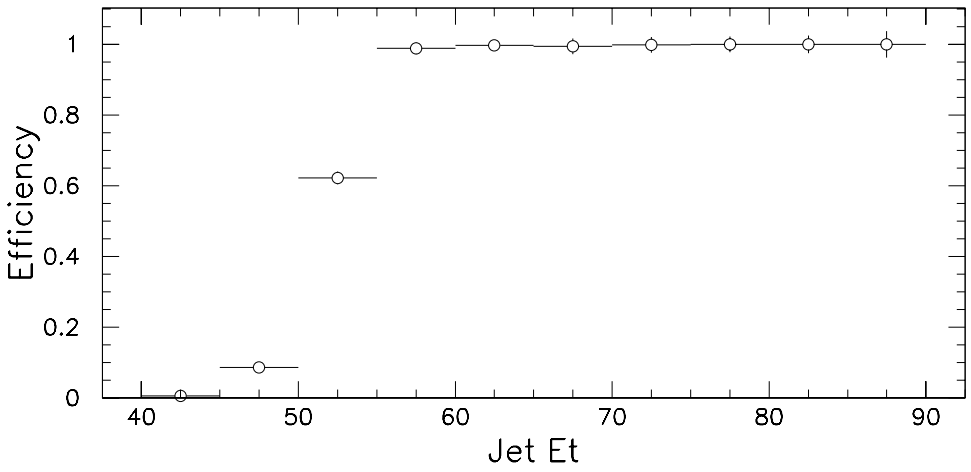

Figure 5.28: Trigger efficiency for JET_MEDIUM trigger. Efficiency versus jet E_T for jets with $|\eta| < 0.7$.

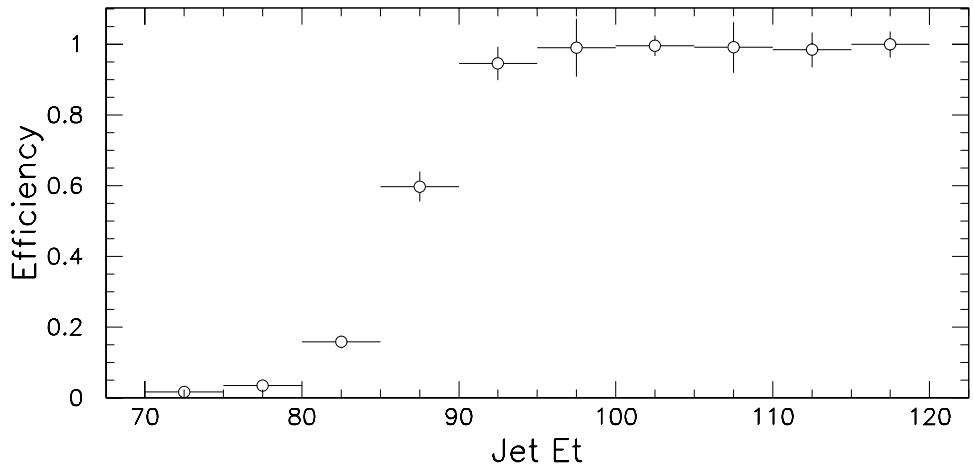

Figure 5.29: Trigger efficiency for JET_HIGH trigger. Efficiency versus jet E_T for jets with $|\eta| < 0.7$.

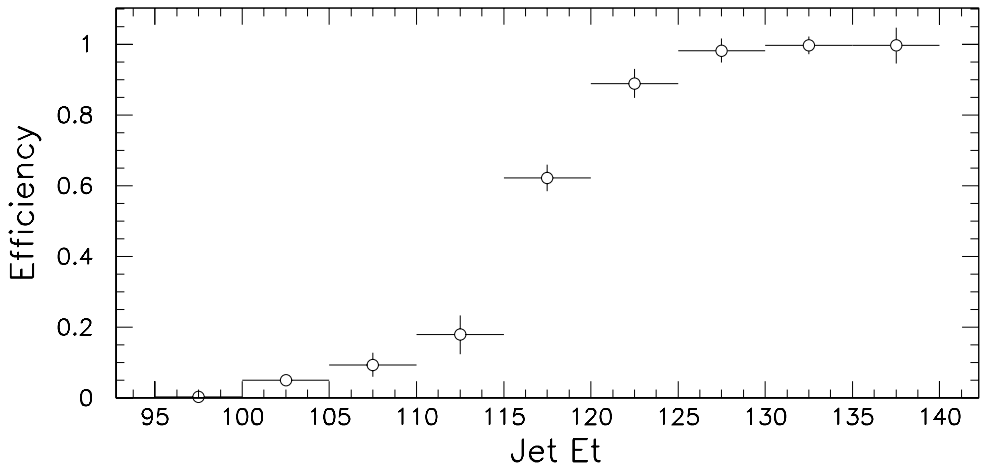

Figure 5.30: Trigger efficiency for JET_MAX trigger. Efficiency versus jet E_T for jets with $|\eta| < 0.7$.

Table 5.3: Trigger E_T thresholds and efficiencies.

Jet Triggers		
Name	Benchmark E_T	Average Efficiency
JET_MIN	25 GeV	98%
JET_LOW	35 GeV	97%
JET_MEDIUM	55 GeV	98%
JET_HIGH	90 GeV	94%
JET_MAX	125 GeV	97%

events for which the trigger is inefficient. Kinematical cuts will be discussed in the next chapter when acceptances are known.

5.2.1 Removal of Fake Jets

The trigger and offline jet reconstruction are susceptible to spurious energy deposition in the calorimeter from sources other than final state partons from an inelastic scatter. These sources include, but are not limited to, main ring energy deposition, cosmic ray bremmstrahlung, and noisy calorimeter cells. Cuts are made on jet energy deposition topology and tested using data with known problems for their efficiency at detecting the fake jets. Monte Carlo events are used to estimate how many real jets are removed by the cuts. The cuts used are described below:

- **.05 < EMfrac < .95:** The electromagnetic fraction (EMfrac) is defined as the fraction of the jet's E_T that was deposited in the electromagnetic portion of the calorimeter. It is constrained to be greater than .05 and less than .95. This cut is very effective against noisy calorimeter cells and has been seen to find over 90% of these fake jets. It rejects very few real jets as can be seen in Figure 5.31, which shows the fraction of Monte Carlo (noise-free) jets that are passed by this cut versus jet E_T and η. Since there is no electromagnetic calorimetry in the cryostat crack region, a slight dip in efficiency can be seen at around $|\eta| = 1.4$.

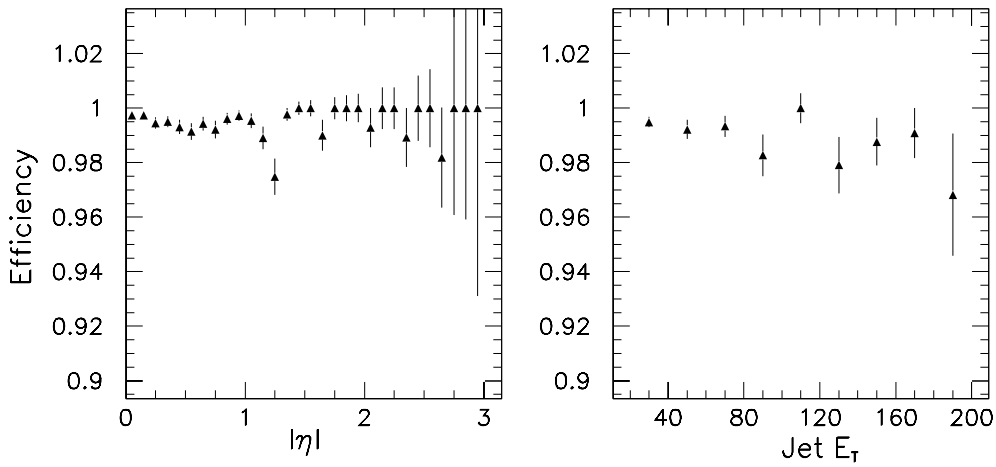

Figure 5.31: Efficiency of the cut $.05 <$ EMfrac $< .95$ (a) versus $|\eta|$ for jets with $E_T > 25$ GeV, and (b) versus E_T for $0.9 < |\eta| < 1.4$.

- **CHfrac $< .4$:** This cut is intended to remove fake jets caused by main ring deposits. Even with micro-blanking, particles under acceleration in the main ring still sometimes hit the beam pipe in the vicinity of DØ. The majority of the energy for such occurances will be in the coarse hadronic, so a cut requiring the fraction of E_T of the jet in the coarse hadronic calorimeter to be less than 0.4 removes most all ($> 95\%$) of fake jets from this source. This cut will also remove over 99% of fake jets due to noisy cells in the coarse hadronic calorimeter. Figure 5.32 shows the efficiency of this cut for Monte Carlo events and it is seen to be greater than 99% everywhere except in the cryostat crack region, where it drops to 95%. This is due to the higher probability that a jet will deposit the majority of its energy in the outer coarse hadronic due to the missing electromagnetic and fine hadronic calorimetry.

Since we need two good jets in the event, the event is rejected if either of the first two cuts fail for either of the two highest E_T jets in the event. Another cut that is not used on the final data sample but is used on the energy calibration

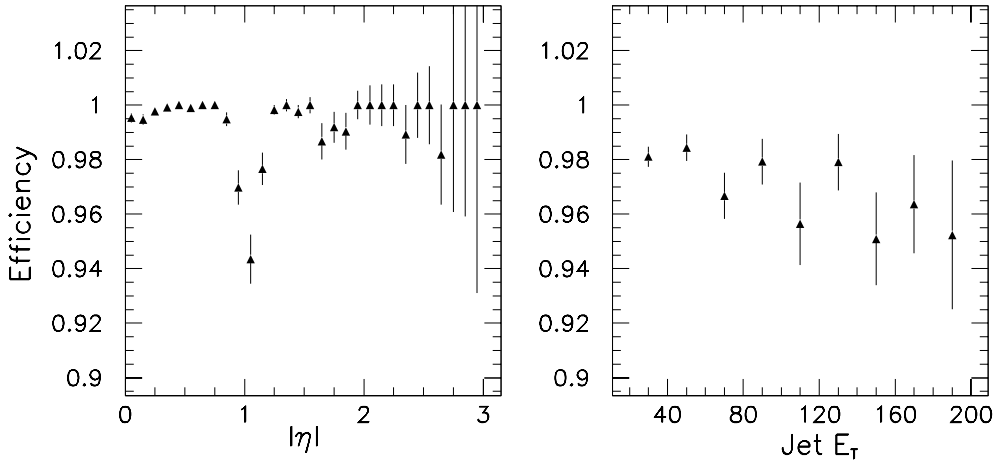

Figure 5.32: Efficiency of the cut CHfrac $< .4$ (a) versus $|\eta|$ for jets with $E_T > 25$ GeV, and (b) versus E_T for $0.9 < |\eta| < 1.4$.

data is the "cell ratio", defined as the ratio of the E_T of the highest E_T cell in the jet to the 2nd highest E_T cell in the jet. This cut is very efficient at removing jets due to noisy cells but also removes a sizable fraction of good jets.

5.2.2 Trigger Threshold Cuts

In order to keep biased events out of the data sample, a cut is made on the average uncorrected E_T of the two highest jets. It is required to be above the level 2 threshold of each trigger (see Table 5.2) where the efficiency is typically 70% or higher. This also has the effect of making the acceptance calculations more reliable by removing events where the trigger turn-on is steepest, and therefore not well determined.

5.3 Jet Energy Calibration

The jet energy scale is very important for almost every jet measurement and analysis made at DØ. Uncertainties in jet energy calibration are the largest source of

systematic error for this analysis.

Jet response in the calorimeter is based on many factors, the most important of which is the single particle energy response. Jets are often composed of many low energy ($E < 10$ GeV) particles and the calorimeter in general responds poorly to low energy particles. So while we may read out 50 GeV of energy for a 50 GeV incident pion or electron, we may only get 40 GeV from a 50 GeV jet.

Other effects which may contribute to a lowering of the calorimeter jet response include out-of-cone showering, defined here as the showering occurring inside the calorimeter which can deposit energy outside the jet cone although the incident particle itself is inside the jet cone. Also, calorimeter cells are zero-suppressed before being read out (see Chap. 4) which removes energy from the jet if many cells have small amounts of energy deposited in them. This is what happens for high energy jets. But for low energy jets zero-suppression actually increases the amount of energy seen since the pedestal distribution for a given cell is not symmetric and has a positive side tail due to background from the radioactive uranium. The average of the distribution (after pedestal subtraction) is by definition zero, but after zero-suppression the average energy is positive due to the tail of the distribution. This has the effect of adding a constant amount of energy to each jet.

The last effect to be considered is the underlying event energy due to the breakup of the proton and antiproton after the hard scattering takes place. This adds a constant E_T to a jet cone.

5.3.1 Jet Energy Scale in the Central Calorimeter

As the first step in calibrating for jets, we concentrate on jets well-contained in the central calorimeter. Here there is an abundance of low energy test beam data and most systematic effects are simpler; uncomplicated by non-uniform calorimetry and high-η jet shape considerations. The extension of the energy calibration from the central region to the rest of the calorimeter will be done using dijet P_T balance,

and is discussed in §5.3.2.

The calibration has been performed using two completely separate methods, one using data from test beam runs and the other using actual collider data. The jet energy scale from the actual data is the one used later to correct the jet energies, but the test beam method itself is a useful and informative process.

Jet Energy Scale from Test Beam Data

The method described here is an attempt to use the test beam data to obtain a jet energy response that one can use to correct collider data. The test beam single particle responses were used to simulate the calorimeter response to a jet. A jet was generated using a given event generator Monte Carlo (either Pythia, Herwig, or ISAJET) and each particle's energy was multiplied by the appropriate test beam response and summed. The sum of response-altered particle energies divided by the sum of unaltered particle energies is the jet energy response. Test beam particle showering information gives us the effect of out-of-cone showering and zero-suppression.

The test beam data used in this note is shown in Figures 5.33 and 5.34 and was taken during 1990-1991 run at Fermilab[26]. The response is defined as the fraction of the incoming particle's energy which is measured by the calorimeter. The data at and below 10 GeV was obtained from a special low-energy beamline setup. The responses shown are from the benchmark point of $\eta = 0.05$, $\phi = 31.6$.

The pion response drops a great deal at low energies, and this is the dominating effect when considering the jet energy scale. The shape of the jet energy scale depends mostly on the shape of the pion response curve and, to a lesser extent, the shape of the electron response curve (assuming a given jet fragmentation.) The electron response decreases at low energies due mainly to effects of upstream material, but low energy hadronic response is not well understood.

Since there is no test beam data below 2 GeV, a (somewhat arbitrary) choice was made to use the 2 GeV point for all particle energies below 2 GeV. In

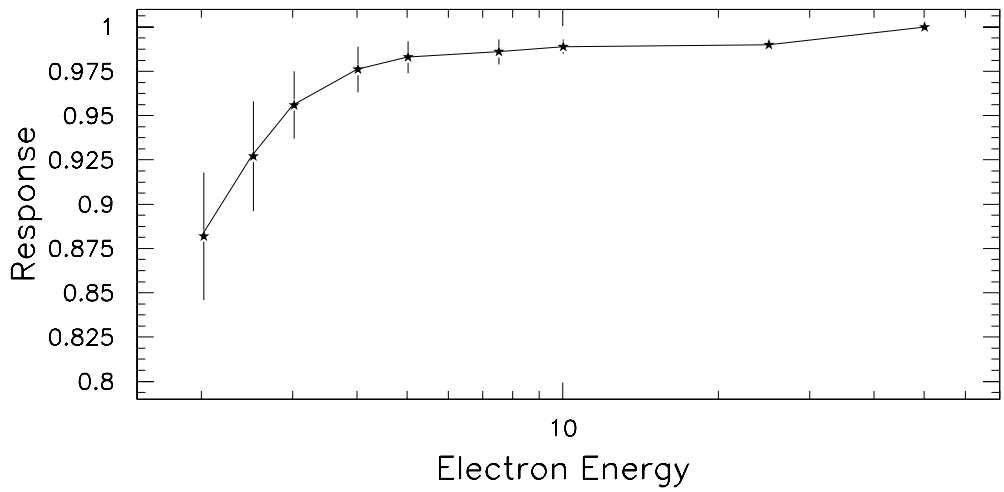

Figure 5.33: Test beam responses for electrons.

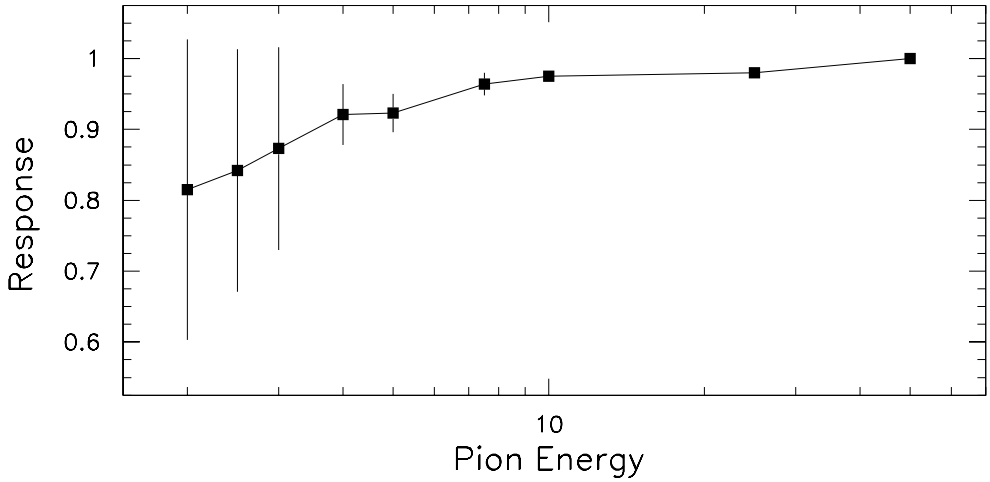

Figure 5.34: Test beam responses for pions.

effect, the response was chosen to be constant below 2 GeV. This was done for both pions and electrons and the ramifications of this choice will be explored later.

The detector response is not uniform in ϕ due to the segmentation into 32 CCEM modules and 16 CCFH modules. Since the test beam responses used here were taken at a value of ϕ away from these module/module cracks, a further correction must be applied in order to make the simulation more realistic. CCEM ϕ crack effects were simulated using data from 25 GeV electrons at $\eta = 0.025$ and scanning in ϕ. The data shows a drop in response of about 15% at the center of the crack (due to uninstrumented regions) and an increase near the edges of the crack (due to less absorber.) These effects average out when integrated over ϕ and the result is a negligible difference in jet response when the CCEM ϕ crack is included. Cracks also exist between CCFH modules and effect hadronic response adversely. Data from 25 GeV pions near the CCFH ϕ cracks shows a 10% drop in pion response at the center of these cracks. Using this data to simulate the effects of the cracks on hadronic response results in about a 1% decrease in the jet response. Pions in the test beam were seen to be insensitive to CCEM cracks and likewise electron response was independent of CCFH crack position. Both the CCEM and CCFH ϕ crack effects were included in the simulation.

The jet simulation was accomplished using the Pythia[27] event generator. Jets were defined using the particle PJET jet finder as described in §4.2. The jets were required to be free of overlap with other jets found in the same event in order to minimize algorithm dependent biases. Figure 5.35 shows the particle energy composition of an average 50 GeV jet where electromagnetic and hadronic contributions are shown separately. The Figure shows the importance of low energy responses; note that on average 67% of the total jet energy comes from particles with energies below 5 GeV.

To generate a jet energy scale the particles in the jet cone were multiplied by the test beam response according to particle type. Electrons and photons were multiplied by the response from electrons at the test beam. In order to make the

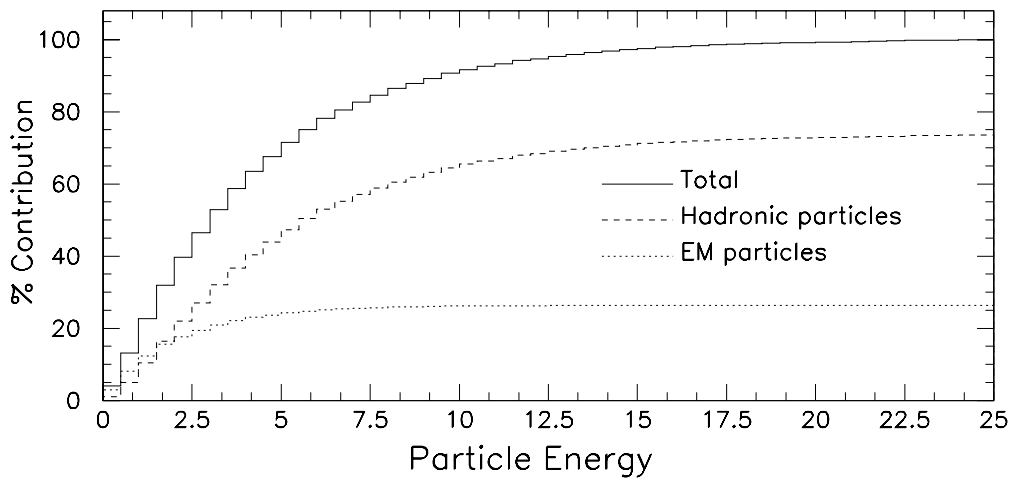

Figure 5.35: Particle composition of 50 GeV jets. The percent contribution is shown integrated over lower energies. For example, particles with energies below 5 GeV make up about 70% of the total jet energy.

simulation more accurate, π^o's were treated as if they decayed into two photons, each with half the energy of the original particle. All other particles were considered to be hadronic and were multiplied by the response from pions at the test beam. Since at the test beam the responses were measured at discrete values of particle energy, and the event generator gives a continuous spectrum of particle energies, the responses were calculated by interpolating between test beam data points. As mentioned above, below the lowest data point the response and error was taken to be constant equal to the response and error at 2 GeV for both pions and electrons. In order to incorporate ϕ cracks the distance of each electromagnetic particle to the nearest CCEM ϕ crack was calculated and the response corrected accordingly. The CCFH cracks are handled in a similar manner.

The nominal scale was generated using the nominal test beam response values. To get the upper limit on the uncertainty, the upper points of the error bars in Figures 5.33 and 5.34 were used as well as an additional 2% for electrons and 5% for pions to reflect the overall scale uncertainty that occurs when transferring

Table 5.4: Results of fitting $E_{measured}$ versus E_{actual}

$E_{measured} = A_0 + A_1 E_{actual} + A_2 E^2_{actual}$			
Fit Data	A_0	A_1	A_2
Nominal	-1.666	0.896	0.000239
High Response	-0.822	0.949	0.000142
Low Response	-2.177	0.843	0.000316

the test beam results to the D-Zero calorimeter. The lower limit was obtained in a similar way, by using the lower points on the error bars minus 2% for electrons and 5% for pions.

The simulated response curves were then fit to the following polynomial: $E_{measured} = A_0 + A_1 E_{actual} + A_2 E^2_{actual}$. The fits were made using the data from 25 GeV to 200 GeV and agree with the data curve to within .5%. The values of A_i are shown in Table 5.4 for the 3 fits. In Figure 5.36 we show $E_{measured}/E_{actual}$, the jet energy response in the calorimeter. The nominal curve ranges from 84% at 25 GeV to 93% at 200 GeV. The errors on the response are seen to range from 10% at 25 GeV to 4% at 200 GeV. Also note that the response is still somewhat less than 100% even for 200 GeV jets. This is due to the fact that low energy particles make up a substantial portion of the jet energy even for 200 GeV jets. The shape of the response curve is due to two main effects:

- The variation of the test beam results with particle energy (Figures 5.33 and 5.34.)

- The change in particle energy composition of jets with jet energy Figure 5.35 shows the composition of 50 GeV jets, but 200 GeV jets will show a different composition, with higher energy particles making up a larger fraction of the total jet energy.

The above results were calculated using Pythia jets which were free of both underlying event and initial state radiation. The jet energy response was also calculated using the Herwig and ISAJET Monte Carlo event generators, which

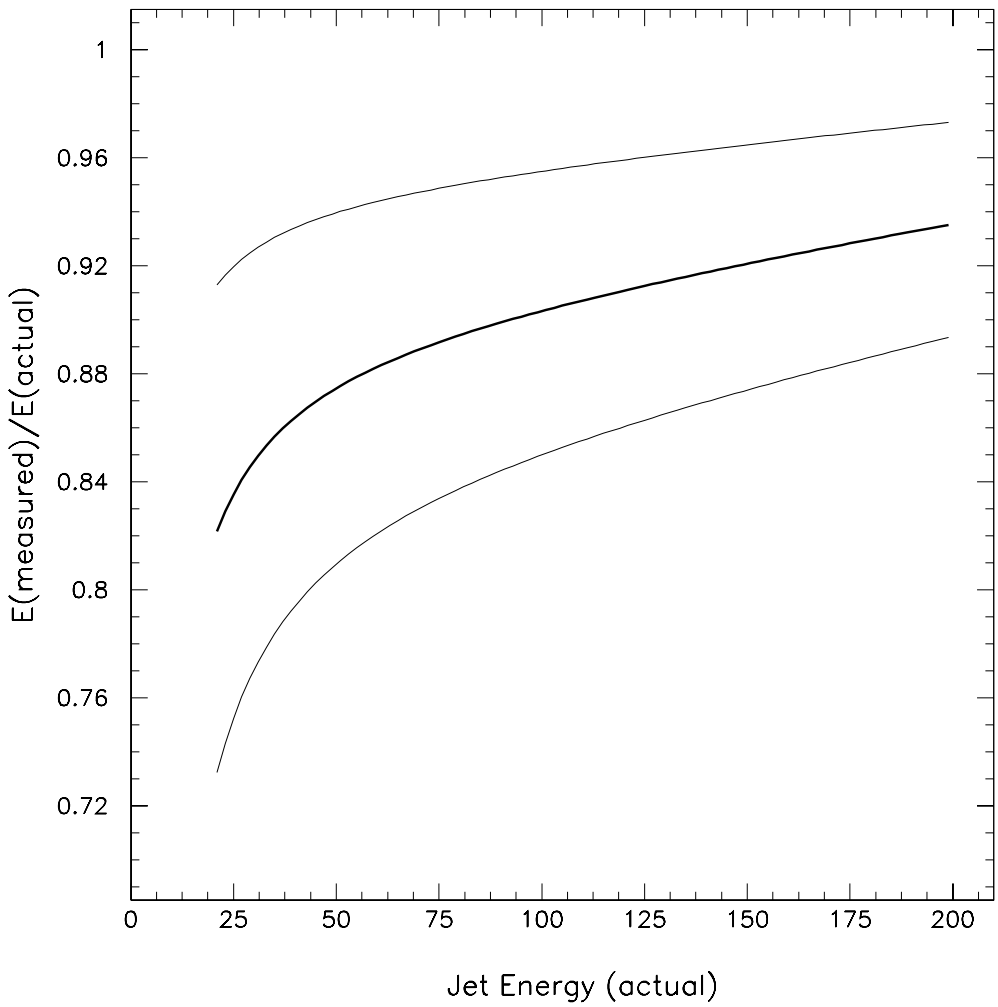

Figure 5.36: Nominal jet energy scale and limits of errors. The thick line is the nominal response and the thin lines are the upper and lower limits.

include both of the above-mentioned effects. Despite this, the results were seen to agree with the Pythia results to within 1.5%[28].

Since there is no reliable test beam data below 2 GeV, the response in that energy region is not known. In this study the response below 2 GeV, both for pions and electrons, was taken to be the same as the response used at 2 GeV. The question of how the jet response curve changes using other reasonable choices of single particle responses below 2 GeV are explored below for three reasonable cases:

- If the electron response continued to drop as an extrapolation of the test beam data the jet response would be 2% lower for 50 GeV jets and 1% lower for 150 GeV jets.

- The pion response is expected to increase at very low energy since charged pions begin to act like minimum ionizing particles. Assuming the response increases to 100% at 1 GeV increases the response by 2% for 50 GeV jets and 0.5% for 150 GeV jets.

- If the pion response continues to decrease as an extrapolation of test beam data, then the jet response decreases by 2% for 50 GeV jets and 1% for 150 GeV jets.

The uncertainties due to very-low-energy particle response uncertainty are seen to be much less than the uncertainties already present and can therefore be safely ignored.

The magnitude of such shape-dependent effects as out-of-cone showering and zero-suppression are estimated using actual test beam single-particle events added together using the ISAJET fragmentation scheme[29]. The out-of-cone effect in the central region was seen to be of the order of 3-4 %. Zero-suppression, as discussed above, tends to add a constant amount of energy (measured from calorimeter cell pedestal distributions to be 2.1 - 2.4 GeV for a jet with cone

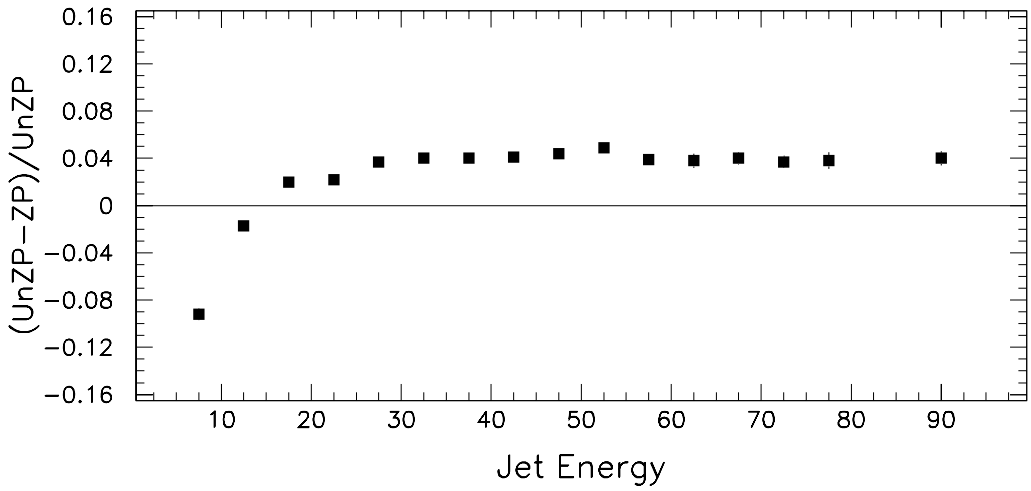

Figure 5.37: Energy lost due to zero-suppression of data for jets with cone size $R = 0.7$. Plotted is ((unsuppressed energy) - (suppressed energy))/(unsuppressed energy) versus suppressed jet energy.

size $R = 0.7$) as well as subtract an energy-dependent amount. By using unzero-suppressed data and comparing the jet energies before and after zero-suppression we obtain the energy-dependence of this effect as shown in Figure 5.37. These effects and others will be discussed in more detail later.

Jet Energy Scale from Direct Photon P_T balance

The Missing E_T Projection Fraction (MPF) method was used by the CDF collaboration[30] on dijet events in order to calibrate high-η jets. Here it will be used to derive an absolute jet energy scale using our knowledge of the electromagnetic energy scale and P_T balance of direct photons events. The MPF method is useful in this application since it comes close to giving us the true calorimeter response to jets and minimizes effects of multiple jets in the event and the differences between jet and photon showering and reconstruction algorithms. A method simply using the reconstructed jet and photon E_T to calibrate would be sensitive to these effects and require either more stringent cuts (and hence a reduced data

sample) or additional, as yet undetermined, corrections.

The events we will use consist of a mixture of actual direct photon events and jet events where one jet fluctuates into mostly electromagnetic energy and is reconstructed as an isolated photon. In that sense, the word "photon" will be used loosely here. In the following analysis, the photons and jets are restricted to the central calorimeter, $|\eta_\gamma| < 1.0$, and $|\eta_{jet}| < 0.7$. The η's used here are detector η, the actual position in the calorimeter calculated from the physics η and the z-vertex. The jet cone size used is the same as that of the analysis as a whole, $R = 0.7$.

The MPF used here is defined as

$$MPF = \frac{\vec{\not{E}}_T \cdot \hat{n}_T^{jet}}{E_T^{jet}},$$

where $\hat{n}_T^{jet}$ is the unit vector giving the transverse direction of the jet with $E_T = E_T^{jet}$. The missing E_T vector is defined as the sum over calorimeter cells:

$$\vec{\not{E}}_T = -\sum_i E_T^i \hat{n}_i, \quad i = \text{calorimeter cell number.}$$

The unit vector $\hat{n}_i$ is transverse to the beam line and points in the direction of the ith calorimeter cell.

For the case of a photon balanced by a single jet the operation of the MPF is straightforward (Figure 5.38.) We assume the calorimeter response to the photon is 100% and the response to the jet is R. If E_T^{jet} is the uncorrected reconstructed E_T of the jet and E_T^{corr} is the actual jet E_T, then $R = E_T^{jet}/E_T^{corr}$. If $R \neq 1$ then there will be a $\vec{\not{E}}_T$ component along the jet direction and:

$$\vec{\not{E}}_T \cdot \hat{n}_T^{jet} = E_T^{corr} - E_T^{jet}.$$

Then:

$$MPF = \frac{\vec{\not{E}}_T \cdot \hat{n}_T^{jet}}{E_T^{jet}} = \frac{E_T^{corr} - E_T^{jet}}{E_T^{jet}} = \frac{E_T^{corr}}{E_T^{jet}} - 1 = \frac{1}{R} - 1$$

so that the jet response R may be written in terms of the MPF as:

$$R = \frac{1}{1 + MPF}.$$

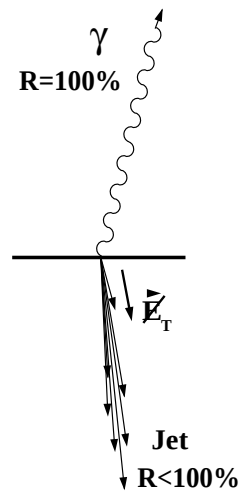

Figure 5.38: Direct photon event with single jet balancing P_T. If the calorimeter response to both the photon and jet is 100%, then the reconstructed missing E_T is zero. If the jet response is less than 100%, then there will be a reconstructed missing E_T vector pointing along the direction of the jet that is equal to the jet E_T lost due to low response.

If $R > 1$ then the $\vec{\not{E}}_T$ will point opposite to the jet and the MPF will be negative. Essentially this method operates by balancing P_T along the direction of the jet, thereby minimizing the effect of out-of-cone showering of the jet, including partonic radiation out of the cone which is observed as another jet in the event.

If a second jet is present due to either initial state or final state gluon bremmstrahlung, the situation will be as shown in Figure 5.39. Depending on its E_T, this jet may or may not be reconstructed due to the jet reconstruction threshold which requires the jet to have 8 GeV of E_T. Now equating $\vec{\not{E}}_T \cdot \hat{n}_T^{jet}$ with $E_T^{corr} - E_T^{jet}$ is only approximate since the response of the second jet (which may be different than the response of the first) is included in the $\vec{\not{E}}_T$. Taking the dot product with the transverse direction of the first jet minimizes this contamination, which will be zero if the direction of the second jet is uncorrelated with the direction of the first (just as likely to add as to subtract from the $\vec{\not{E}}_T$.) If the direction of the second jet is correlated with the direction of the first this will tend to lower

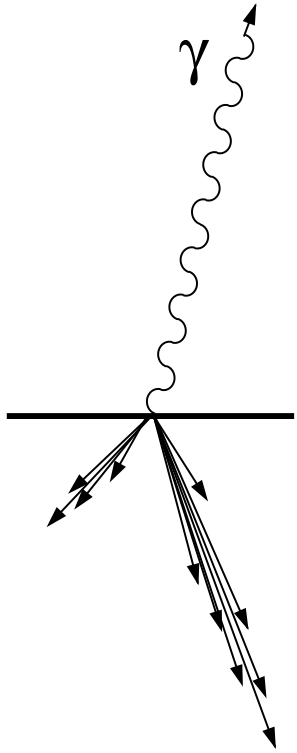

Figure 5.39: Direct photon event with two balancing jets

the apparent response of the first jet since the second jet is lower in energy (hence response) than the first. The following simulation will serve to put limits on the magnitude of any perturbative effects.

The MPF-derived jet response calculation was tested using HERWIG[31] generated direct photon events as well as dijet events where one jet fluctuated into mostly electromagnetic energy (π^0's) so as to simulate a direct photon event. The PJETS particle jet finder was used to find jets in the data and the photons (or π^0's) were required to be isolated as described below.

The simulation was accomplished by scaling each particle by an assumed energy- and η-dependent response and smearing with test beam energy- and η-dependent resolution. What is termed the "actual" jet response is the sum of all the response-altered particle energies in the given PJET divided by its unaltered

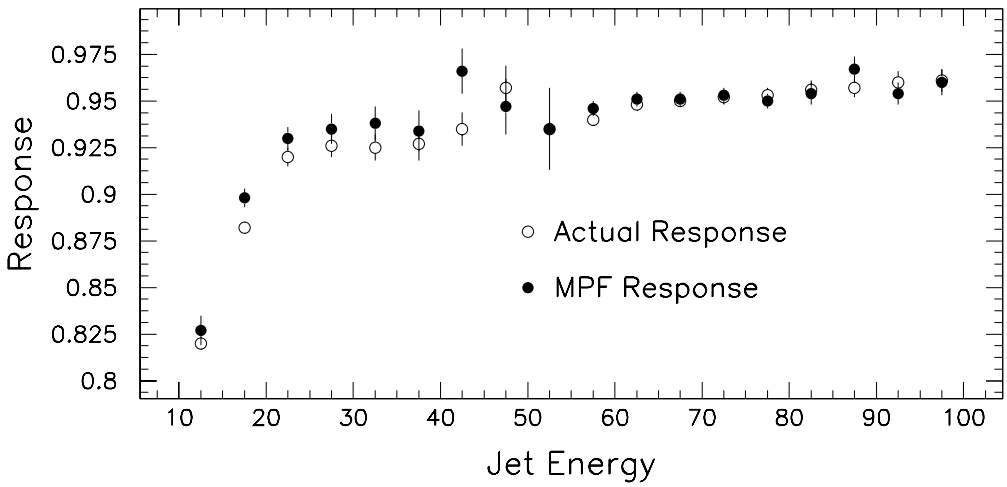

Figure 5.40: Comparison of "actual" jet response (open circles) and MPF-derived response (solid circles) using HERWIG generated direct photon events and simulated calorimeter single particle responses and resolutions.

particle energy sum (the same as the method described earlier in this section.) The missing E_T is simply the opposite of the sum of all the response-altered particles in the event with $|\eta| < 4.0$. Since jets are composed of some sizable fraction of low-energy particles with a low calorimeter response, the missing E_T should reflect this by pointing toward the largest cluster of low-response particles, just as it should in the actual calorimeter.

The results of the simulation using simulated direct photon data is shown in Figure 5.40. The highest E_T jet was used and required to have $|\eta| < 1$. The open circles are from the "actual" response using only the particles in the jet cone and the solid circles are from the MPF-derived response. The data was generated in two bins of photon E_T, from 10 - 50 GeV and 50 - 150 GeV, hence the poor statistics in the range 30 - 50 GeV. The agreement is seen to be very good (within 0.5%) over a large range in jet E_T.

The following variations of cuts, response and resolution were made in order to study the effects on the comparison between actual and MPF-derived

response and all were found to have minimal ($< 0.5\%$) impacts on the comparison either singly or in various combinations:

- Requiring only one jet and one photon, i.e., no second reconstructed jet in the event.

- Requiring photon and jet to be back-to-back in ϕ to within 50 degrees.

- Simulate ICD/MG cryostat crack region by lowering electromagnetic particle scale by 10%, lowering hadronic particle scale by 5% and doubling the smearing (particle resolution) in the region $1.0 < |\eta| < 1.5$. In this case both the photon and jet were restricted to the region $|\eta| < 1$.

- The electromagnetic particle response was lowered everywhere by 10%. The MPF-derived response was then seen to be exactly 10% higher than the actual jet response. This indicates that the MPF-derived response can be easily corrected using the known electromagnetic response.

Results of these simulations show that the MPF method is very insensitive to other activity (besides the photon and highest E_T jet) in the event for direct photons. However, the actual direct photon sample to be used is considerably contaminated with π^0's from jet fragmentation that simulate isolated direct photons. These events might have different event topologies or other effects that might lead to discrepancies between the MPF method and the actual jet energy scale.

The π^0 portion of the calibration data was simulated using HERWIG dijet events where one jet was required to fragment into a π^0 that carried at least 50% of the jet E_T. The jets were generated in the E_T range from 55 - 65 GeV and the π^0's were required to be isolated. The results are shown in Figure 5.41 and the agreement is seen to be within the statistical uncertainties.

Several conclusions may be drawn from the simulation studies:

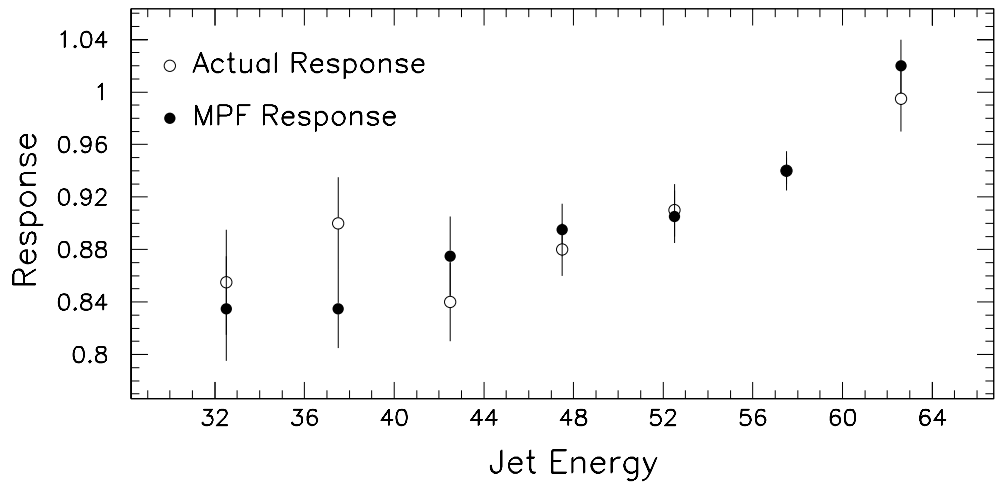

Figure 5.41: Comparison of "actual" jet response (open circles) and MPF-derived response (solid circles) using HERWIG generated electromagnetic jet events and simulated calorimeter single particle responses and resolutions.

- The MPF method gives excellent agreement with the actual response over a large range in jet E_T. This indicates that contamination due to multiple jets is not a major factor.
- Photon (or π^0) must be restricted to a detector region where the response is known.
- Where electromagnetic response is known to be different than unity, simply correct using the known electromagnetic response.

There are some aspects of the calorimeter that the Monte Carlo cannot simulate very well or at all and therefore cannot be studied. It an effort to homogenize the photon/π^0 response into something that we can hopefully measure, cuts are made on the data to remove photons that may have gone into cracks, may be noisy cells, may be charged π's, etc.

Events are selected from the direct photon trigger sample using the following requirements:

- The photon must be above the 95% trigger efficiency point (7 GeV for GAM_LOW_ISO, 15 GeV for GAM_MED_ISO and 30 GeV for GAM_HIGH_ISO.)

- The jet E_T must be 30% above the photon threshold to prevent the photon threshold from biasing the response distribution (10 GeV for GAM_LOW_ISO, 20 GeV for GAM_MED_ISO and 40 GeV for GAM_HIGH_ISO.)

- A photon isolation requirement is made by determining whether there is a significant fraction of energy in a cone of radius 0.4 outside the core cone of radius 0.2.
$$\frac{(E_T \text{ in } 0.2 \text{ cone})}{(E_T \text{ in } 0.4 \text{ cone})} > .85.$$

- The reconstructed z-vertex must be within 40 cm of the nominal center point of the detector.

- The photon cannot be within 0.01 radians of a CCEM ϕ crack.

- There must be at least one reconstructed jet in the event.

- If there is more than one reconstructed jet, the 2nd jet (ordered in E_T from highest to lowest) must have $E_T < 15$ GeV.

- All the reconstructed jets in the event must pass the following cuts to remove events with jets due to noisy cells or main ring activity (see §5.2.1):

  - Cell Ratio =(highest E_T cell)/(2nd highest cell) < 10.

  - Coarse Hadronic fraction $< .4$.

  - $.05 <$ Electromagnetic fraction $< .95$.

- As an additional cut on noisy cells, the $\not{E}_T$ must be less than 90% of the photon E_T.

A missing E_T correction is applied to correct for the transverse shift of the vertex position. The average $\vec{\not{E}}_T$ ($E_{T_x} = 1.00$ GeV, $E_{T_y} = -.55$ GeV) is subtracted from the $\vec{\not{E}}_T$ of each event. While this constant shift will not effect the average MPF, it should reduce the fluctuations about the average.

With the cuts and corrections explained above, the MPF-derived energy-dependent response for jets with $|\eta| < .7$ and photons with $|\eta| < 0.9$ is shown in Figure 5.42. The fit shown is:

$$R = \frac{E_0}{1.6494 + 1.0495 E_0}$$

where $R = E_0/E^{corrected}$ is the response and E_0 is the uncorrected reconstructed jet energy. The fit was made over the range from 15 to 125 GeV and the error-weighted values were used. The fit is somewhat sensitive to the range used, the weighting and the form of the fit and can change by up to 2% depending on these choices. The statistics above 100 GeV are very poor and the extrapolation of the fit to much higher energies (up to 400 GeV) adds additional uncertainties that depend greatly on the form of the fit. The form used here fit the test beam data well from 25 to 400 GeV. These uncertainties are shown in Figure 5.42 by the dashed lines.

As shown earlier, if the calorimeter response to the photon is less than 100% then an additional correction must be applied to the jet energy. Currently our best estimate for the electromagnetic scale is from reconstructed decays of the Z^0 particle, which has been measured using collider data to be a factor of 1.088 below the accepted value of 91.2 GeV from LEP experiments[32]. Approximately 4.5% of the total of 8.8% is understood in terms of differences in high voltage and liquid argon, etc., between the DØ and the test beam calorimeters. The remaining difference cannot be explained. On the basis of this, the correction applied is energy independent (we know 4.5% of it is) and an uncertainty is energy dependent. The uncertainty used is 0.5% at a jet energy of 40 GeV (where the scale is best known from Z^0 decays) and increases linearly to 4.0% at 10 GeV and at 440 GeV. This scale factor is assumed to effect both the electromagnetic and hadronic sections

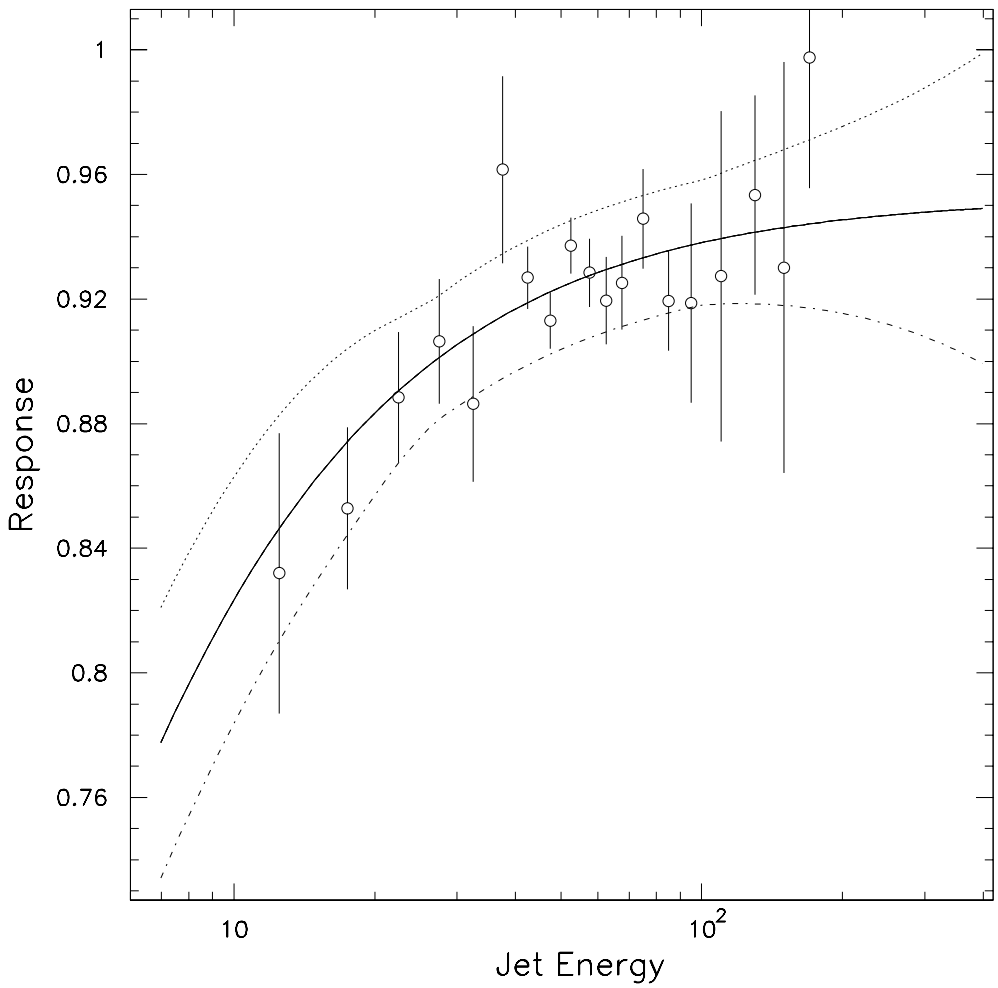

Figure 5.42: Jet energy response using the MPF method. The best fit is shown by the solid line and the limits of the uncertainties by the dashed lines

equally, and the 4.5% accounted for is such an overall correction. If part of the correction is not and only effects the electromagnetic, then only the jet resolution is effected and the overall scale obtained above is not.

Hadronic particles in the jet make broad showers in the calorimeter, and if they are near the edge of the cone, may shower energy into calorimeter cells outside the cone. This can also be calculated by using the test beam shower sizes and a Monte Carlo event generator[33]. This effect was determined to be mostly energy independent, and is corrected for using the multiplicative factor $1.04 \pm .02$.

There are two effects which cause energy unassociated with the jet to be added into the cone. Zero-suppression, as discussed earlier in this section and in Chapter 4, adds a constant average energy to each cell due to a positive-side tail on the calorimeter pedestal distribution and underlying events add a constant transverse energy due to the breakup of the proton and antiproton involved in the collision. This E_T must be subtracted since it is not associated with the jets but is a uniform (on average) background to each event. This has been measured using MIN_BIAS trigger events (events where no jets were required, only a level 0 signal for the breakup of a proton or antiproton) to be 3.0 ± 0.5 inside a jet cone of radius 0.7 in the central region[34]. Additionally, one can measure the so-called "jet pedestal", the amount of energy deposited at a point perpendicular (in ϕ) to the jets in dijet events. This has been done[35] and a value of 4.0 GeV obtained for a jet with radius 0.7 in the central calorimeter. The zero-suppression background is the same for each, while the underlying event is:

- different, due to the difference in the momentum scale of the interaction for the two processes.
- differently measured, since part of the jet pedestal measurement may be due to partons from the primary hard scatter causing an overestimate of the underlying event.

For these reasons, the energy offset is chosen as 3.0 ± 1.0 GeV, where the MIN_BIAS

measurement is considered more reliable but the uncertainty does encompass the jet pedestal measurement as well.

The order in which the corrections are applied is very important and is accomplished as follows:

- Correct using response from central jet-photon MPF method.
- Subtract zero-suppression and underlying event energy.
- Correct for electromagnetic scale response from measured Z^0 mass.
- Correct for out-of-cone effect in the central region.

The effects of the electromagnetic scale correction, the out-of-cone showering correction, and the energy offset (zero-suppression and underlying event) on the jet response are shown in Figure 5.43.

5.3.2 Jet Energy Scale at Large η

Once we know how to calibrate jets in the central region, one can use P_T balance of dijet events to extend the calibration to all regions of the calorimeter. By selecting dijet events which have one jet in the central ($|\eta| < 0.7$) region (hereafter referred to as the "central" jet) and the other jet anywhere (the "probe" jet) the ratio of the probe jet E_T to the central jet E_T gives the probe jet response relative to the central jet, which we already know how to calibrate.

Event selection begins by requiring each event to have only two reconstructed events with $E_T > 10$ GeV and these jets must be back-to-back in ϕ to within 25 degrees. One of the two jets must have detector $|\eta| < 0.7$. In order to minimize trigger biases, the average jet E_T must be greater than the trigger efficiency threshold (see Table 5.3.) When both the central and probe jet have $|\eta| < 0.7$, the central jet is chosen at random. Fake jets are removed using the same cuts as discussed in §5.2.1. If either of the two highest E_T jets fails any fake

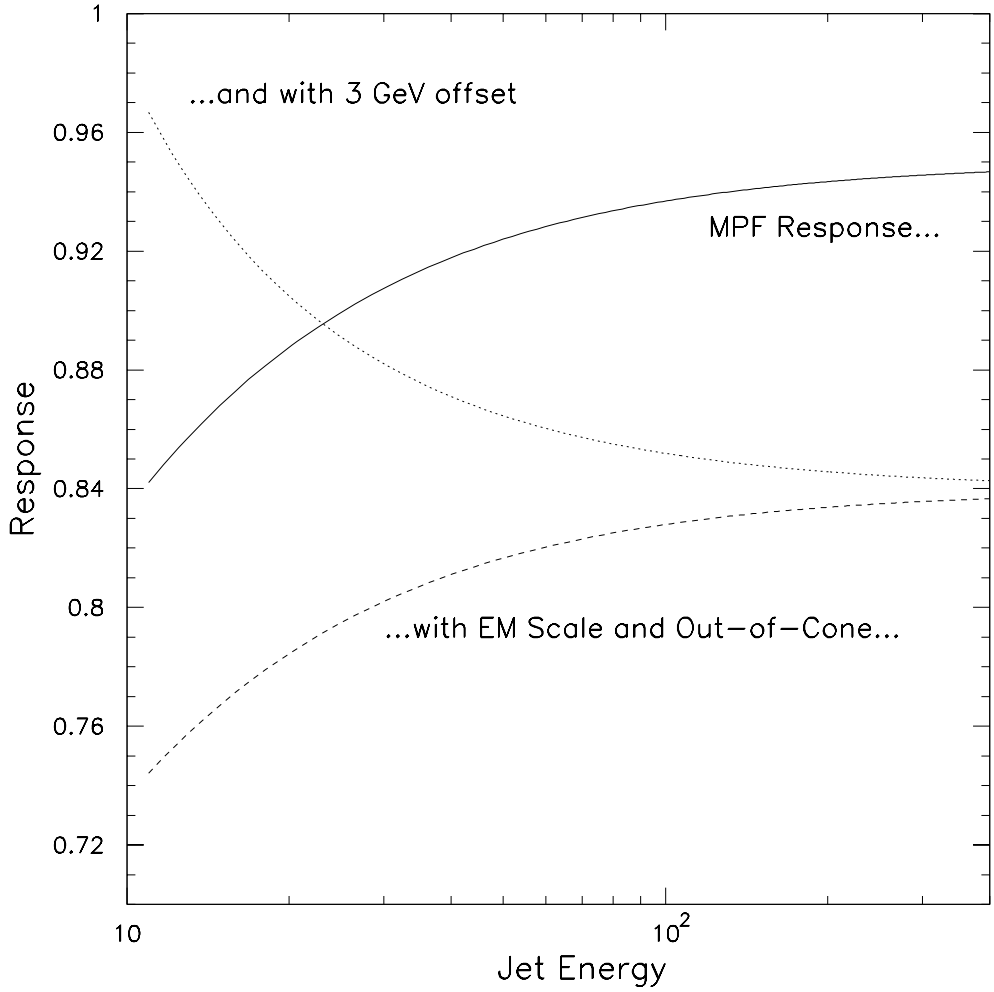

Figure 5.43: Jet energy response in the central calorimeter using the MPF method and effects of corrections.

jet cut, then the event is not used. Additionally, the event z-vertex is required to be within 100 cm of the detector center.

The "asymmetry"

$$A = (E_T^{probe} - E_T^{central})/(E_T^{probe} + E_T^{central})$$

is calculated for each event and plotted versus detector η of the probe jet. With this definition, the relative response of the probe jet is

$$R = E_T^{probe}/E_T^{central} = (1 + A)/(1 - A).$$

The results of this analysis are shown in Figure 5.44 for various bins of average jet E_T. The cryostat crack region is seen to be over-corrected due in part to a known calibration problem with the inter cryostat detectors (ICD's.) One might expect the response at large η to be better than in the central region due to the fact that, since the jet E_T's are similar, the jet energy is much higher in the forward region. Figure 5.44 shows that the response is similar in the central and forward regions. This may be due to a cancellation due to large out-of-cone showering effects for high-η jets.

The forward response can also be determined using the Missing E_T Projection Fraction (MPF) method introduced in §5.3.1. Using the same sample of dijet events, the MPF is calculated using this definition:

$$MPF = \frac{\vec{\not{E}}_T \cdot \hat{n}_T^{probe}}{E_T^{probe} + E_T^{central}}.$$

Where $E_T^{central}$ is the transverse energy of the central jet and $\hat{n}_T^{probe}$ is the unit vector along the probe jet direction in the transverse plane. The missing E_T, $\vec{\not{E}}_T$, is the vector sum of the $\vec{E_T}$ of all the calorimeter cells. Now the MPF can be assumed to represent the fractional difference in probe jet E_T to central jet E_T,

$$MPF = \frac{E_T^{central} - E_T^{probe}}{E_T^{probe} + E_T^{central}} = (1 - R)/(1 + R)$$

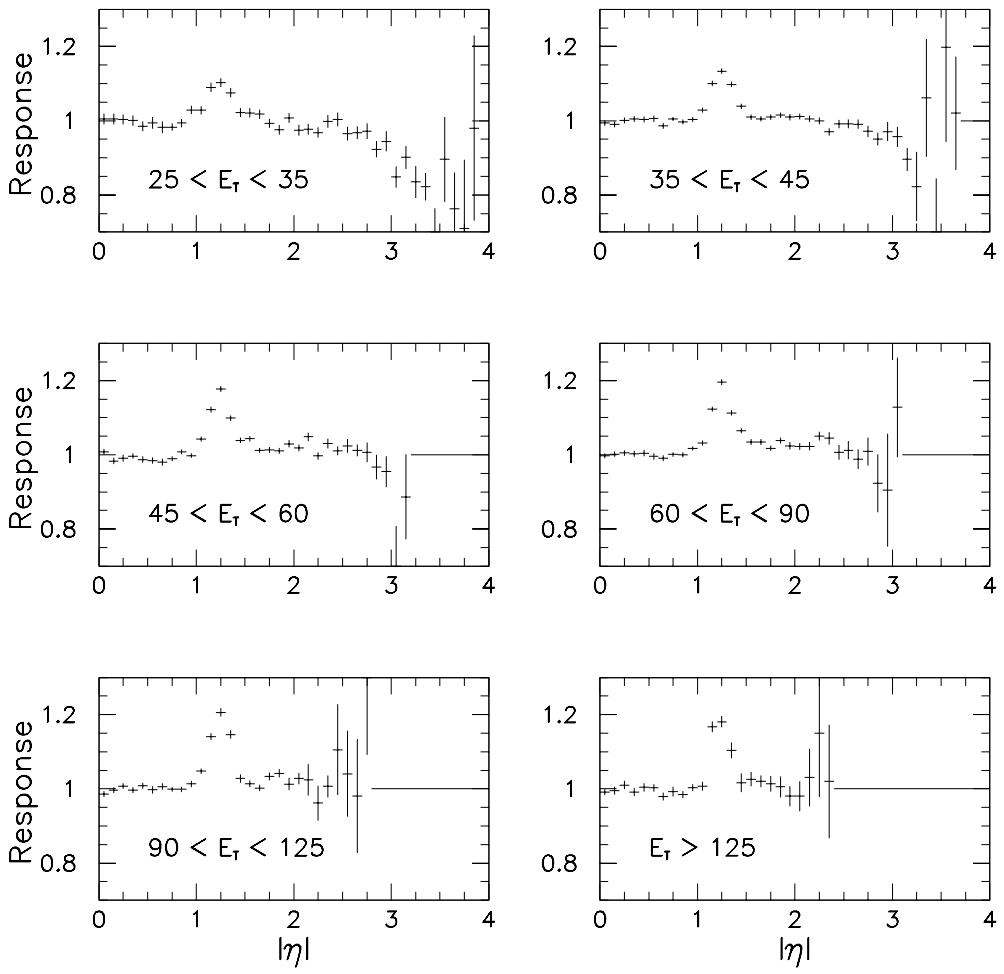

Figure 5.44: Jet energy response versus detector η using dijet P_T balance asymmetry.

where R is the response of the probe jet since the central jet is calibrated. The response calculated in this manner $R = (1-MPF)/(1+MPF)$ is shown in Figure 5.45. Note that the MPF method shows a distinctly higher response at high $|\eta|$ that is not shown by the jet E_T asymmetry method of Figure 5.44. The MPF method, which uses the entire calorimeter to balance P_T, is insensitive to out-of-cone showering effects, and so shows how the calorimeter response increases as the jet energy increases. The jet E_T ratio method is sensitive to both increasing response for higher energies as well as the out-of-cone showering effect, which increases for higher $|\eta|$. This difference can be seen in the higher relative response obtained from the MPF method as compared to the dijet asymmetry method in Figures 5.44 and 5.45.

The full energy correction now can proceed by first correcting using the dijet asymmetry (Figure 5.44.) This scales the jet energy to the corresponding central jet with the same E_T. Then the corrections listed at the end of the previous section can be employed. The complete correction proceeds as follows, starting with a jet at $\theta = \theta_0$ with energy E_0:

1. Do η-dependent correction from dijet asymmetry(A) to get $E' = E_0/A$. This scales the jet to a central jet with the same E_T.

2. Correct using response from central jet-photon MPF method. The relevant energy to use is the E_T of the forward jet, namely $E' \sin\theta_0$ to get the proper response.

3. Subtract zero-suppression energy and underlying event energy appropriate for a central jet.

4. Correct for electromagnetic scale response from Z^0 mass as measured in the central calorimeter.

5. Correct for out-of-cone effect in the central region.

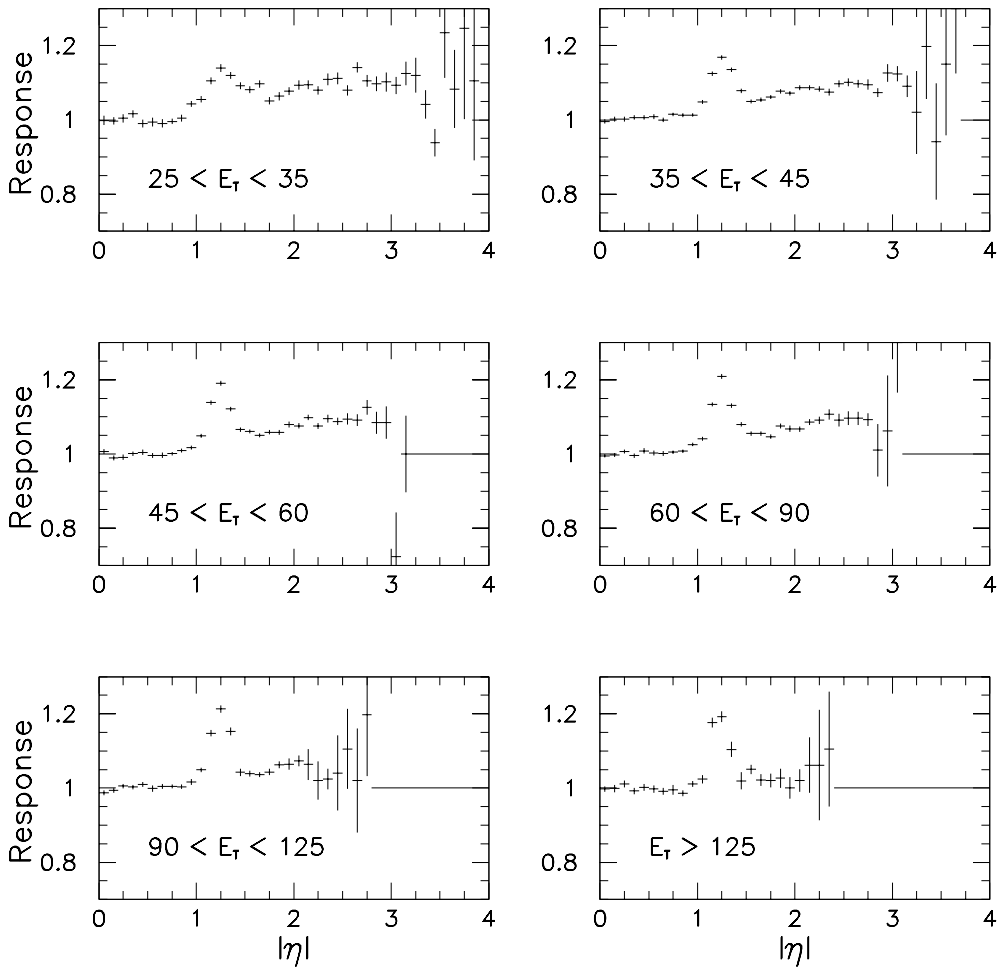

Figure 5.45: Jet energy response versus detector η using dijet P_T balance and the MPF method.

The uncertainty in the procedure is due mainly to threshold biases arising from jet energy resolution η-dependence. Consider the case where one jet is in the crack region and the other is central and both have the same E_T. Since the resolution in the crack region is much worse than that of the central region and the cross-section falls steeply with increasing E_T, it is more likely for the jet in the crack region to fluctuate from a lower to a higher E_T and cause the event to pass the threshold than it is for the central jet to fluctuate higher. One might expect then that the response in the crack region would appear to be higher than it actually is. The uncertainty used is zero for $|\eta| < 1.0$ (where the dijet asymmetry method is not used) and increases linearly thereafter to 4% at $|\eta| = 3.0$.

Addendum: η-dependent biases.

At a point late in the process of writing this document, it was discovered that large systematic biases are possible due to differing energy resolutions in different regions of the detector. For example, consider a two jet event where each jet has 25 GeV E_T and one jet is at $\eta = 0.0$ and the other at $\eta = 3.0$. Using the resolutions determined in the next section, the central jet has $\sigma(E)/E = .18$ and the endcap jet has $\sigma(E)/E = .08$. Since the cross section falls rapidly with increasing jet E_T, this smearing and the threshold requirement conspire to bias the calculated η-dependent response. Since the smearing is much larger in the central region, it is more likely for a low-E_T jet there to be smeared higher and cause the event to pass the threshold cut than it is for the endcap jet to do so[36].

Preliminary studies indicate that this effect is large for low E_T and high η jets. For the E_T range from 25 to 35 GeV, it ranges from 3% at $|\eta| = 2.0$ to 8% at $|\eta| = 3.5$. For the E_T range from 35 to 45 GeV, it ranges from 2% at $|\eta| = 2.0$ to 5% at $|\eta| = 3.5$. This mainly effects results from the low E_T triggers, JET_MIN and JET_LOW, making the resultant distributions steeper as a function of χ. The effects on the other (higher E_T) triggers is most likely negligible.

5.3.3 Jet Energy Resolution

The asymmetry variable can also be used to measure jet energy resolution. By selecting only dijet events, then the asymmetry, A, defined as

$$A = \frac{E_{T_1} - E_{T_2}}{E_{T_1} + E_{T_2}}$$

has a width that may be written as follows:

$$(\sigma_A)^2 = \left(\left| \frac{\partial A}{\partial E_{T_1}} \right| \sigma_{E_{T_1}} \right)^2 + \left(\left| \frac{\partial A}{\partial E_{T_2}} \right| \sigma_{E_{T_2}} \right)^2$$

$$= \left[\left(\frac{2E_{T_2}}{(E_{T_1} + E_{T_2})^2} \right) \sigma_{E_{T_1}} \right]^2 + \left[\left(\frac{2E_{T_1}}{(E_{T_1} + E_{T_2})^2} \right) \sigma_{E_{T_2}} \right]^2$$

Assuming $E_{T_1} = E_{T_2}$ and $\sigma_{E_{T_1}} = \sigma_{E_{T_2}}$ then

$$(\sigma_A)^2 = \left[\left(\frac{2E_T}{(2E_T)^2} \right) \sigma_{E_T} \right]^2 + \left[\left(\frac{2E_T}{(2E_T)^2} \right) \sigma_{E_T} \right]^2 = \frac{1}{2} \left(\frac{\sigma_{E_T}}{E_T} \right)^2$$

we obtain the result for the fractional transverse energy resolution:

$$\left(\frac{\sigma_{E_T}}{E_T} \right) = \sqrt{2} \sigma_A$$

where we have ignored other effects which could widen the asymmetry distribution such as η position smearing and transverse boosts of the dijet system from physical sources such as additional unreconstructed low E_T jets and transverse momentum of the partons in the colliding hadrons. Through event selection, we will attempt to minimize these effects. The corrected E_T is used to calculate the asymmetry and the resolution is plotted versus the average of the two jets corrected energy.

Dijet events are selected using the following cuts:

- Only 2 reconstructed jets above 10 GeV.
- Both jets must have $E_T > 15$ GeV.
- Jets must be back-to-back in ϕ to within 25 degrees.

- z-vertex must be within 100 cm of detector center.
- Both the reconstructed jets must pass the fake jet cuts (see §5.2.1):
  - Cell Ratio =(highest E_T cell)/(2nd highest cell) < 10.
  - CH fraction $< .4$.
  - $.05 <$ Em fraction $< .95$.

Events are grouped into bins according to η (detector η) where both jets are required to be in a certain region of the detector in order that our approximation of $\sigma_{E_{T_2}} = \sigma_{E_{T_1}}$ is appropriate. The central region ($|\eta| < 0.8$) has uniform calorimetry and most additional smearing effects are minimal. The crack region ($0.8 < |\eta| < 1.5$) is not uniform due to the cryostat walls and other uninstrumented material. The resolution should be much worse there than in the central region. In the endcaps ($1.5 < |\eta| < 3.0$) the systematic effects mentioned above dominate despite the cuts since the η resolution is a much larger effect and all the events are low E_T, thereby more sensitive to transverse fluctuations. For this reason, we will also use the Monte Carlo to determine the energy resolution in a manner similar to the method used to obtain the position resolution (§4.2.2.)

Figure 5.46 shows the measured resolution, σ_{E_T}/E_T, versus E for the central and crack regions of the detector described above. Both the dijet asymmetry method and the Monte Carlo results are shown. The Monte Carlo resolution in the central region agrees quite well with the measured resolution. Note that the crack region does have much worse resolution than the central and that the Monte Carlo reproduces it reasonably well except for one data point at high energy. For these two regions, the actual data will be used to determine the fits, whereas in the forward region, the Monte Carlo data will be used. The data for the three calorimeter regions is shown in Figure 5.47 Energy resolution fits of the form:

$$\left(\frac{\sigma_E}{E}\right)^2 = \left(\frac{N}{E}\right)^2 + \left(\frac{S}{\sqrt{E}}\right)^2 + (C)^2$$

Table 5.5: Jet energy resolution fit parameters.

η region		Noise(N)	Sampling(S)	Constant(C)
$0.0 < \|\eta\| < 0.8$	Central	1.74	.860	0.016
$0.8 < \|\eta\| < 1.5$	Crack	7.81	.349	0.117
$1.5 < \|\eta\| < 3.0$	Endcap	1.97	1.10	0.034

have been made and the results are in Table 5.5.

Although the forward region uses virtually the same calorimetry as the central, the energy resolution is worse there than in the central region. This is due to the large out-of-cone effect we measured earlier. If the jet cone does not contain 100% of the jet energy, then jet-to-jet fluctuations of jet width will mean large fluctuations in measured energy. Also, the η position resolution is folded into the energy resolution for endcap jets, but this contribution is only 5-10% and can be safely ignored.

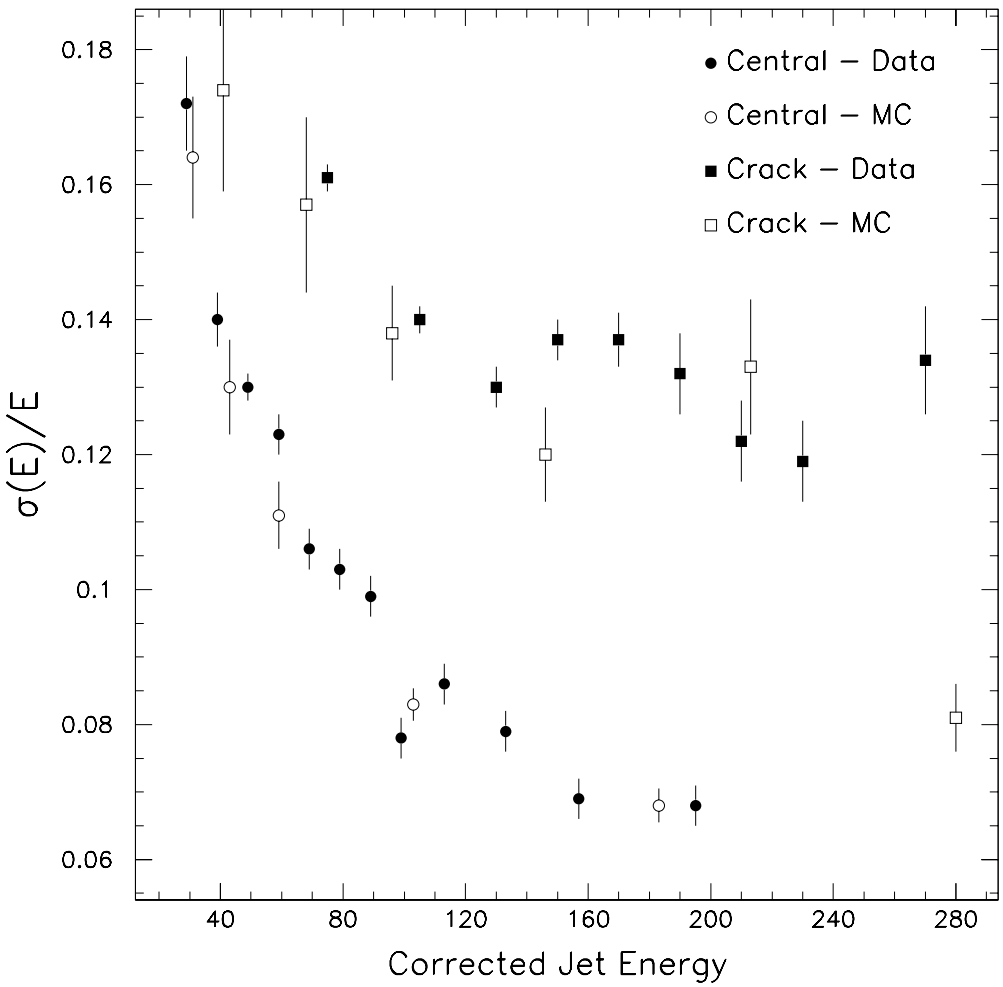

Figure 5.46: Jet transverse energy resolution versus jet energy using the asymmetry for two regions of the detector. Actual data is compared to Monte Carlo resolution and the agreement is seen to be good.

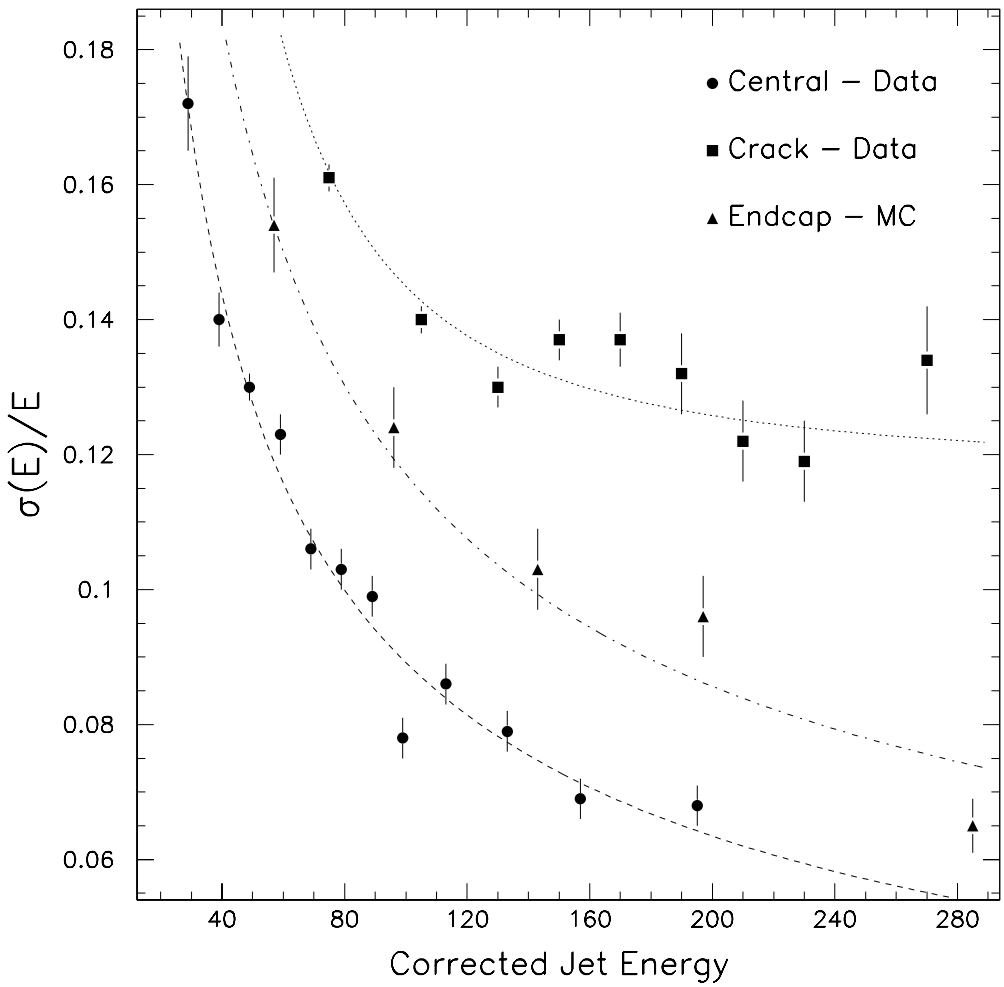

Figure 5.47: Jet energy resolution versus energy using the asymmetry for the central and crack region and Monte Carlo results for the end region. Resolution fits are shown for each region.

CHAPTER 6

Results

Before any data can be presented, we must use our knowledge of the detector's ability to detect and measure jets to calculate the acceptance as a function of the angular variable of interest. The acceptance is simply the ratio of number of events measured to number of events actually in a given bin. Once we know how to relate what we measure to physical reality, we can correct our distributions and compare to theoretical predictions. The ramifications of these distributions will then be explored in terms of agreement with QCD and evidence for parton compositeness.

6.1 Acceptance Corrections

The acceptance is calculated using the Papageno[37] event generator and comparing unmolested distributions with those that have been smeared using known energy and position resolutions and efficiencies. The smeared distribution will then be compared to the unsmeared distribution.

The Papageno generator produces simple two-parton events with no initial state radiation, parton showering or fragmentation. Each generated event consists of the η and P_T of the two partons. A weight for each event is calculated using the matrix elements and parton density functions for the given kinematic parameters.

The unsmeared distribution is obtained first by selecting events based on dijet mass (M_{JJ}) and dijet longitudinal boost ($|\eta_{boost}|$.) Exactly the same thresholds are used here as will be used on the actual data. The $|\eta_{boost}|$ cut is used to extend the region of good acceptance to larger angles, since events with both large $|\eta_{boost}|$ and large center-of-mass angle means one of the two jets will be very far forward, either outside the triggerable region or even outside the detector.

The $|\eta_{boost}|$ threshold selection is based on how far in η^* we hope to go. This can be demonstrated using the definitions:

$$\eta_{boost} = \frac{1}{2}(\eta_1 + \eta_2)$$

$$\eta^* = \frac{1}{2}(\eta_1 - \eta_2)$$

which means that

$$\eta_1 = \eta^* + \eta_{boost}$$

$$\eta_2 = -\eta^* + \eta_{boost}.$$

So that if we plan on measuring η^* out to 2.0, say, and we must have both jets with $|\eta| < 3.5$ (contained in the calorimeter) then we must require $|\eta_{boost}| < 1.5$ or the acceptance will begin dropping before we reach $\eta^* = 2.0$.

The major factor that limits acceptance is the single jet E_T threshold imposed by the trigger. We can use the approximate equation for dijet mass from §2.6 to show how this is so. Remember,

$$M_{JJ} = 2E_T \cosh \eta^*$$

for two jets with the same E_T. This can be written in terms of η^* as:

$$\eta^* = \cosh^{-1}\left(\frac{M_{JJ}}{2E_T}\right).$$

If our triggers had perfect step-function-like thresholds, then the higher limit in η^* could be determined using the trigger threshold and the dijet mass threshold only. Although this simple approximation does work reasonable well for obtaining the η^* limit in acceptance, the detailed acceptance calculation to follow can show any deviations from flat over the whole range in η^*.

The smearing process consists of several steps which will now be discussed in detail. First, each parton is considered to be a jet and smeared as follows:

1. The measured jet E_T is determined using the Papageno energy and position and inverting the jet energy correction. This is required since the jet energy

and position resolutions are known in terms of measured jet E_T, not corrected jet E_T. The uncertainties in the jet energy correction process will be handled separately from the acceptance calculations.

2. The E_T is smeared using the jet E_T resolution fits as determined in §5.3.3. Different fits are used depending on jet η position.

3. The jet η and ϕ positions are smeared using the position resolution determined in §4.2.2.

4. The jet energy correction is now applied to the smeared energy and position.

After we have obtained a smeared energy and position for each jet, new 4-vectors are calculated and the smeared M_{JJ}, η^*, and η_{boost} are obtained. Cuts (the same as used on the unsmeared distribution) are then placed on the smeared M_{JJ} and η_{boost} as well as the average uncorrected jet E_T.

Next we determine the efficiency for this configuration of jets to pass the fake jet cuts. The requirements made on the data are that the electromagnetic fraction of the two jets be between .05 and .95 and that the coarse hadronic fraction be below 0.4 (See §5.2 for more details.) Using the full detector simulation the efficiencies, $\epsilon(\eta, E_T)$, for these cuts (shown in Figures 5.31 and 5.32) are parameterized as follows:

$$\epsilon = .995 - \frac{1}{E_T^{1.4}} \quad |\eta| < .8$$

$$\epsilon = 1 - (.03744 + .0005663 E_T) \exp\left[-\left(\frac{|\eta| - 1.05}{.15}\right)^2\right] \quad .8 < |\eta| < 1.4$$

$$\epsilon = .995 \quad |\eta| > 1.4$$

Since these are single jet efficiencies, the total fake jet cut event efficiency is the product of the efficiency of each jet and is used to modify the weighting for each event in the distribution.

Lastly the trigger efficiency for the dijet configuration is calculated. Since the trigger is in two steps, level 1 and level 2 (see §3.4 and §5.1), an efficiency for

each level will be determined and the event efficiency will be the product of the two:

$$\epsilon_{total} = \epsilon_{L1}\epsilon_{L2}.$$

The level 2 efficiency is determined from the single jet level 2 efficiencies in the following way:

$$\epsilon_{L2} = 1 - (1 - \epsilon_1)(1 - \epsilon_2)$$

where ϵ_i is the level 2 efficiency of jet i. Whereas the total efficiency requires both level 1 and level 2 to fire (a Boolean "and"), here we require one "or" the other jet to cause a trigger, hence the different mathematical equations.

The level 1 efficiency depends on the η and E_T of both jets. For the simplest case of a one-tower trigger such as JET_MIN or JET_LOW, which requires one trigger tower with E_T greater than a certain threshold, the process is the same as that for level 2 efficiencies above. If ϵ_i is the efficiency for jet i to have caused a trigger tower to go above threshold, then the total level 1 efficiency is

$$\epsilon_{L1} = 1 - (1 - \epsilon_1)(1 - \epsilon_2).$$

For triggers which require two or more towers above threshold, the equations become more complicated. For JET_MEDIUM, which requires 2 towers over 7 GeV E_T, there are now three different ways this can be satisfied: one or the other jet could fire two towers or each jet could fire one tower. If ϵ_j^i is the efficiency for jet i to fire j trigger towers, then the expression for the total level 1 efficiency is:

$$\epsilon_{L1} = 1 - (1 - \epsilon_2^1)(1 - \epsilon_2^2)(1 - \epsilon_1^1\epsilon_1^2).$$

This can be extended to 3 trigger towers (JET_HIGH):

$$\epsilon_{L1} = 1 - (1 - \epsilon_3^1)(1 - \epsilon_3^2)(1 - \epsilon_1^1\epsilon_2^2)(1 - \epsilon_2^1\epsilon_1^2)$$

or 4 towers (JET_MAX):

$$\epsilon_{L1} = 1 - (1 - \epsilon_4^1)(1 - \epsilon_4^2)(1 - \epsilon_2^1\epsilon_2^2)(1 - \epsilon_1^1\epsilon_3^2)(1 - \epsilon_3^1\epsilon_1^2).$$

Table 6.6: Mass ranges and triggers used to plot dijet angular distributions.

Mass Range	$\lvert\eta_{boost}\rvert$ Cut	Trigger Name	χ limit	η^* limit	$\cos\theta^*$ limit	Number of Events
100 - 150	2.0	JET_MIN	14	1.32	.86	11000
150 - 250	2.0	JET_LOW	14	1.32	.86	18000
250 - 350	1.5	JET_LOW	49	1.95	.96	4600
350 - 450	1.5	JET_MEDIUM	35	1.76	.94	2200
450 - 550	1.5	JET_HIGH	20	1.50	.90	1200
550 -	1.5	JET_MAX	13	1.28	.86	450
450 -	.9	JET_LOW	180	2.60	.99	550

The trigger efficiencies obtained are then used to weight the events as they enter the distribution. This smeared distribution is then divided by the unsmeared distribution to obtain the acceptance. Note that this method is sensitive to the choice of input (unsmeared) distribution. Leading order QCD with $Q^2 = P_T^2/4$ was used in the calculation above. The dependence of the acceptance on the form of the input distribution was tested by comparing the results obtained using a flat (pure Rutherford scattering) versus χ distribution and comparing with the results obtained above. The difference in shape was seen to be less than 1%.

The acceptances were calculated for the mass ranges and triggers shown in Table 6.6. As can be seen, each trigger is used for one plot of a certain range in mass, with the exception of JET_LOW, which is used for three, one utilizing a high mass threshold to generate a distribution which extends to very large angles. Nearly 400,000 events were taken with this trigger, far more than any other, making it the most useful for the large-angle distribution.

The acceptances for all 7 combinations of triggers and dijet mass ranges have been generated and are shown as acceptance vs. χ in Figures 6.48 and 6.49. The limit that will be used when plotting the data is shown in Table 6.6. The lines indicate the systematic uncertainties which will be discussed in the next section.

Several features of the acceptance curves are noteworthy. The intermediate and high mass acceptances are seen to increase slightly as the angle increases, this

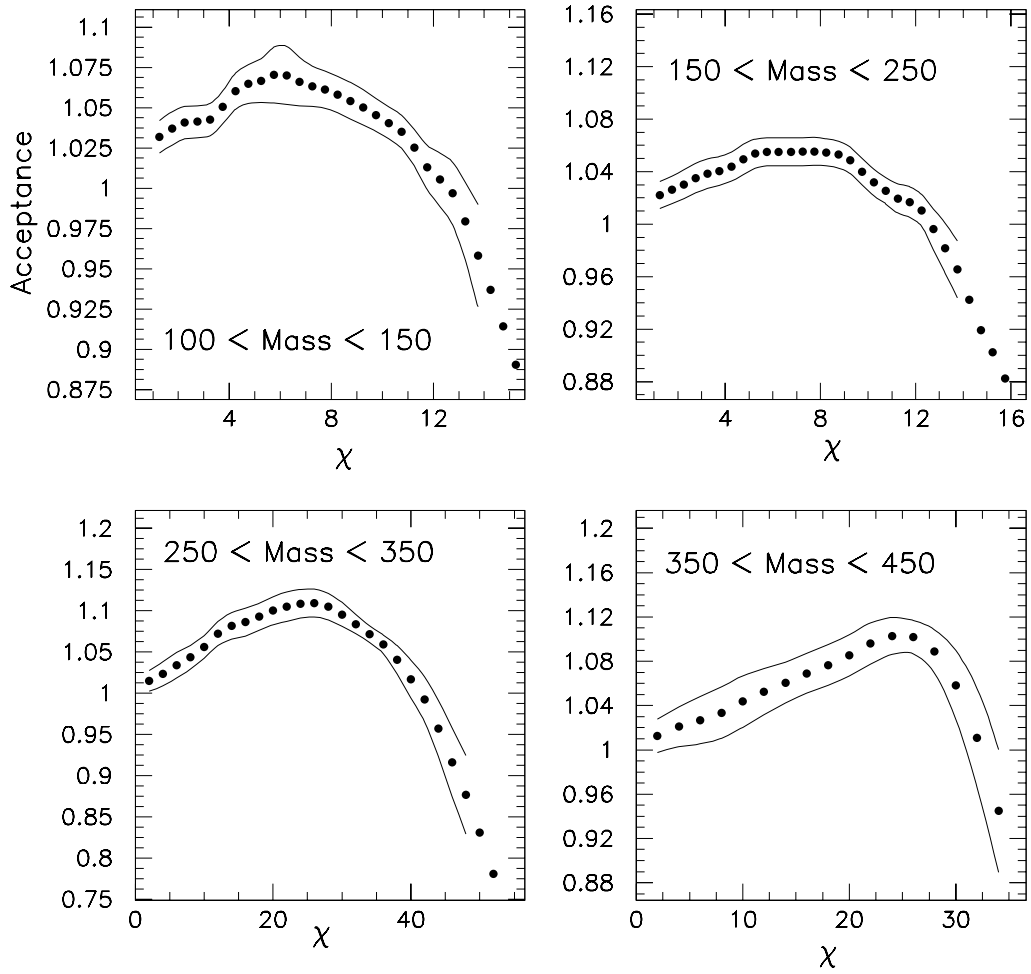

Figure 6.48: Acceptance versus χ for different mass ranges.

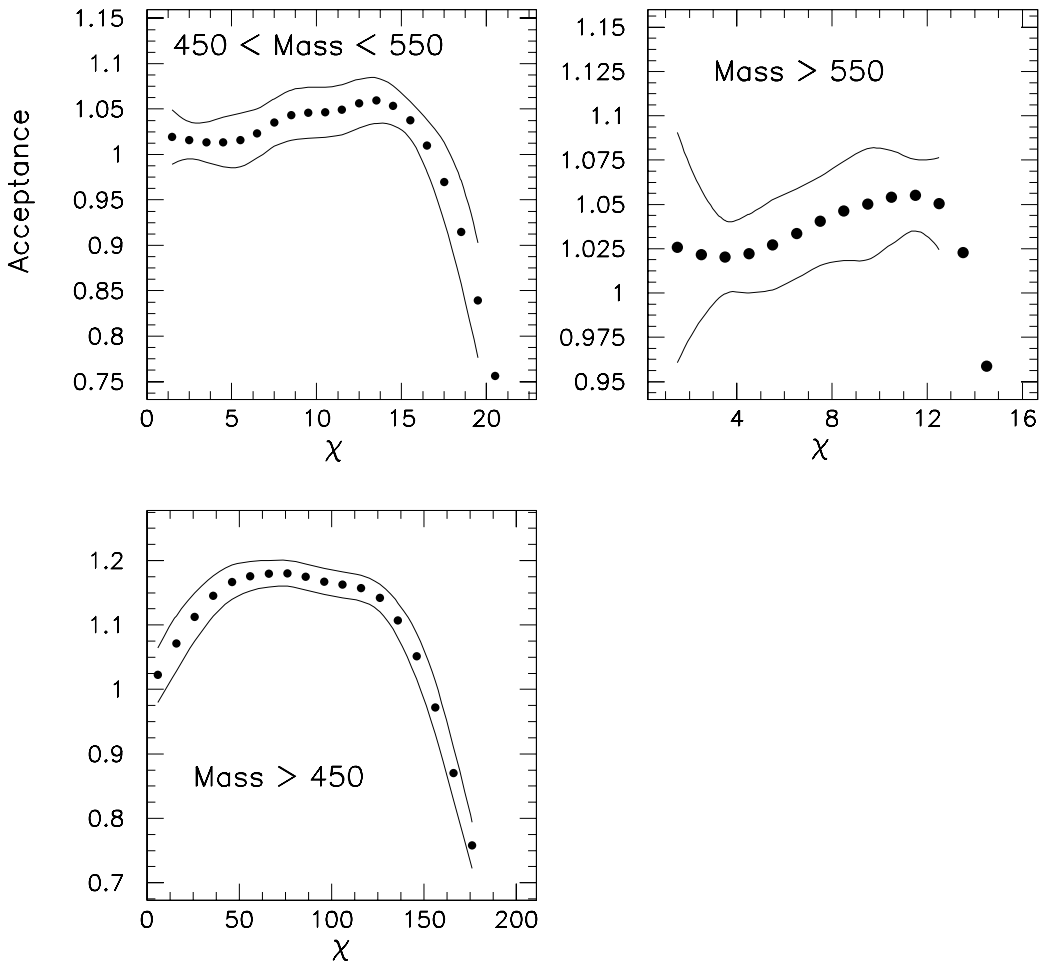

Figure 6.49: Acceptance versus χ for different mass ranges.

is due to mass smearing from lower masses to above-threshold masses (also called "feed-down effect") that increases at larger angles where the jet energy resolution is worse. Generally the acceptances are quite flat, varying by 5-10% typically over the range used. The χ limit can be seen to correspond to the point where the acceptance begins to drop steeply. The JET_LOW $M_{JJ} > 450$ GeV plot is the exception. In order to extend the measured range as far as possible, the useable acceptance was allowed to drop to nearly 70%.

6.2 Systematic Uncertainties

The systematic uncertainties consist of two independent parts; the uncertainty in acceptance and the energy scale uncertainty. The uncertainties in the acceptances shown in the above Figures are derived from uncertainties in the jet trigger efficiencies, the fake jet cut efficiencies, and the resolution and position smearing. Also included is the possible systematic η shift uncertainty. One of the largest effects is the fake jet cut efficiency uncertainty in the crack region, which is due mainly to poor Monte Carlo statistics there and uncertainty in applicability of the Monte Carlo results in this complex region. Also a large effect, the η position resolution uncertainty is somewhat large due to questions about the simulation's reliability. Overall, though, the flatness of the acceptance over the large ranges in angle mean the uncertainties are small, ranging from 2% to 5% depending on trigger and mass range.

The energy scale uncertainty makes a larger contribution to the overall systematic uncertainty. The slope of the χ distribution depends on the parameters of the energy correction to some extent. The relevant parameters of the energy scale include the response of the jet relative to the photon, the electromagnetic scale and out-of-cone correction, the underlying event energy, and the dijet P_T-balance η-dependent correction, each of which has an associated uncertainty as discussed in §5.3. To obtain the effect on the angular distribution, the $dN/d\chi$ distributions are generated three times using actual data. Once using the nominal energy scale,

once using the uncertainty limits on the energy scale parameters which cause the distribution to steepen, and lastly using the limits that cause the distribution to flatten in slope. The curves are then normalized to each other so that if the slopes are different, they will all cross in the middle. The energy scale uncertainty is then determined by measuring the difference in the curves at the extremes of χ. For instance, if the difference between the flatter curve and the nominal curve is 7% at one end and 8% at the other, and the steeper curve is 6% different at one end and 7% different at the other, then the energy scale uncertainty is the average of these four numbers, or 7%. This reflects the uncertainty in the slope due to the uncertainty in the energy scale.

The single largest effect is the uncertainty in the slope of the jet-photon response. In Figure 6.50 the nominal as well as the flattest and steepest reasonable fits to the data. The data and the form of the fits are the same as that used in §5.3.1 and shown in Figure 5.42. The lack of substantial data above a jet energy of 100 GeV is the major cause of this uncertainty. This effect alone is responsible for about 5% of the total systematic uncertainty.

At lower masses, the energy offset (zero-suppression and underlying event) uncertainty is a large effect as well, contributing up to 4% to the total systematic uncertainty in the shape of the distributions. At higher masses (larger angular range) the η-dependent uncertainty was a large effect, up to a 6% contribution for the large χ range plot (JET_LOW, $M_{JJ} > 450$ GeV.)

The energy scale and acceptance uncertainties are independent and so are added in quadrature to obtain an overall systematic uncertainty. In the $dN/d\chi$ distributions, this error is shown separately from the data, which has only statistical error bars.

6.3 Dijet Angular Distributions

The distributions for the seven mass ranges in Table 6.6 will be shown plotted as $dN/d\chi$ versus χ where both the data and the theory have been normalized to unity

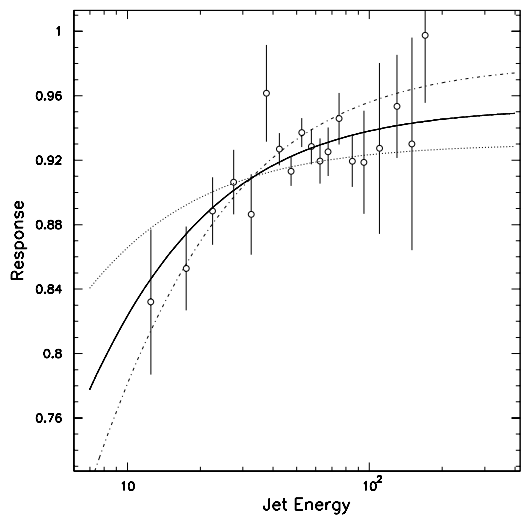

Figure 6.50: Nominal and upper and lower limits of slope of the jet response.

over the range in χ used. The $O(\alpha_s^2)$ predictions have been generated using $Q^2 = P_T^2/4$ and MRS S0 [7] parton distributions. The NLO curves have been generated using the choice $Q^2 = \left(\frac{M_{JJ}}{4\cosh(0.7\eta^*)}\right)^2$ (see §2.6.3.) If this choice of scale was used for the leading order curves, the result would be almost indistinguishable from the NLO curves. The form used for the $O(\alpha_s^3)$ scale was not known beforehand, it was only available after the NLO predictions were calculated. Before the $O(\alpha_s^3)$ predictions, there was no reason to doubt that the choice $Q^2 = P_T^2/4$ was not the best one to make. It is on this basis, therefore, that the leading order predictions are presented using this momentum scale, that it is the *a priori* leading order QCD scale choice.

Note that due to expansion of possibilities of the form of Q from $Q = AP_T$ to $Q = AM_{JJ}/2\cosh B\eta^*$ that virtually any (positive) slope of the leading order curve is attainable by a suitable choice of parameters. However, the NLO curve is much less sensitive to the scale choice due to cancellation in the higher order terms. Ellis, Kunszt, and Soper determined that for changes of a factor of two

about the nominal scale choice (A=0.5, B=0.7), the slope of the leading order curve varied by 40% whereas the NLO curve varied by only 10%, indicating much less dependence on the scale at $O(\alpha_s^3)$[11].

As mentioned in §2.6.1, the Collins-Soper angle gives a more accurate definition of the center-of-mass angle in the presence of transverse boosts of the dijet system. It is useful to compare the result using each angular definition. In Figure 6.51 we see the comparison between the distributions derived using the Collins-Soper angle and the simpler definition for mass ranges $100 < M_{JJ} < 150$ GeV and $250 < M_{JJ} < 350$ GeV. A slight difference is seen in the low mass plot where the Collins-Soper angle gives a slope that is about 5% steeper than the simple angular definition. No difference between the two methods is visible in the higher mass range, presumably since only at the lowest masses are transverse boosts large enough to perturb the measurements. But perhaps the difference is simply lost in the larger statistical errors of the higher mass ranges.

Comparisons to $O(\alpha_s^2)$ plots will be made using the Collins-Soper angle. The $O(\alpha_s^3)$ predictions, however, were calculated using the simple definition $\eta^* = \frac{1}{2}(\eta_1 - \eta_2)$ where jets 1 and 2 are the two highest E_T jets in the event. These calculations can have up to 3 jets in the event, so the dijets can be boosted transverse to the beam. Therefore, using the Collins-Soper angle to compare with $O(\alpha_s^3)$ predictions would be incorrect and the definition used in the theory calculation will also be used in the data for all such comparisons. Since the distributions obtained using each definition is the same for masses above 250 GeV, those plots will be shown only once, using the definition $\eta^* = \frac{1}{2}(\eta_1 - \eta_2)$ to compare to both $O(\alpha_s^2)$ and $O(\alpha_s^3)$ QCD predictions.

We are now prepared to show the acceptance-corrected angular distributions for the 7 mass ranges and trigger combinations of Table 6.6. We will go through each mass range and show the relevant angular distributions along with the theoretical predictions and a short discussion of the results. A summary of the results of the fits appears in Table 6.7.

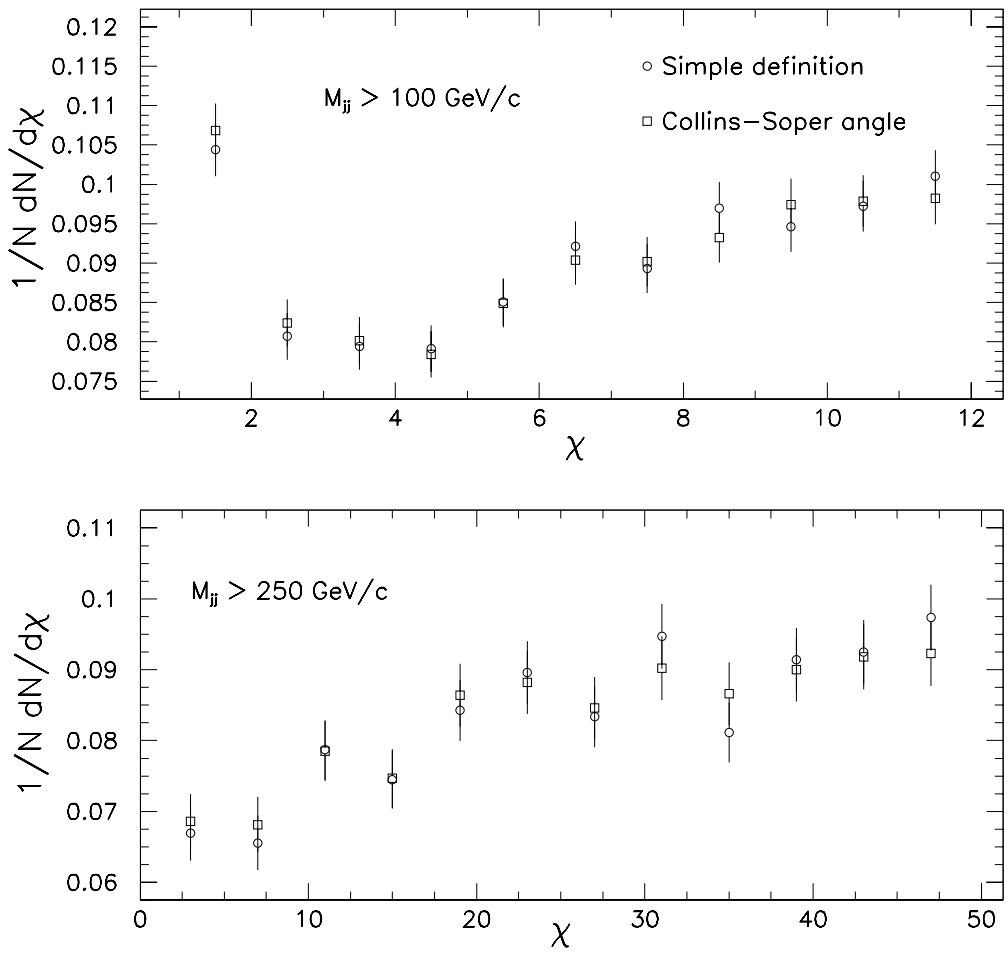

Figure 6.51: Comparison of angular distributions $dN/d\chi$ vs. χ using the simple definition $\eta^* = \frac{1}{2}(\eta_1 - \eta_2)$ and the Collins-Soper angle. Two different mass ranges are shown and no acceptance corrections have been made.

JET_MIN: $100 < M_{JJ} < 150$ **GeV**

The $O(\alpha_s^2)$ QCD prediction is compared to the distribution obtained using the Collins-Soper angle in Figure 6.52. The distribution obtained using the $\eta^* = \frac{1}{2}(\eta_1 - \eta_2)$ definition is shown in Figure 6.53 compared to both leading and next-to-leading order QCD predictions. The data is seen to prefer the steeper $O(\alpha_s^2)$ QCD prediction over the $O(\alpha_s^3)$ curve. In fact the data has a slightly steeper slope than even the leading order curve[1]. The NLO prediction is a very poor fit, with a 7% significance level. Only the large size of the systematic uncertainty (6.5% compared to 5% statistical) prevents us from ruling out the NLO curve. Since the major difference between the leading and the next-to-leading order predictions is the steeper slope of the leading order curve, and all the curves are normalized to unity, the major discrepancies will be seen at the extremes of the plots.

JET_LOW: $150 < M_{JJ} < 250$ **GeV**

The $O(\alpha_s^2)$ QCD prediction is compared to the distribution obtained using the Collins-Soper angle in Figure 6.54. The distribution obtained using the $\eta^* = \frac{1}{2}(\eta_1 - \eta_2)$ definition is also shown in Figure 6.55 compared to both leading and next-to-leading order QCD predictions. The tendency is also towards the steeper $O(\alpha_s^2)$ curve, although now the data is closer to the shape of the NLO prediction. The systematic uncertainties (which here are 5.4%, much larger than the statistical error of about 3.5%) again dominate and make it impossible to state a preference.

JET_LOW: $250 < M_{JJ} < 350$ **GeV**

The data is compared to $O(\alpha_s^2)$ and $O(\alpha_s^3)$ QCD predictions in Figure 6.56. For these masses and above the difference between the Collins-Soper and $\eta^* = \frac{1}{2}(\eta_1 - \eta_2)$ is negligible so the latter definition will be used since that is what is used to derive

[1] This may be due in part to the η-dependent bias discussed at the end of §5.3.2. The correction for this effect was not applied in the data shown and tends to steepen distributions which rely on low-E_T jets. This effects mainly the plots $100 < M_{JJ} < 150$ GeV and $150 < M_{JJ} < 250$ GeV

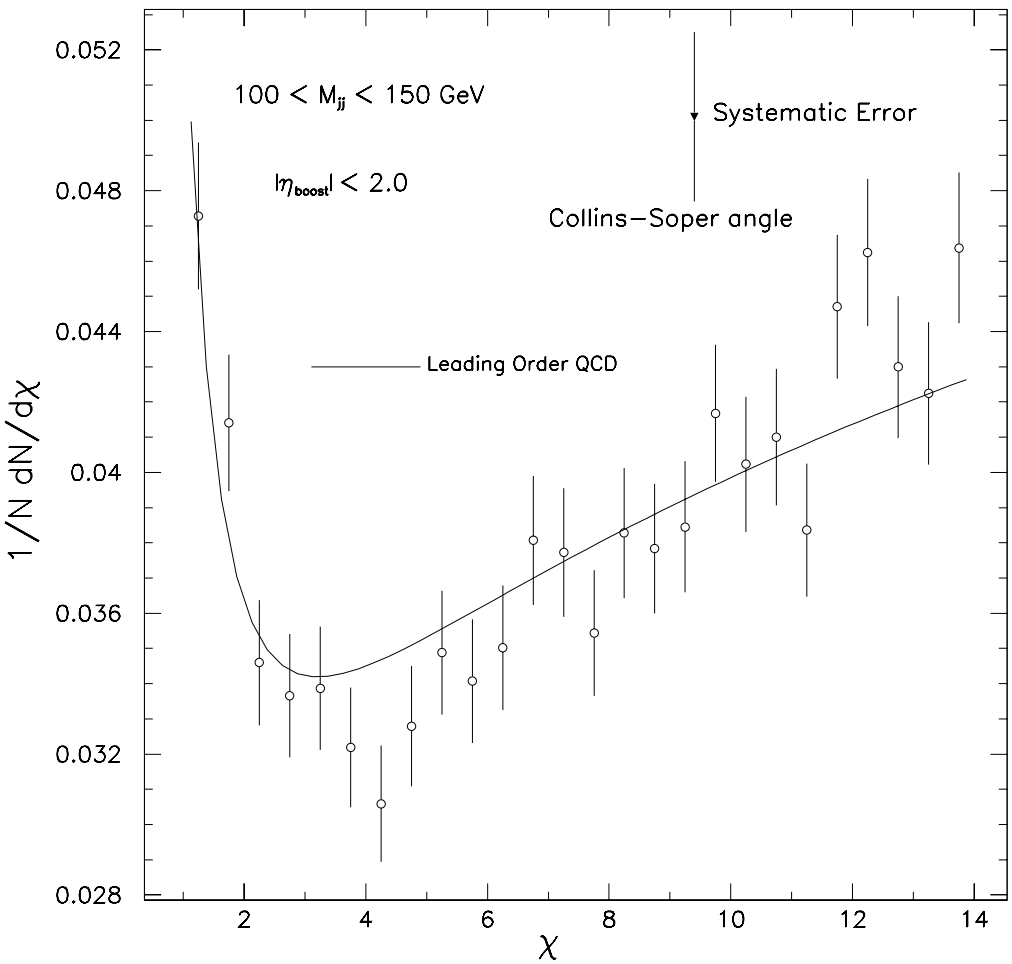

Figure 6.52: $dN/d\chi$ versus χ for $100 < M_{JJ} < 150$ distribution obtained using the Collins-Soper angle and compared to leading order QCD.

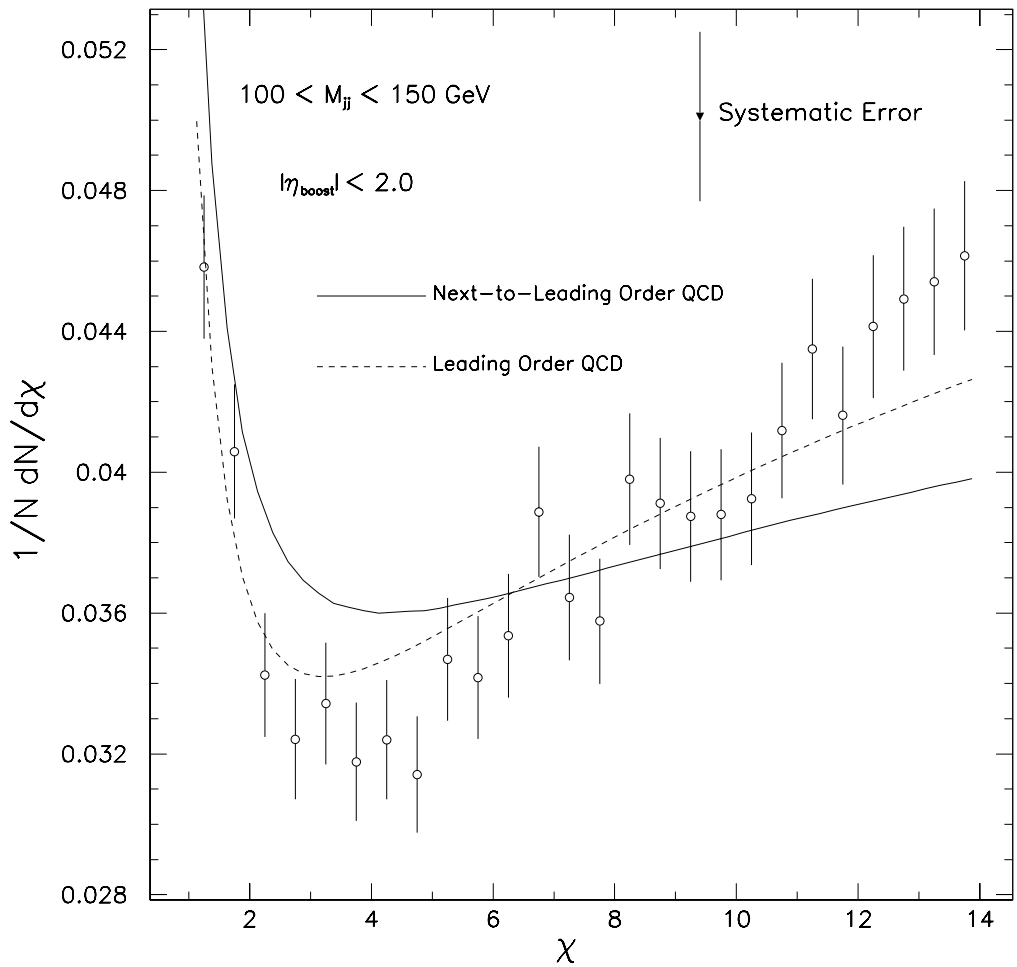

Figure 6.53: $dN/d\chi$ versus χ for $100 < M_{JJ} < 150$ distribution obtained using the simple definition $\eta^* = \frac{1}{2}(\eta_1 - \eta_2)$ compared to both leading order and next-to-leading order.

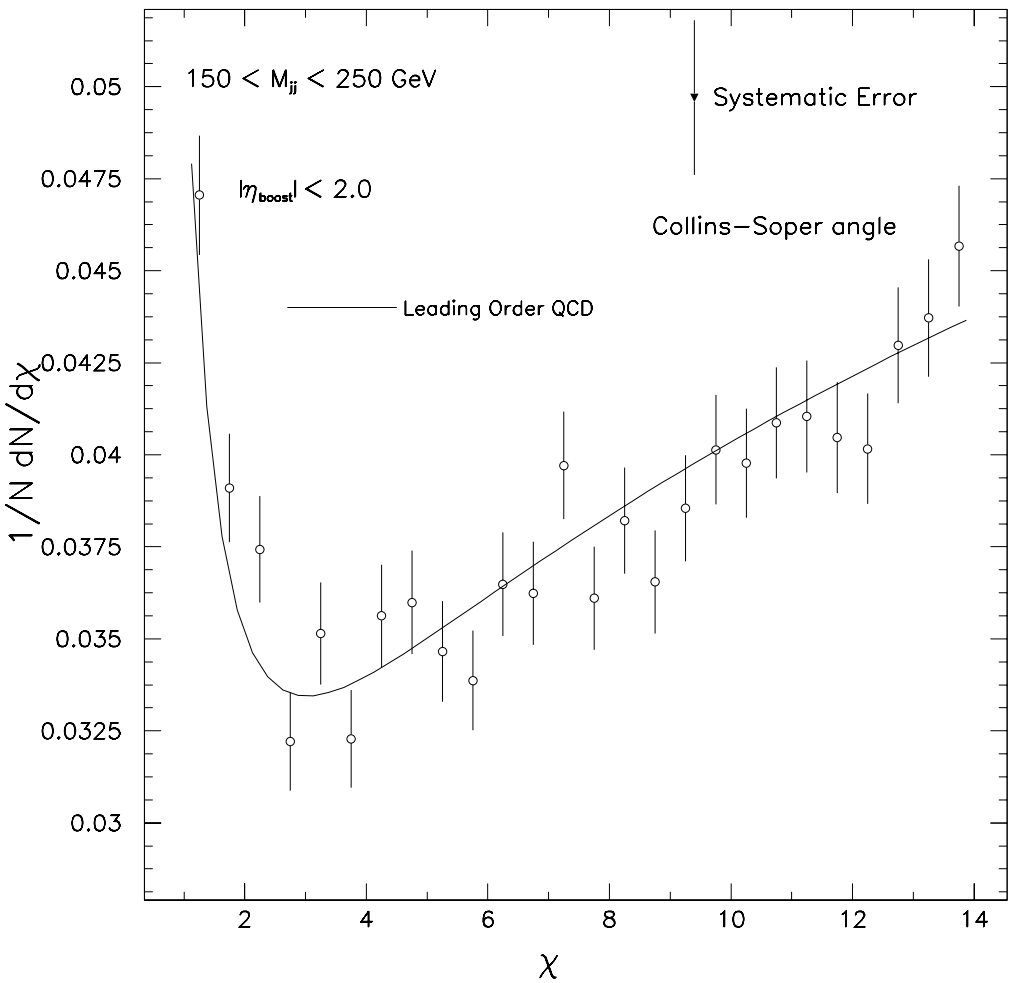

Figure 6.54: $dN/d\chi$ versus χ for $150 < M_{JJ} < 250$ distribution obtained using the Collins-Soper angle compared to leading order QCD.

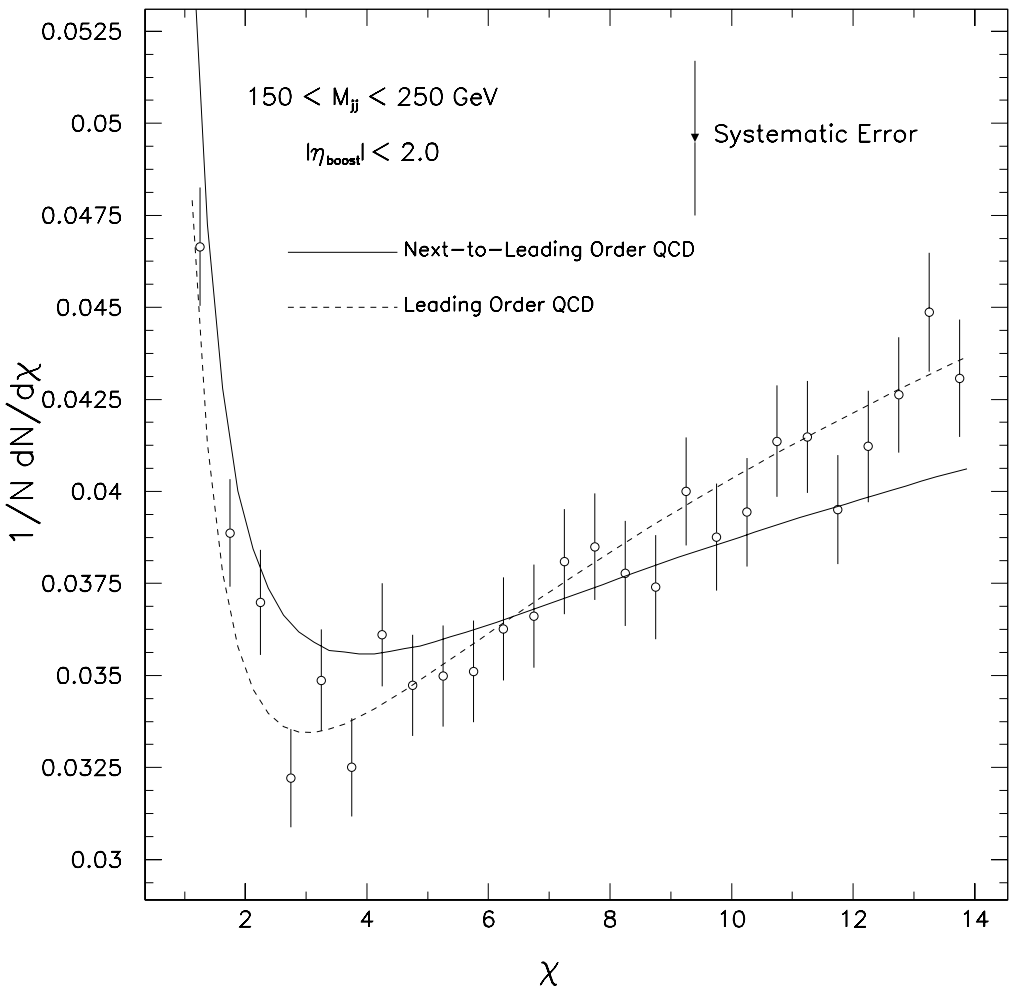

Figure 6.55: $dN/d\chi$ versus χ for $150 < M_{JJ} < 250$ distribution obtained using the simple definition $\eta^* = \frac{1}{2}(\eta_1 - \eta_2)$ compared to both leading order and next-to-leading order.

the $O(\alpha_s^3)$ curves.

Over this larger angular range the slope difference between the $O(\alpha_s^2)$ and $O(\alpha_s^3)$ curves becomes a larger overall effect. The difference between the two curves is about 15% at low χ compared to the combined statistical and systematic uncertainty of 12.5%. The data agrees quite well with the next-to-leading order prediction, but also with the leading order curve.

JET_MEDIUM: $350 < M_{JJ} < 450$ **GeV**

In Figure 6.57 the distribution is compared to both leading and next-to-leading order QCD predictions. The data is clearly in better agreement with the flatter $O(\alpha_s^3)$ curve. The $O(\alpha_s^2)$ curve is a somewhat poor fit with a significance level of only 11%.

JET_HIGH: $450 < M_{JJ} < 550$ **GeV**

In Figure 6.58 the distribution is compared to both leading and next-to-leading order QCD predictions. The data seems to favor a flatter distribution than the leading order and even slightly flatter than the NLO curve. The steep $O(\alpha_s^2)$ curve is here ruled out at the 1% significance level. The $O(\alpha_s^3)$ curve is a poor fit due to what seems to be large statistical fluctuations but still acceptable with only a 9% significance level.

JET_MAX: $M_{JJ} > 550$ **GeV**

Figure 6.59 shows the comparison of the distribution to both leading and next-to-leading order QCD predictions. The data cannot be used to reject either curve, although neither is a very good fit. This data will also be used in the search for composite quarks which will be discussed in the next section.

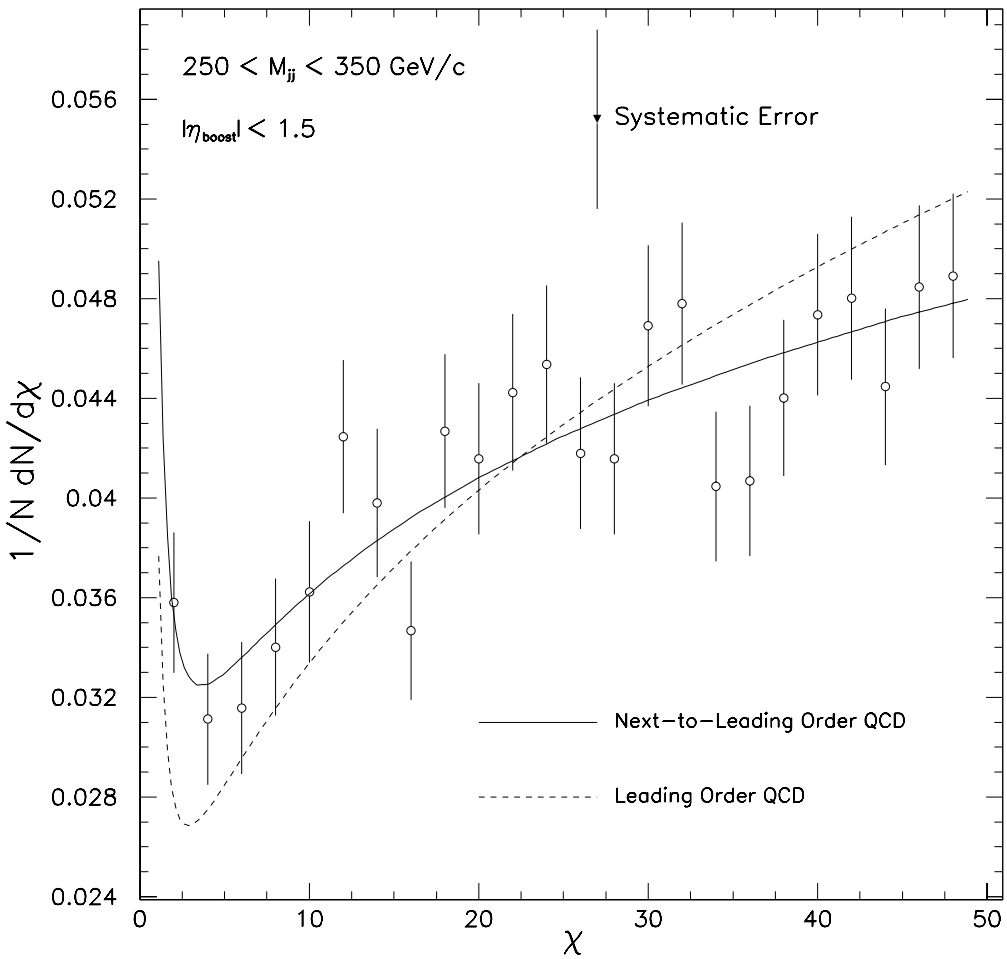

Figure 6.56: $dN/d\chi$ versus χ for $250 < M_{JJ} < 350$.

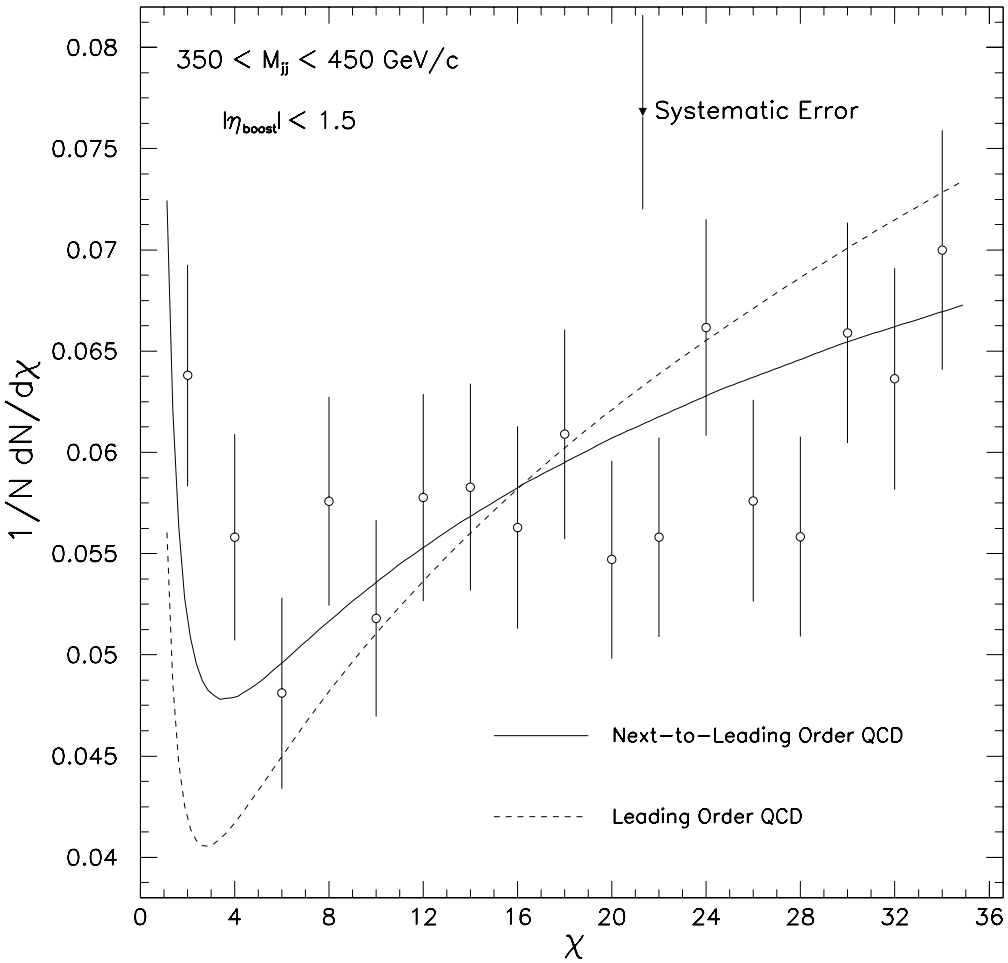

Figure 6.57: $dN/d\chi$ versus χ for $350 < M_{JJ} < 450$.

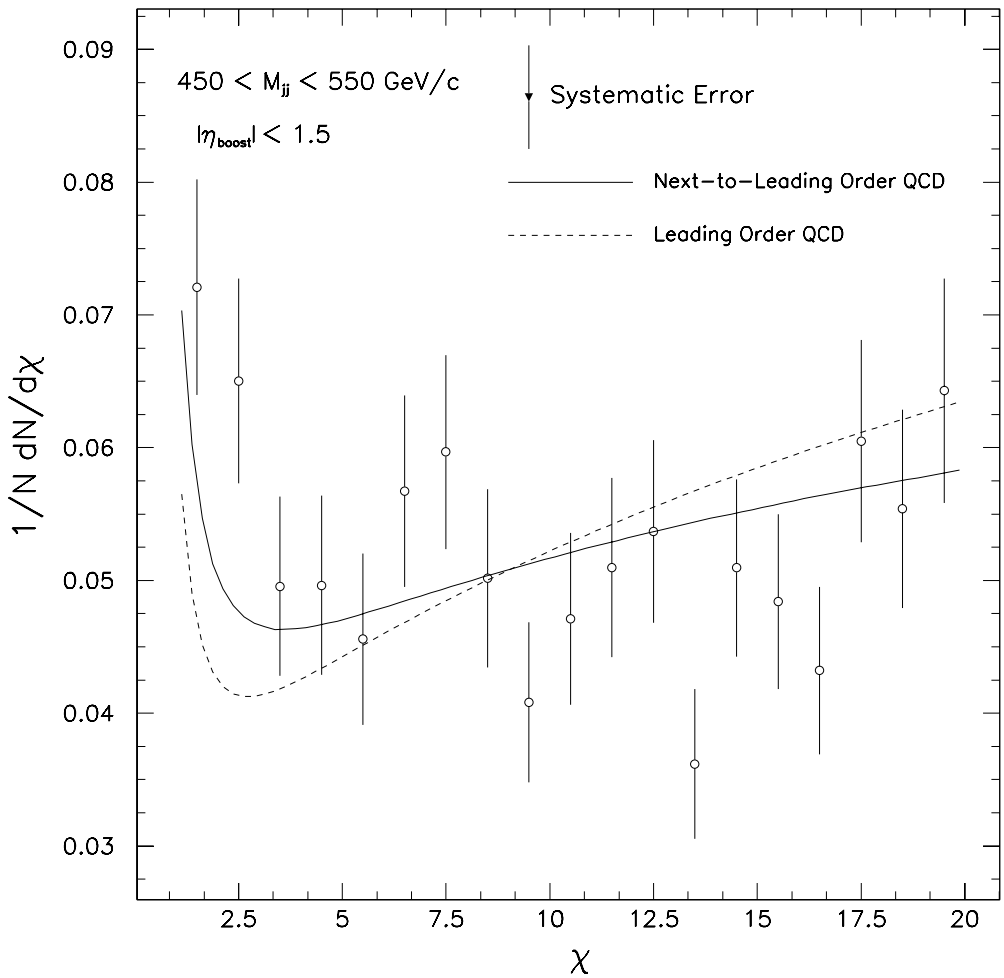

Figure 6.58: $dN/d\chi$ versus χ for $450 < M_{JJ} < 550$.

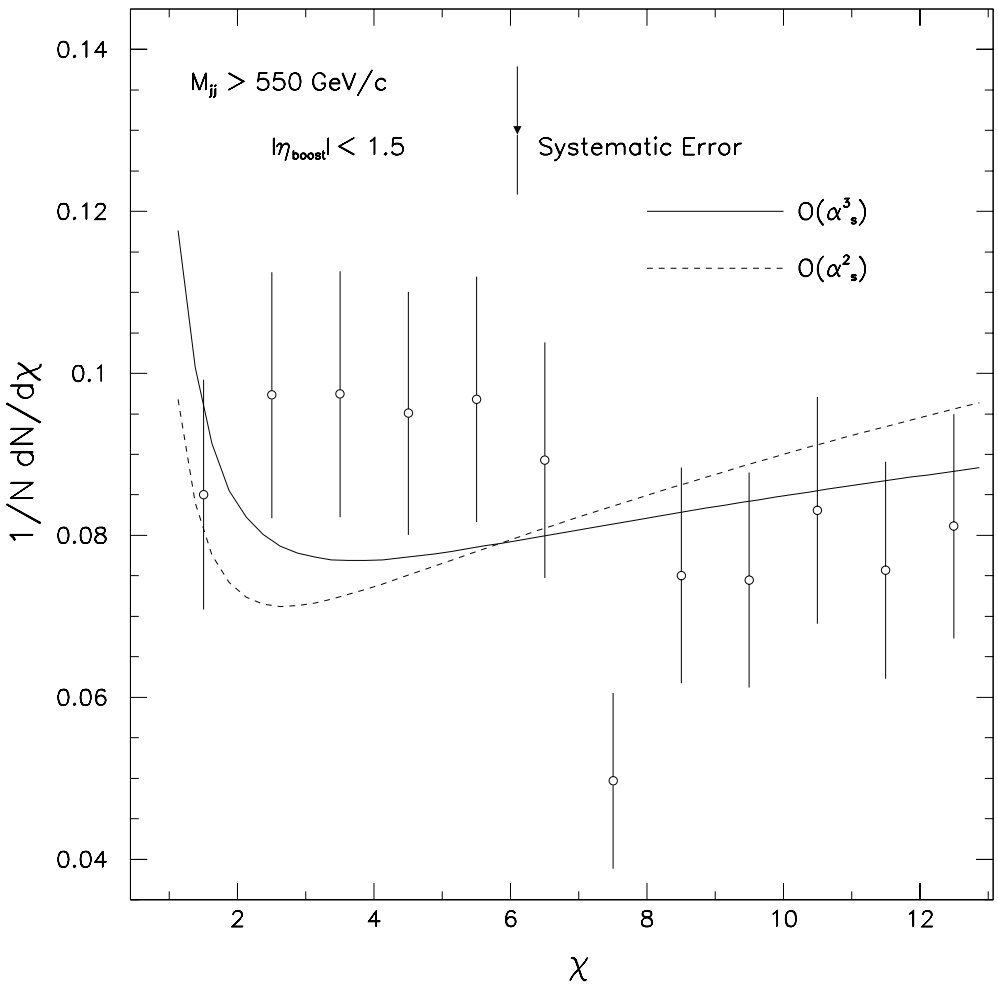

Figure 6.59: $dN/d\chi$ versus χ for $M_{JJ} > 550$ GeV.

Table 6.7: Results of fits of $O(\alpha_s^2)$ and $O(\alpha_s^3)$ QCD predictions to the data. χ^2 significance levels in % are shown.

Mass	Trigger	$O(\alpha_s^2)$	$O(\alpha_s^3)$
100 - 150	JET_MIN	98	7
150 - 250	JET_LOW	100	90
250 - 350	JET_LOW	80	100
350 - 450	JET_MEDIUM	11	94
450 - 550	JET_HIGH	.2	9
550 -	JET_MAX	9	31
450 -	JET_LOW	75	95

JET_LOW: $M_{JJ} > 450$ **GeV**

In Figure 6.60 the distribution is compared to both leading and next-to-leading order QCD predictions. The large mass threshold which provides the very large angular reach of the data also limits the statistics to somewhat low levels. This data is in good qualitative agreement with both curves, although the significance levels show a slight preference for the $O(\alpha_s^3)$ curve. It is worth noting that this measurement extends the range in χ by more than a factor of 7 over previous attempts[30, 38, 39].

Summary

Although all the mass ranges have nominal agreement with the NLO QCD predictions, a clear trend is seen in Table 6.7 toward better agreement with NLO (i.e., flatter distributions) for dijet masses greater than 250 GeV and better agreement with leading order QCD curves (steeper distributions) for masses lower than about 250 GeV.

It should be noted that the theoretical curves are not without their own intrinsic uncertainties. The momentum scale sensitivity is very large and this gives an uncertainty of 10% for the $O(\alpha_s^3)$ curves. This is equivalent to the difference between the data points and the NLO curve in Figure 6.53 ($100 < M_{JJ} < 150$ GeV.) Perhaps a different choice of the form of the momentum scale could give

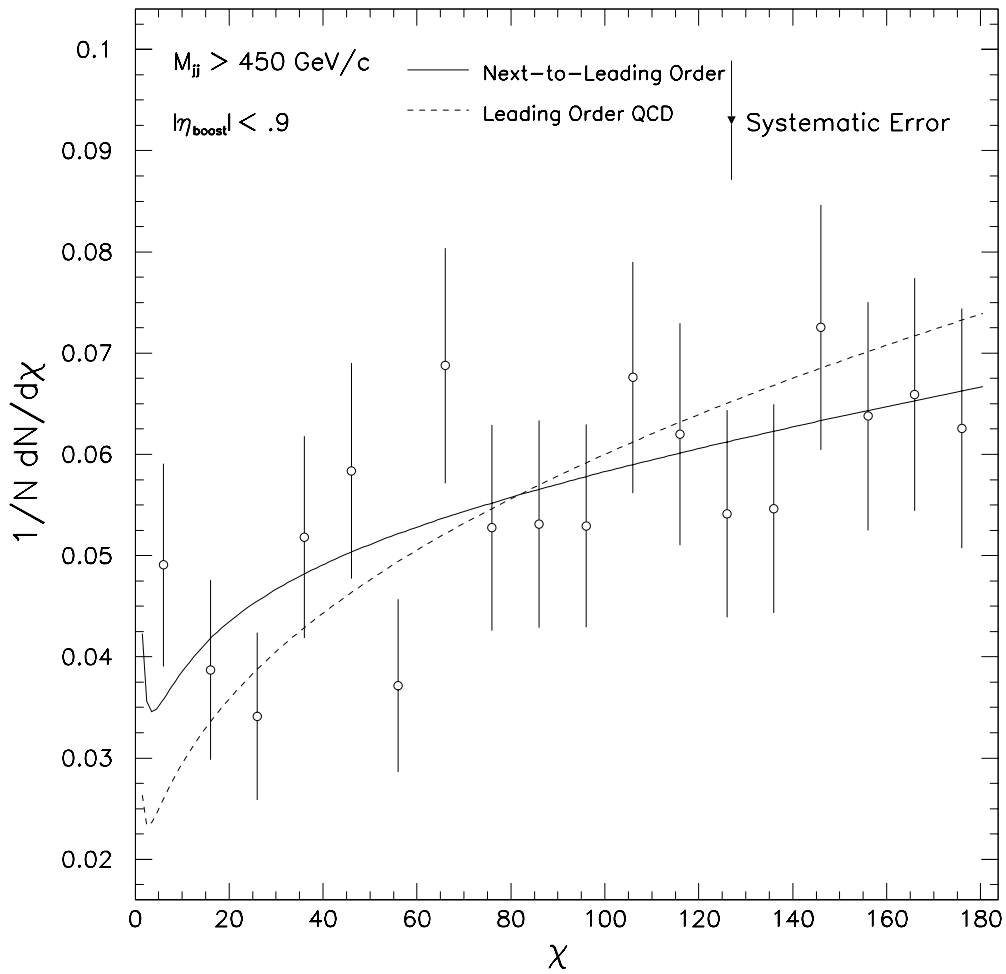

Figure 6.60: $dN/d\chi$ versus χ for $M_{JJ} > 450$ GeV.

Table 6.8: Results of fits of $O(\alpha_s^2)$ QCD with a quark-quark contact term. Shown is χ^2 significance levels as a function of Λ_C.

Λ_C	χ^2 probability in %
800 GeV	$< .1$
900 GeV	$< .1$
1000 GeV	$< .1$
1100 GeV	1.0
1200 GeV	9

better agreement with lower mass data.

6.4 Search for Quark Substructure

In this section we will use the high-mass data to put a limit on the scale of quark compositeness, Λ_C (see §2.6.4.) We will use the $M_{JJ} > 550$ GeV data compared to leading order curves generated with various values of Λ_C. The data was taken with the JET_MAX trigger, which was not prescaled (see §5.1.1.) By calculating significance levels we will determine the largest value of Λ_C that we can reject and take that as our upper limit on the scale of a composite interaction.

Various values of Λ_C have been used to generate curves and some are shown in Figure 6.61 along with pure leading order QCD ($\Lambda_C = \infty$.) Table 6.8 shows the results of fitting the curves as a function of Λ_C. Note that due to the shape of the contact-term-altered plots, the majority of our discrimination power is at low χ, where the difference in shape is largest.

As can be seen from the Table, we can rule out $\Lambda_C = 1.1$ TeV at the 5% significance level. The current highest published limit is 1.4 TeV from CDF single-jet inclusive cross sections [40] and the current highest limit from this method is 1.0 TeV from CDF [30]. Our limit is comparable although we have twice the integrated luminosity. This is due mainly to the poor range in χ of this trigger, which had a large single jet E_T threshold of 125 GeV. The range in χ can be increased by increasing the mass threshold (which also increases the sensitivity to

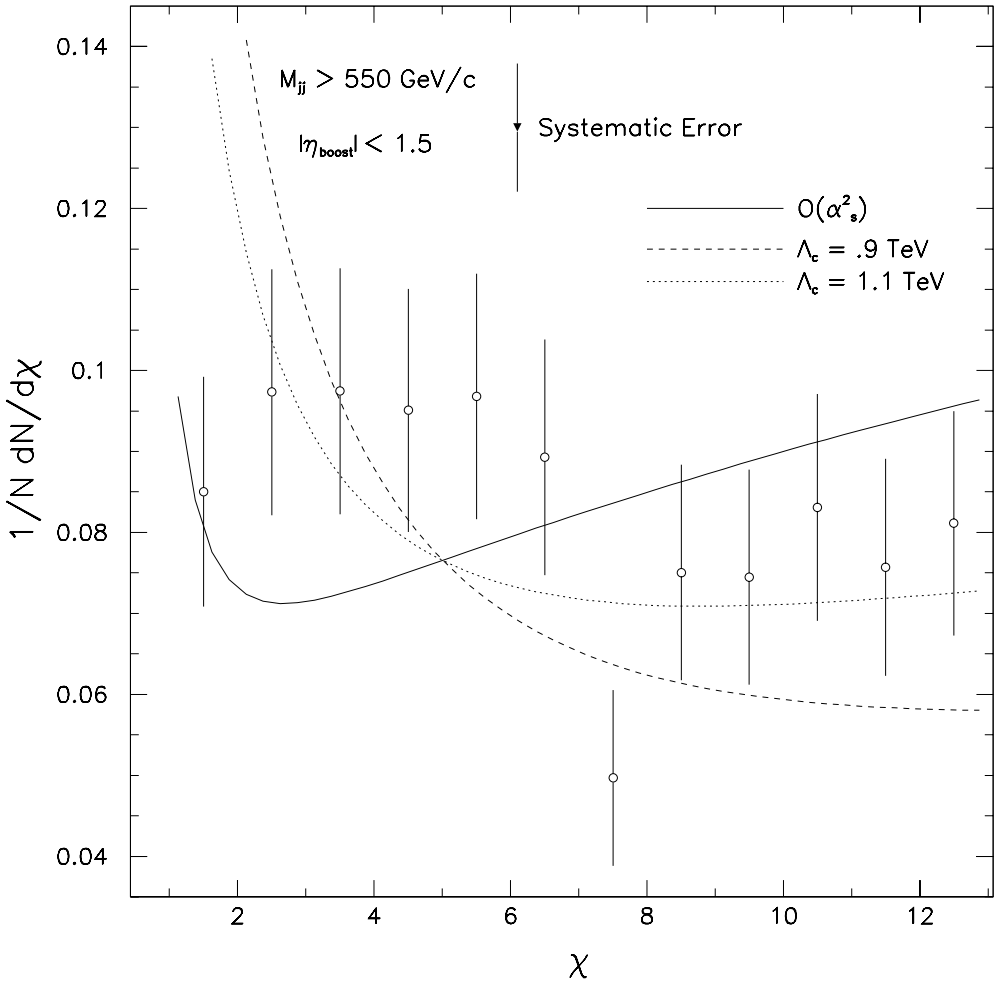

Figure 6.61: $dN/d\chi$ versus χ for $M_{JJ} > 550$ GeV compared to $O(\alpha_s^2)$ QCD without a contact term and with $\Lambda_C = 0.9$ Tev and $\Lambda_C = 1.1$ TeV.

higher Λ_C), but the subsequent loss of statistics negates any advantage.

The momentum scale used for the curves shown above was $Q^2 = P_T^2/4$ and the question arises what the results might be if the $O(\alpha_s^3)$- determined scale $Q = M_{JJ}/4\cosh(0.7\eta^*)$ were used instead in the same leading order calculation. Since it is flatter with no contact term added it should be steeper after the compositeness scale is introduced, perhaps allowing a higher Λ_C limit. Curves have been generated using the NLO momentum scale and compared to data, and although they are slightly steeper, the significance levels were lowered only slightly, from 9% to 7% for $\Lambda_C = 1.2$ TeV and from 1.0% to 0.6% for $\Lambda_C = 1.1$ TeV.

Another approach to compositeness would be to try to obtain a scale Λ_C by minimizing the χ^2 of the fit[41]. This shall be done using the knowledge that the compositeness signal increases the cross section at low χ which implies that the cross sections with and without the contact term converge at high χ. Using this information, we shall proceed by first normalizing the leading order QCD non-contact-term cross section to the three highest data points (the range from 10 to 13 in χ for the $M_{JJ} > 550$ GeV plot used here.) Then the fit is performed between the data and the leading order plus contact term curve where the contact term curve has been scaled using the same normalization correction. In other words, the relative scale between the curves with and without a contact term is maintained.

This procedure is also sensitive to the form of the momentum scale used and so has been done using both the leading order $Q = P_T/2$ and the next-to-leading-order-derived $Q = M_{JJ}/4\cosh(0.7\eta^*)$. The results including the best fit values of Λ_C are shown in Figure 6.62. The significance levels are 40% using the scale $Q = P_T/2$ and $\Lambda_C = 1.4$ TeV and 50These values of Λ_C are those multiples of 100 GeV that provided the best fit.

As can be seen from Figure 6.62, although better than leading order alone, the addition of a contact term does not make a curve that fits the data particularly well. It should be emphasized that the use of this procedure implies absolutely no claim for a compositeness signal in the data. We can only state a lower limit

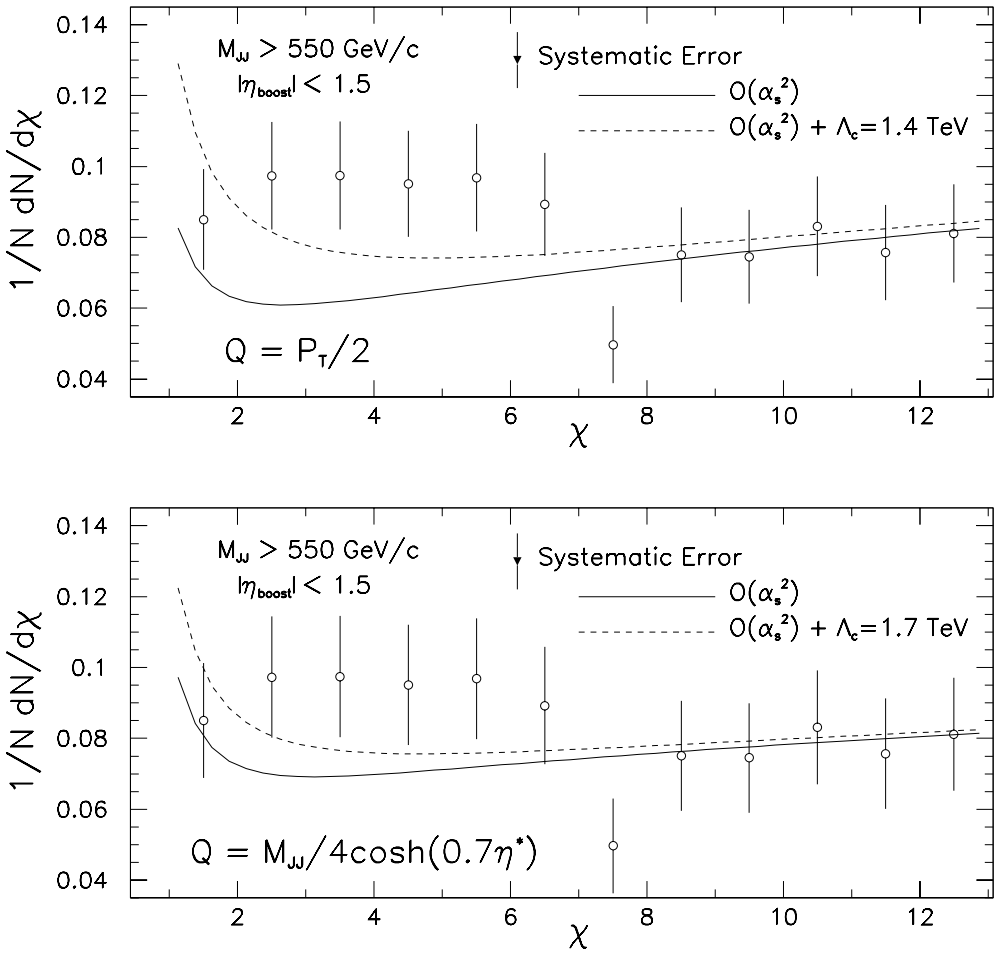

Figure 6.62: $dN/d\chi$ versus χ for $M_{JJ} > 550$ GeV. (Top): Leading order QCD alone and the best-fit curve LO QCD plus a contact term using the momentum scale $Q = P_T/2$. (Bottom): Same but using NLO-derived scale $Q = M_{JJ}/4\cosh(0.7\eta^*)$ and leading order QCD.

on Λ_C of 1.1 TeV as derived above. This exercise is illustrative of the type of procedure that might be employed should a more definite compositeness signature appear in future data. That is, using the high χ data for normalization and seeing if sufficient excess events are observed at low χ to make a claim for a statistically significant observed signal.

6.5 Conclusion

The DØ detector has made possible new measurements of the dijet angular distribution that, for the first time, are of sufficient precision to enable a possible distinction between leading order QCD and the new $O(\alpha_s^3)$ QCD predictions. The data shows reasonable agreement with $O(\alpha_s^3)$ predictions over the entire mass range from 100 to 550 GeV. With the leading order momentum scale choice $Q^2 = P_T^2/4$, the leading order curves give very good agreement for low masses ($M_{JJ} < 350$ GeV, but give worse fits for masses greater than this. In fact, for the mass range 450 - 550 Gev, the leading order fit is inconsistent with the data at the 1% level. However, when theoretical uncertainties are included, which can give uncertainties in the slope of the distribution of up to 40% for leading order and 10% for $O(\alpha_s^3)$ theory curves, no substantial distinction can be made between leading order and $O(\alpha_s^3)$ QCD theory on the basis of this data.

With large statistics at low masses and low systematic uncertainties, measurements of QCD phenomena have moved from simple "qualitative agreement" to more precise tests of the theory. The experimental uncertainties are at approximately the same or even slightly lower than the theoretical uncertainties for some mass ranges. The large uniform range of calorimetry has extended the range of measurable angles much farther than previously possible. Additionally, a limit on quark compositeness of $\Lambda_C = 1.1$ TeV has been obtained.

REFERENCES

[1] C. H. Llewellyn Smith, *Neutrino Interactions at Accelerators*, Phys. Rep. 3, 261, 1972.

[2] D.Duke, R.Roberts, Phys. Rep. 120, 275, 1985.

[3] G.Altarelli, Phys. Rep. 81, 1, 1982.

[4] S.Ellis, Z.Kunszt, D.Soper, Phys. Rev. Lett. 64, 2121, 1990.

[5] J. C. Collins, D. E. Soper, *Angular Distribution of Dileptons in High-Energy Hadron Collisions*, Phys. Rev. D16, 2219, 1977.

[6] B.L. Combridge, C.J. Maxwell, *Untangling Large-p_T Hadronic Reactions*, Nucl. Phys. B239,429, 1984.

[7] A.Martin, R.Roberts, W.Stirling, Phys. Rev. D43,3648, 1991.

[8] J. Morfin, W.K.Tung, Z. Phys. C52, 13, 1991.

[9] J. Botts, J.G. Morfin, J.F. Owens, J. Qiu, W.K. Tung, H. Weerts, *CTEQ Parton Distributions and Flavor Dependence of the Sea Quarks*, MSUHEP-92-27, Fermilab-Pub-92/371, FSU-HEP-92-1225, ISU-NP-92-17.

[10] R.Ellis, J.Sexton, Nucl. Phys. B269, 445, 1986.

[11] S.Ellis, Z.Kunszt, D.Soper, *Two-jet Production in Hadron Colliders at Order α_s^3 in QCD*, Phys. Rev. Lett. 69, 1496, 1992.

[12] E.Eichten et al., Rev. Mod. Phys. 56, 579, 1984, erratum 58 ,1065.

[13] DØ Collaboration, *An Experiment at DØ to Study Antiproton-Proton Collisons at 2 TeV: A Design Report*, Print-84-0306 (Fermilab) 1983.

[14] S.Abachi et al, (The DZero Collaboration), *The D-Zero Detector*, Report No. Fermilab-PUB-93/179, (submitted to Nucl. Inst. and Meth. A), 1993.

[15] A. Clark et al, *The Central Tracking Detectors for DØ*, CONF-8806235-8-mc (microfiche), 1988.

[16] DØ Collaboration, *Design, Construction, and Performance of the Electromagnetic Module of the D-Zero End Calorimeter*, Submitted to Nucl. Instrum. Meth. A., 1992.

[17] F. Nang, R. Partridge, *Level 0 Detector Layout*, DØ internal note #998, DØ Experiment at Fermilab, Batavia, IL, Aug. 1990.

[18] R. Astur, H. Weerts, *Level 1 Jet Trigger and Level 2 Jet Tool: Rates and Efficiencies*, DØ internal note #1044, DØ Experiment at Fermilab, Batavia, IL, Nov. 1990.

[19] N. Hadley, *Cone Algorithm for Jet Finding*, DØ internal note #904, DØ Experiment at Fermilab, Batavia, IL, Nov. 1989.

[20] G. Forden, (private communication), June 1993.

[21] R. Brun et al, GEANT3 Users Guide, CERN-DD/EE/84-1, May 1986.

[22] DØ Collaboration, *Beam Test of the DØ Uranium Liquid Argon End Calorimeters*, Nucl. Instrum. Meth. A324:53-76, 1993.

[23] F. Paige, S. Protopopescu, *ISAJET*, BNL-31987.

[24] B. Klima, C. Stewart, *PJET-Parton Jets in the Monte Carlo*, DØ internal note #905, DØ Experiment at Fermilab, Batavia, IL, Dec. 1989.

[25] R. Astur, *A Study of the Ability of the DØ Detector to Measure the Single Jet Inclusive Cross Section*, Ph.D. thesis, Michigan State University, 1992.

[26] J. Borders, R. Hirosky, P. Bhat, (private communications), Oct. 1992.

[27] H. Bengtsson, T. Sjostrand, *The Lund Monte Carlo for Hadronic Processes*, CERN/TH, CH-1211, May 1990.

[28] A. Milder, R. Astur, *Jet Energy Scale using Test Beam Data*, DØ internal note #1595, DØ Experiment at Fermilab, Batavia, IL, Dec. 1992.

[29] R. Astur, A. Milder, J. Borders, D. Cullen-Vidal, *Determining the Jet Energy Scale using Test Beam Data*, DØ internal note #1689, DØ Experiment at Fermilab, Batavia, IL, Mar. 1993.

[30] F. Abe et al, (The CDF Collaboration), *The Dijet Angular Distribution in $p\bar{p}$ Collisions at $\sqrt{s}$ = 1.8 TeV*, FERMILAB-Pub-92/182-E, Submitted to Phys. Rev. Lett., 1992.

[31] G.Marchesini, B.R.Webber, Nucl. Phys. B310 (1988) 461; ibid. B330 (1990) 261; I.G. Knowles, Nuc. Phys. B310 (1988) 571.

[32] Particle Data Group, *Review of Particle Properties*, Phys. Rev D45, Part 2, June 1992.

[33] R. Astur, J. Borders, (private communication), Feb. 1993.

[34] B.May, (private communication), June 1993.

[35] J.Jaques, (private communication), June 1993.

[36] G. Forden, *A Plan for In-Situ Calibration of the DØ Calorimeters*, DØ internal note #1442, DØ Experiment at Fermilab, Batavia, IL, June 1992.

[37] Partonic Event Generator PAPAGENO written by Ian Hinchliffe, Theoretical Physics Group, Lawrence Berkeley Laboratory, Version 3.60, 1993.

[38] G. Arnison et al, (The UA1 Collaboration), *Angular Distributions and Structure Functions from Two-Jet Events at the CERN SPS $p\bar{p}$ Collider*, Phys. Lett. 158B, 494, 1985.

[39] P. Bagnaia et al, (The UA2 Collaboration), *Measurement of Jet Production Properties at the CERN $\bar{p}p$ Collider*, Phys. Lett. 144B, 283, 1984.

[40] F. Abe et al, (The CDF Collaboration), *Inclusive Jet Cross Section in $\bar{p}p$ Collisions at $\sqrt{s}$ = 1.8 TeV*, Phys. Rev. Lett. 68: 1104, 1992.

[41] M. Shupe, (private communication), Aug. 1993.